Cosmology with next generation radio telescopes

PhD Thesis

Author:
Amadeus Witzemann (Wild)

Supervisor:
Prof. Mario Santos
Co-Supervisors:
Prof. Amanda Weltman
Prof. Chris Clarkson

UNIVERSITY *of the* WESTERN CAPE

A thesis submitted in partial fulfilment of the requirements for the degree of Doctor Philosophiae in the Department of Physics and Astronomy, University of the Western Cape.

Centre for Radio Cosmology
Department of Physics and Astronomy

University of the Western Cape

July 2, 2019

Declaration of Authorship

I, Amadeus Witzemann (Wild), declare that this thesis titled, "*Cosmology with next generation radio telescopes*" is my own work, that it has not been submitted for any degree or examination in any other university, and that all the sources I have used or quoted have been indicated and acknowledged by complete references.

Signed: 

Date: July 3rd, 2019

Keywords: cosmology, emission line surveys, large scale structure, intensity mapping, HI 21cm line, forecasting, curvature, multi-tracer technique, gravitational lensing, cosmic magnification

UNIVERSITY OF THE WESTERN CAPE

Abstract

Faculty of Natural Science
Department of Physics and Astronomy

PhD

Cosmology with next generation radio telescopes

by Amadeus Witzemann (Wild)

The next generation of radio telescopes will revolutionize cosmology by providing large three-dimensional surveys of the universe. This work presents forecasts using the technique *21cm intensity mapping* (IM) combined with results from the cosmic microwave background, or mock data of galaxy surveys. First, we discuss prospects of constraining curvature independently of the dark energy (DE) model, finding that the radio instrument HIRAX will reach percent-level accuracy even when an arbitrary DE equation of state is assumed. This is followed by a study of the potential of the multi-tracer technique to surpass the cosmic variance limit, a crucial method to probe primordial non-Gaussianity and large scale general relativistic effects. Using full sky simulations for the Square Kilometre Array phase 1 (SKA 1 MID) and the Large Synoptic Survey Telescope (LSST), including foregrounds, we demonstrate that the cosmic variance contaminated scenario can be beaten even in the noise free case. Finally, we derive the signal to noise ratio for the cosmic magnification signal from foreground HI intensity maps combined with background galaxy count maps. Instruments like SKA1 MID and HIRAX are highly complementary and well suited for this measurement. Thanks to the powerful design of the planned radio instruments, all results confirm their potential and promise an exciting future for cosmology.

July 2, 2019

Acknowledgements

I would like to thank my collaborators Alkistis Pourtsidou and Marta Spinelli who inspired and assisted my work, and fellow students who always helped me when I asked for advice. I express special gratitude to David Alonso and Phil Bull, who patiently guided and taught me, and who thus invaluably contributed to the progress and quality of our projects and my entire thesis. My supervisors Mario Santos, Amanda Weltman and Chris Clarkson helped me find my way on this long and often difficult journey. I could always rely on my wife Anna and her unfailing aid. I acknowledge the support of the Centre for High Performance Computing, South Africa, under the project ASTR0945.

Contents

Declaration of Authorship **ii**

Abstract **iv**

Acknowledgements **v**

1 Introduction **1**

2 The standard model **6**

2.1 Metric and distances 6

2.1.1 The Friedmann equations 7

2.1.2 Distance measures 10

2.2 Inhomogeneities and Anisotropies 12

2.2.1 The 3-D power spectrum 12

2.2.2 Baryon Acoustic Oscillations 13

2.2.3 The angular power spectrum 14

2.2.4 The galaxy bias 18

3 Forecasting methods **20**

3.1 Bayes' theorem 20

3.2 Fisher matrix formalism 21

3.3 Markov Chain Monte Carlo: a tool for forecasting and parameter estimation 22

3.3.1 Sampling distributions 23

3.3.2 Convergence 24

4 Radio cosmology **27**

4.1 Planned radio and optical instruments for cosmology 27

4.2 Radio continuum 30

4.3 21cm galaxy clustering . . . 32
4.4 21cm intensity mapping . . . 33
4.4.1 Cosmological probes . . . 34
4.4.2 Foreground contamination . . . 37
4.4.3 The 21cm signal model . . . 41
4.4.4 Forecasts for MeerKLASS . . . 42

5 Model-independent curvature determination 46
5.1 Introduction . . . 47
5.2 Forecasting for HIRAX . . . 49
5.2.1 Noise power spectrum . . . 49
5.2.2 Drift scanning . . . 51
5.2.3 Survey optimization . . . 51
5.3 Curvature measurements in the presence of dark energy . . . 52
5.3.1 Avoiding the dark energy era . . . 52
5.3.2 Non-parametric dark energy marginalization . . . 54
5.3.3 Series expansion of dark energy . . . 55
5.4 Forecasts for IM experiments . . . 56
5.4.1 Convergence of the curvature constraints . . . 59
5.4.2 Results . . . 59
5.5 Conclusions . . . 61

6 Simulated multi-tracer analyses 64
6.1 Introduction . . . 65
6.2 Multi-tracer estimators . . . 69
6.2.1 Signal modeling . . . 69
6.2.2 The Surveys . . . 71
6.2.3 The Estimators . . . 73
6.3 Simulated Forecasts . . . 75
6.3.1 The Simulations . . . 75
6.3.2 Foreground Removal . . . 77
6.4 Results . . . 79
6.4.1 Theoretical expectation . . . 79
6.4.2 Foreground-free results . . . 82

6.4.3 Foreground removal 85
6.4.4 Results in the presence of foregrounds 87
Sensitivity and bias 87
The effects of foregrounds 92
6.5 Discussion 98

7 Magnification measurements with HI intensity mapping 103
7.1 Introduction 104
7.2 Cosmic magnification statistics 106
7.2.1 Galaxies as the foreground sample 107
7.2.2 HI intensity maps as the foreground sample 108
7.3 Error calculations 113
7.3.1 HI intensity maps 113
7.3.2 Photometric galaxy counts 116
7.4 Results and Discussion 121
7.5 Conclusions 121

8 Conclusions 123

1 Introduction

During the last few decades, cosmology has made significant progress. A large number of precise observations greatly decreased uncertainties in the science, it is thus said that we have entered the era of 'precision' cosmology (Planck Collaboration XIII, 2016; Alam et al., 2017). The most successful model in modern cosmology, Lambda Cold Dark Matter (ΛCDM), or Concordance Cosmology, is based on observations of the spectrum and temperature fluctuations of the cosmic microwave background (CMB) (Planck Collaboration XIII, 2016), galaxy clustering (Sánchez et al., 2017; Alam et al., 2017), the abundances of light elements and their isotopes (e.g. Walker et al., 1991; Smith et al., 1993; Copi et al., 1995; Burles & Tytler, 1998), and last but not least on measurements of redshifts and distances to type Ia supernovae (Riess et al., 1998; Perlmutter et al., 1999). While a few problems and tensions remain (Dodelson, 2003), it describes with incredible precision both low redshift observations at $z < 1$, e.g. galaxy surveys, and the extremely high redshift measurements of the CMB with $z \approx 1100$.

CMB photons last scattered during the epoch of recombination, 300000 years after the big bang, when the Universe cooled enough for electrons and protons to combine. They have traveled freely through space since. This black-body radiation is an extremely powerful probe of early universe physics and significantly contributed to the success of big bang theory (Dodelson, 2003). Since its first detection in the mid-1960s by Penzias and Wilson, high-precision full-sky maps of temperature fluctuations in the CMB have been obtained by the spacecrafts Wilkinson Microwave Anisotropy Probe (WMAP) (Bennett et al., 2003) and Planck[1], giving great insight into early Universe large scale structure.

Amongst the probes of the late-time Universe, Type Ia supernovae and

[1] www.esa.int/Our_Activities/Space_Science/Planck

galaxy clustering statistics stand out. They provide independent means of constraining redshift-distance relations as well as maps of cosmic structure. The widely accepted notion of the accelerating expansion first came up with Hubble rate constraints from supernova observations, and is strengthened by results from galaxy clustering, most notably the Dark Energy Survey (DES[2]) and the Sloan Digital Sky Survey (SDSS[3]). These large-area surveys in optical and infrared frequencies directly probe large scale structure by detecting galaxies and measuring their redshifts, thus greatly improving our understanding of the accelerated expansion of the Universe. The cosmological constant Λ, of uncertain origin, contributing to the Universes energy density and thus accelerating its expansion, is one of the basic parameters in ΛCDM. Dark energy, a popular extension to standard cosmology generalizing the cosmological constant, is the concept of an energy form with potentially varying, but mostly negative pressure. It remains one of the greatest challenges in cosmology to distinguish between a cosmological constant, dark energy, or an alternative explanation, and to fully understand the physical origin of cosmic acceleration. Chapter 5 deals with the problem of the weakly constrained dark energy equation of state and the degeneracies that thus arise with other cosmological parameters. It presents a way to analyze observations in a model-independent way.

When Zwicky (1937) found that galaxy cluster mass estimates based on their luminosities yield results greatly different from dynamical mass measurements, the first evidence for a non-radiating matter, so called Dark Matter (DM), was provided. Later observations of galaxy masses (e.g. Rubin & Ford, 1970), the growth of large scale structure (e.g. Croft et al., 2002; Kunz et al., 2016) and gravitational lensing mass estimates (e.g. Tyson et al., 1990) also called for DM. In standard cosmology, roughly 85% of all matter is thought to be dark (Planck Collaboration et al., 2016), but its nature and origin are still unknown and alternative explanations that do not require the DM concept still are not ruled out. See Arun et al. (2017) for a review of theories and observations of dark matter.

[2]www.darkenergysurvey.org
[3]www.sdss.org

With most available cosmological data located either at extremely large redshifts, like the CMB, or at comparably close distance to us, there remains a great lack of data at intermediate redshifts. Therefore current data is unable even to constrain simple extensions to standard cosmology. Especially the range of $1 \leq z \leq 6$, where much of the important evolution in the universe takes place, has received a lot of attention in recent years. Mapping the matter distribution over a large fraction of this redshift range would allow us to unambiguously constrain more general models of dark energy, as well as cosmic curvature, among many other things (Morales & Wyithe, 2010). Redshifts beyond $z \sim 6$, including the Epoch of Reionization and the Dark Ages, are also extremely interesting, but even harder to probe than lower redshifts (Lewis & Challinor, 2007; Furlanetto et al., 2006; Fan et al., 2006). In essence, measuring a much greater range of redshifts will not only allow us to probe the redshift dependence of important cosmological quantities, like the Hubble rate or the equation of state of dark energy, but also enable us to test and potentially extend ΛCDM cosmology and fundamental theories of gravity at scales and energies never explored before (Pritchard & Loeb, 2012; Hall et al., 2013). Planned optical experiments, like the spacecraft Euclid[4] (Laureijs et al., 2011) and the Large Synoptic Survey Telescope[5] (LSST Science Collaboration et al., 2009) will greatly increase precision, survey area and redshift depth of galaxy clustering data. In a very innovative approach, the next generation of radio telescopes, like the Square Kilometer Array (SKA)[6] or HIRAX (Newburgh et al., 2016a), promises to map an even larger volume of the Universe with extremely precise redshift information. The still young field of radio cosmology will provide new and independent measurements of the distribution of matter in the universe, completing the picture drawn by supernova, optical galaxy and microwave observations, and removing degeneracies still present in today's data sets. Specifically, measuring the redshifted emission from the 21cm line emission of neutral hydrogen is greatly promising (Pritchard & Loeb, 2012; McQuinn et al., 2006; Bull et al., 2015b; Furlanetto et al., 2006). It will allow us to

[4]www.euclid-ec.org
[5]www.lsst.org
[6]www.skatelescope.org

probe the redshift dependent distribution of neutral hydrogen, which is thought to trace the underlying dark matter field, over wide and mostly unexplored regions deep into space.

While the nature of CMB data is in principle two-dimensional, and all current galaxy clustering as well as supernova data is at very low redshifts, the data obtained by this new generation of telescopes will be of a fully three-dimensional nature. This work points out some of the weaknesses of current data sets, and shows new ways to overcome modeling and analysis problems using the power of three-dimensional data.

Specifically, chapter 5 demonstrates how curvature constraints heavily rely on the assumptions on dark energy. Although the current modeling of dark energy as the cosmological constant Λ explains available data very well, this might be due to the small volume explored by that data. The lack of good physical understanding of dark energy justifies the consideration of more general equations of state of dark energy (DE EOS) than needed to describe the CMB and low redshift observations alone. Assuming that the DE EOS is not necessarily fixed, but could be varying with time, greatly weakens curvature constraints. Data gathered by an instrument like HIRAX will put tight constraints on Ω_k, even in a model with an entirely free functional form of the DE EOS. In order to demonstrate this, we simulate data as obtained from HIRAX and develop a model-independent technique to derive curvature constraints.

By combining data from planned radio experiments with planned galaxy surveys, e.g. the Large Synoptic Survey Telescope (LSST)[7] or Euclid[8], we expect to yield tighter constraints than each type of survey could obtain individually. An example of such a synergy between different experiments is the multi-tracer technique, which requires measurements of two or more biased tracers of the dark matter background. The technique benefits from tracers with very distinct biases. It is argued that certain observables can thus be measured up to a precision surpassing the cosmic variance limit. This fundamental limit is commonly thought to be insurmountable. It arises due to the finite size of the observable universe, or of a given survey, which limits

[7] www.lsst.org
[8] www.euclid-ec.org

the statistical sample size of large structures. By using a combination of different surveys, however, one hopes to measure some quantities up to much higher precision than cosmic variance would allow. In section 6, we thoroughly investigate the potential of the multi-tracer technique in the case of combining maps from LSST and SKA. We simulate data sets for each instrument and realistically contaminate the intensity maps with foreground radiation. We find that, after the cleaning of the foreground contamination, the cosmic variance limit can still be breached albeit at a much smaller margin than when foreground effects are ignored. We conclude by offering an explanation for this effect and discuss potential ways to solve the problem using other survey combinations.

In chapter 7, we look at an entirely different way of combining optical and radio maps, forecasting the signal to noise ratio for a detection of the cosmic magnification signal. We use foreground HI maps acting on and magnifying the clustering of background galaxies. This weak effect is predicted by the theory of General Relativity and is notoriously hard to detect. Using the future instruments SKA, HIRAX and LSST, though, the prospects are bright and a detection seems likely.

2 The standard model of cosmology

This chapter introduces concepts of standard cosmology and basic extensions, which form the physical basis to this work. Largely following the excellent book by Dodelson (2003), the Friedmann-Lemaître-Robertson-Walker space time metric, the Friedmann equations and the most common distance notions in cosmology are introduced in section 2.1. The chapter is concluded with a very brief discussion of the large scale structure in the universe in section 2.2, putting special emphasis on the angular power spectrum, including a derivation in a general example.

2.1 Metric and distances

We start with the distance, also called proper time or line element, which is generally given by the space-time metric $g_{\mu\nu}$ as

$$ds^2 = g_{\mu\nu} dx^\mu dx^\nu, \tag{2.1}$$

where Einstein's summation rule is applied and the infinitesimal coordinate separations dx^μ have indices μ and ν running from $0 \to 3$. Making use of the standard cosmological assumption of a homogeneously expanding, isotropic universe, the metric is heavily constrained. It can only take the form

$$ds^2 = -dt^2 + a^2(t)\gamma_{ij} dx^i dx^j, \tag{2.2}$$

with scale factor a, cosmic time t and i, j from $1 \to 3$. The metric of constant time hypersurfaces γ_{ij} is also constrained and can be written as (Peter & Uzan, 2009)

$$dx^2 \equiv \gamma_{ij} dx^i dx^j = \frac{dr^2}{1 - kr^2} + r^2(d\theta^2 + \sin^2(\theta) d\phi^2). \tag{2.3}$$

Here dx^2 denotes the 3D line element with radius r, the curvature of the metric is k and the infinitesimal solid angle is $d\theta^2 + \sin^2(\theta) d\phi^2$. In standard cosmology, space is assumed to be flat, i.e. $k \equiv 0$ (Dodelson, 2003). This implies $\gamma_{ij} \equiv \mathbb{1}$ in Euclidean coordinates, which gives the flat Friedmann-Lemaître-Robertson-Walker (FLRW) metric

$$g_{\mu\nu} = \begin{pmatrix} -1 & 0 & 0 & 0 \\ 0 & a^2(t) & 0 & 0 \\ 0 & 0 & a^2(t) & 0 \\ 0 & 0 & 0 & a^2(t) \end{pmatrix}. \tag{2.4}$$

The redshift is usually defined as $1 + z = \lambda_{\text{now}}/\lambda_{\text{emit}}$, with λ_{emit} the wavelength of any radiation at its emission and λ_{now} at the time of its detection. Using the common convention that the scale factor today $a_0 \equiv 1$, their relation can easily be shown to be

$$1 + z = \frac{1}{a}. \tag{2.5}$$

Besides this cosmological contribution, the redshift also contains other contributions from peculiar velocities (Doppler effect) and gravitational redshift, both ignored for now.

2.1.1 The Friedmann equations

The Einstein equations describe the relation between energy, or more specifically, the energy-momentum-stress tensor $T_{\mu\nu}$ and the metric. In the case of cosmology, the general equations with 10 components,

$$G_{\mu\nu} = 8\pi T_{\mu\nu}, \tag{2.6}$$

can greatly be simplified to yield the Friedmann equations (Dodelson, 2003). The relation between metric and Einstein tensor

$$G_{\mu\nu} = R_{\mu\nu} - \frac{1}{2} g_{\mu\nu} \mathcal{R} \tag{2.7}$$

can be expressed using the Christoffel symbols[1]

$$\Gamma^{\mu}{}_{\alpha\beta} = \frac{g^{\mu\nu}}{2} \left(g_{\alpha\nu,\beta} + g_{\beta\nu,\alpha} - g_{\alpha\beta,\nu} \right) \tag{2.8}$$

and the Ricci scalar $\mathcal{R} = g^{\mu\nu} R_{\mu\nu}$ as well as Ricci tensor

$$R_{\mu\nu} = \Gamma^{\alpha}{}_{\mu\nu,\alpha} - \Gamma^{\alpha}{}_{\mu\alpha,\nu} + \Gamma^{\alpha}{}_{\beta\alpha} \Gamma^{\beta}{}_{\mu\nu} - \Gamma^{\alpha}{}_{\beta\nu} \Gamma^{\beta}{}_{\mu\alpha}. \tag{2.9}$$

To the interested reader, Misner et al. (1973) is a voluminous but pedagogic and thorough resource on gravitation and differential geometry in general as well as in a cosmological context.

Using the Hubble rate $H = \dot{a}/a$ and Newton's gravitational constant G, the time-time component ($\mu = \nu = 0$) of the Einstein equation for the non-flat FLRW metric can be simplified to

$$H^2 = \frac{8\pi G}{3} \rho - \frac{k}{a^2} + \frac{\Lambda}{3}, \tag{2.10}$$

which is called the first Friedmann equation.

Here ρ contains the energy density of matter and radiation, it is the time-time component of the energy-momentum-stress tensor (Peter & Uzan, 2009), and Λ is called the cosmological constant. The space components of Einstein's equations give Friedmann's second equation

$$\dot{\rho} + 3H(\rho + \mathcal{P}) = 0, \tag{2.11}$$

relating scale factor, density and pressure $\mathcal{P}$.

The energy density ρ is a sum of components with different equations of state. We model them as perfect fluids obeying $w\rho = \mathcal{P}$ with equation of state

[1] We use commas as a shorthand for partial derivatives with respect to the coordinates x, e.g. $g_{\alpha\beta,\nu} \equiv \partial g_{\alpha\beta} / \partial x_{\nu}$

parameter w. The most important components of ρ are the radiation density ρ_r (photons and neutrinos), the matter density ρ_m (baryonic and non-baryonic, e.g. visible and dark matter) and the dark energy density $\rho_{\rm DE}$. Matter in the universe can be modeled as pressure-less dust, i.e. $w_m = \mathcal{P}_m = 0$, equation 2.11 then implies $\rho_m \propto a^{-3}$. Radiation, on the other hand, has $\mathcal{P}_r = \rho_r/3$, giving $\rho_r \propto a^{-4}$. Standard cosmology assumes that dark energy is described by the cosmological constant, the equation of state is fixed at $w_{\rm DE} \equiv -1$, which gives a constant density (Dodelson, 2003).

We define the critical density $\rho_{\rm cr} \equiv 3H^2/(8\pi G)$ and the density parameters

$$\begin{aligned} \Omega_\Lambda &= \frac{\Lambda}{3H^2}, \\ \Omega_k &= -\frac{k}{H^2 a^2}, \\ \Omega_i &= \frac{\rho_i}{\rho_{\rm cr}}, \qquad \text{for } i = m,\, r, \end{aligned} \tag{2.12}$$

which turns the first Friedmann equation (eq. 2.10) into a constraint equation (Peter & Uzan, 2009):

$$\Omega_m + \Omega_r + \Omega_\Lambda + \Omega_k = 1, \tag{2.13}$$

where $\Omega_k \equiv 0$ in standard cosmology.

We will denote the value of any of these density parameters today ($a = 1$) as $\Omega_{i,0}$. Assuming the standard model of cosmology, recent measurements of the density parameters are presented in table 2.1 (from Planck Collaboration XIII, 2016). If allowed to vary, the same experiment constrains curvature to $|\Omega_{k,0}| \lesssim 5 \times 10^{-3}$.

Allowing for $k \neq 0$ is one of the most basic extensions and has not been ruled out by observations yet (Leonard et al., 2016). Most theories of inflation predict a very small amount of curvature in the late-time universe, e.g. slow-roll eternal inflation $\Omega_{k,0} < 10^{-4}$ (Guth et al., 2014) and false-vacuum eternal inflation $\Omega_{k,0} > -10^{-4}$ (Kleban & Schillo, 2012). This level of precision has not yet been achieved and likely requires strong assumptions or knowledge of dark energy, see e.g. chapter 5 or Leonard et al. (2016) for more information.

$\Omega_{\Lambda,0}$	$\Omega_{\mathrm{m},0}$	$\Omega_{\mathrm{r},0} \times 10^5$	H_0
0.691 ± 0.006	0.309 ± 0.006	9.21 ± 0.22	67.7 ± 0.5

TABLE 2.1: Parameter constraints from Planck Collaboration XIII (2016), with H_0 in units of km s^{-1} Mpc^{-1}. The error on $\Omega_{\mathrm{r},0}$ was calculated from the CMB temperature following Dodelson (2003). These results assume a flat universe.

Another extension to ΛCDM is to include more general dark energy models than Λ, which greatly affects curvature constraints. A basic model uses a first order Taylor expansion for its equation of state (called the CPL parametrization), $w_{\mathrm{DE}} = w_0 + z w_a/(1+z)$ (Linder, 2003; Chevallier & Polarski, 2001), but this is not enough to model all possible degeneracies that arise between curvature and dark energy with a general equation of state. Allowing for a comparably complex dark energy model, as well as for curvature, makes constraining either of them very difficult, if not impossible, with present data-sets. Model independent tests of curvature are discussed in e.g. Clarkson et al. (2007), Takada & Dore (2015) and Nesseris & Sapone (2014). In chapter 5 we examine the effects of the dark energy equation of state on curvature constraints with HIRAX. We consider dark energy with a general, piecewise constant redshift dependence as well as the CPL expansion.

2.1.2 Distance measures

To calculate the comoving distance to an object at $a(t)$, we start with the FLRW metric

$$0 = ds^2 = dt^2 - a^2 dx^2, \tag{2.14}$$

which yields $dt^2/a^2 = dx^2$ and thus

$$\chi \equiv \int_t^{t_0} dx = \int_t^{t_0} \frac{dt'}{a(t')} = \int_a^1 \frac{da'}{a'^2 H(a')}. \tag{2.15}$$

The maximum comoving distance anything could have traveled since the beginning of the universe, $\eta = \int_0^t \frac{dt'}{a(t')}$, is called *conformal time* or *comoving horizon*.

Observations of the angle subtended by objects with known physical size l (such objects are called standard rods) measure the angular diameter distance. It is defined as $D_{\rm A} = l/\phi$ where ϕ is the (small) subtended angle of the object. In order to relate this distance measure to the comoving distance, a cosmological model needs to be assumed:

$$D_{\rm A} = aS_k(\chi). \tag{2.16}$$

Here the function

$$S_k(\chi) = \frac{\sinh\left(\sqrt{\Omega_{k,0}}H_0\chi\right)}{H_0\sqrt{\Omega_{k,0}}}. \tag{2.17}$$

relates the the comoving radius χ of a sphere centered at $\chi = 0$ to its comoving surface $4\pi S_k(\chi)^2$, in other words $r = S_k(\chi)$. Equation 2.17 is valid for any sign of Ω_k and converges to $S_k = \chi$ for $\Omega_{k,0} \to 0$. Similarly to the angular diameter distance, the *radial* measurement of a standard rod is an extremely useful probe. Instead of the distance, it allows direct constraints on the redshift dependence of the Hubble rate via $d\chi/dz \sim 1/H(z)$. Combining measurements of radial and angular standard rods has an immense potential. As curvature enters equations 2.10 and 2.16 in distinct ways, its contribution can thus unambiguously be extracted if H and D_A are measured well enough on the same redshift range. See Blake & Glazebrook (2003), chapter 5, or the next section 2.2 or for more information.

There are other distance measures in cosmology, a very important example is the luminosity distance to an object of known absolute luminosity L. The relation between observed flux F, absolute luminosity, comoving and luminosity distance is $D_{\rm L} \equiv L/(4\pi F) = \chi/a$.

Constraining the redshift - distance relation, e.g. by measuring the redshifts to objects of known physical size or luminosity, is one of the most important probes of cosmology and has significantly contributed to the advancement and success of modern cosmology. Arguably the most well known example is the Nobel-prize winning work on type Ia supernovae, the first detection of the Universe's accelerated expansion Riess et al. (1998); Perlmutter et al. (1999). A more recent example is Conley et al. (2006).

2.2 Inhomogeneities and Anisotropies

While the universe is thought to be homogeneous and isotropic on the largest scales, small deviations from this arise due to cosmic structure formation. The clustering statistics of cosmic structure contain an immense amount of information on physics and processes in the history of the universe. Large and small scale structure surveys with planned radio and optical telescopes will facilitate the use of much of the great potential of this information. They promise to create precise maps of the matter distribution over vast volumes. Apart from being an important probe of the physics and cosmological model needed to describe their inhomogeneities and anisotropies, such maps can also provide cosmologists with a standard rod, the Baryon Acoustic Oscillations. These oscillations are a remnant of physics in the early universe and allow constraints on the redshift-distance and redshift-Hubble rate relation on a much larger range than ever probed before.

2.2.1 The 3-D power spectrum

Inhomogeneities can be characterized with the over-density $\delta(\vec{x}) = \rho(\vec{x})/\bar{\rho} - 1$, where $\bar{\rho}$ is the mean of a density $\rho(\vec{x})$. The power spectrum $P(k)$ is related to the Fourier transformed over-density $\delta(\vec{k})$ as

$$\langle \delta(\vec{k})\delta(\vec{k}') \rangle = (2\pi)^3 P(k) \delta^3(\vec{k} - \vec{k}'), \tag{2.18}$$

where δ^3 is the three-dimensional Dirac delta and angular brackets denote an average over the entire space (Dodelson, 2003). This definition imposes $\langle \delta(\vec{k})\delta(\vec{k}') \rangle = f(k = |\vec{k}|)$ and $\vec{k} = \vec{k}'$, which is true thanks to the translational and rotational invariance given by the principles of homogeneity and isotropy. Under the assumption that scale and time dependence can be separated into two factors, the primordial potential Φ_p and the late-time potential Φ can be related as

$$\Phi(\vec{k}, a) = \frac{9}{10} \Phi_p(\vec{k}) T(k) \frac{D(a)}{a}, \tag{2.19}$$

where the transfer function $T(k)$ describes the evolution of perturbations, and the growth function D describes the scale-independent growth. The growth

rate is defined as $f = d\log D/d\log a$ and the potential obeys $g_{ii} = a^2(1+2\Phi)$ $(i \neq 0)$. Neglecting the small contribution of radiation, the relation becomes

$$\delta(\vec{k}, a) = \frac{3}{5}\frac{k^2}{\Omega_m H_0^2}\Phi_p(\vec{k})T(k)D(a), \tag{2.20}$$

or in terms of the power spectra

$$P(k, a) = \left(\frac{3}{5}\frac{k^2}{\Omega_m H_0^2}T(k)D(a)\right)^2 P_\Phi(k), \tag{2.21}$$

with the power spectrum of the primordial potential P_Φ serving as the initial condition, derived from inflationary theory. We can now calculate the *root mean square* mass fluctuation within a sphere of radius R (Fan et al., 1997):

$$\sigma_R^2 = \frac{1}{2\pi^2}\int dk k^2 P(k) W_R^2(k), \tag{2.22}$$

where the window function W_R is the Fourier transformed top hat function with radius R. The parameter σ_8 is called the matter fluctuation at $R = 8\mathrm{h}^{-1}\mathrm{Mpc}$ and is often used to set the overall normalization of P.

As stated before, cold dark matter as well as dust have zero pressure and represent the overwhelming majority of matter in the universe. Without pressure to smooth out inhomogeneities, all modes that entered the horizon evolve identically (Dodelson, 2003). By definition, this evolution is described by the growth factor, which can be derived analytically, see Dodelson (2003). In order to obtain precise estimates of the transfer function T, however, numerical methods are necessary to solve the Einstein and Boltzmann equations. There exist publicly available codes giving accurate and computationally efficient results, e.g. *CMBFAST* Seljak & Zaldarriaga (1996) and *CAMB* Lewis et al. (2000). The main reference of this chapter, Dodelson (2003), presents interesting and pedagogic derivations of analytic results in the large and small scale limits.

2.2.2 Baryon Acoustic Oscillations

The speed of sound in the early universe plasma sets a fundamental limit to the maximum distance any acoustic wave could have traveled before

recombination. At recombination, the plasma cooled sufficiently to form the first neutral atoms, thus decoupling baryons and photons and preventing any further propagation of sound waves. This distance, $\sim$ 150 Mpc comoving distance (Eisenstein & Hu, 1998), is called the *sound horizon*, and is observable in the CMB (e.g. Spergel et al., 2007) and in galaxy clustering (Eisenstein et al., 2005; Cole et al., 2005) as a preferred clustering scale in real space (the acoustic peak), or as the so-called Baryon Acoustic Oscillations (BAO) in the matter power spectrum. Thanks to their large scale, the BAO remain in the linear regime since decoupling and are therefore a highly robust standard ruler even at low redshifts, normalizable with CMB data (Eisenstein et al., 2007, 1998; Hu et al., 1999; Wagner et al., 2008). For a good summary of the BAO in the CMB, see e.g. Hu & Dodelson (2002). In Padmanabhan & White (2009) it is demonstrated that the acoustic peak is both shifted and broadened during structure formation. These effects are well described by second order perturbation theory and are less than $\sim 1\%$. The BAO fraction $f_{\rm BAO}$ is defined by splitting $P(k)$ into a smooth and an oscillatory part, such that

$$P(k) = (1 + A f_{\rm BAO}(k)) P_{\rm smooth}(k), \tag{2.23}$$

with the BAO amplitude A. This separation is often done such that $f_{\rm BAO}$ has no smooth overall trend (Blake & Glazebrook, 2003; Bull et al., 2015b). Figure 2.1 shows the forecast constraints on $f_{\rm BAO}$ for HIRAX, a radio interferometer further described in section 4.1. Its range of sensitivity is optimized for BAO measurements in both angular and radial direction, thus allowing for simultaneous measurements of D_A and H down to a 1%-level. The H constraints are slightly better thanks to the good frequency resolution of 21cm intensity mapping experiments (see chapter 5).

2.2.3 The angular power spectrum

Expanding a function in terms of spherical harmonics is suitable especially on a spherical surface, e.g. the night sky, or the surface of the earth. The popular text book on electrodynamics Jackson (1999) contains a detailed introduction

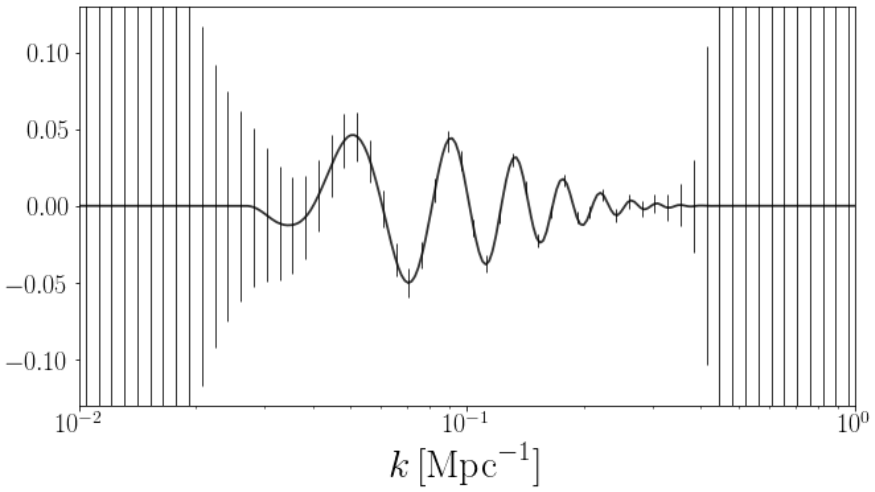

FIGURE 2.1: Fisher forecasted constraints on f_{BAO} for HIRAX. HIRAX is an interferometer optimized for BAO measurements, thus also putting tight constraints on D_A and H over a wide redshift range. This figure shows the combined constraint from all frequency bins. The forecasts presented in chapter 5 are derived from these BAO constraints, which are shown here for illustration. Further details and references are given there.

to this set of functions. Any function $\mathcal{V}(\hat{n})$, where $\hat{n}$ is a unit vector, can be written as a sum with coefficients $a_{\ell m}$:

$$\mathcal{V}(\hat{n}) = \sum_{\ell=1}^{\infty} \sum_{m=-\ell}^{\ell} a_{\ell m} Y_{\ell m}(\hat{n}), \tag{2.24}$$

with the complete set of orthonormal functions $\{Y_{\ell m} |\ \ell \in \mathbb{N},\ m \in \mathbb{Z},\ -\ell \leq m \leq \ell\}$, the spherical harmonics. It is common to refer to the coefficients $a_{\ell m}$ as multipole moments, and to ℓ as multipole. The notation $\sum_{\ell,m}$ will be used as a shorthand for $\sum_{\ell=1}^{\infty} \sum_{m=-\ell}^{\ell}$ from now on. Inverting eq. 2.24 is straight forward, giving

$$a_{\ell m} = \int d\Omega Y^*_{\ell m}(\hat{n}) \mathcal{V}(\hat{n}), \tag{2.25}$$

where the superscript * denotes complex conjugation.

Due to isotropy and homogeneity, it is impossible predict the value of a specific $a_{\ell m}$ in cosmology, but one can calculate the distribution from which it is statistically drawn. While the mean value is always zero, $\langle a_{\ell m} \rangle = 0$, the variance, which we call angular power spectrum C_ℓ, is given by

$$\langle a_{\ell m} a^*_{\ell' m'} \rangle = \delta_{\ell \ell'} \delta_{m m'} C_\ell, \tag{2.26}$$

where again the delta function $\delta_{ij} = 1$ if $i = j$ and 0 otherwise. To derive the C_ℓ's in a practical example, we follow Battye et al. (2013) (note the change of notation). Starting from any kind of 3D overdensity $\delta\tilde{T}(\vec{x}, z)$, e.g. a normalized temperature fluctuation, its projection on the sky can be calculated as

$$\delta T(\hat{n}) = \int_0^{\infty} dz W(z) \delta\tilde{T}(\chi(z)\hat{n}, z), \tag{2.27}$$

where the projection kernel W describes the selection of sources which are projected. This varies depending on the survey and the observed objects, e.g. for a galaxy number count survey, W is given by the normalized number density of detected galaxies LSST Science Collaboration et al. (2009), or for intensity mapping it is often taken to be a top hat window function, see e.g. chapter 7. We first transform to Fourier space $\delta\tilde{T}(\chi(z)\hat{n}, z) = \int \frac{d^3k}{(2\pi)^3} \tilde{T}(\vec{k}, z) e^{i\chi(z)\hat{n}\vec{k}}$ and use the Rayleigh plane-wave expansion with spherical Bessel functions j_ℓ and

unit vector $\hat{k}$, $e^{i\vec{k}\vec{x}} = 4\pi \sum_{\ell,m} i^\ell j_\ell(kx) Y_{\ell m}(\hat{n}) Y^*_{\ell m}(\hat{k})$, to rewrite eq. 2.27 as

$$\delta T(\hat{n}) = 4\pi \sum_{\ell,m} i^\ell \int dz W(z) \int \frac{d^3k}{(2\pi)^3} \delta\tilde{T}(\vec{k}, z) j_\ell(k\chi(z)) Y^*_{\ell m}(\hat{k}) Y_{\ell m}(\hat{n}). \quad (2.28)$$

The expressions for the multipole moments and their variance become lengthy,

$$a_{\ell m}(\hat{n}) = 4\pi i^\ell \int dz W(z) \int \frac{d^3k}{(2\pi)^3} \delta\tilde{T}(\vec{k}, z) j_\ell(k\chi(z)) Y^*_{\ell m}(\hat{k}), \quad (2.29)$$

$$\begin{aligned} \langle a_{\ell m} a^*_{\ell' m'} \rangle = \int dz W(z) \int dz' W(z') \int \frac{d^3k}{(2\pi)^3} \int \frac{d^3k'}{(2\pi)^3} \\ \times \left\langle \delta\tilde{T}(\vec{k}, z) \delta\tilde{T}(\vec{k}', z') \right\rangle j_\ell(k\chi(z)) j_{\ell'}(k'\chi(z')) Y^*_{\ell m}(\hat{k}) Y^*_{\ell' m'}(\hat{k}'), \end{aligned} \quad (2.30)$$

but the variance can be simplified using the orthonormality of the spherical harmonics, and assuming that $\delta\tilde{T}$ is a biased tracer of the dark matter field. The latter means that we express its power spectrum in terms of the dark matter power spectrum $P_{\rm cdm}$ (see eq. 2.18), i.e. $\langle \delta\tilde{T}(\vec{k}, z) \delta\tilde{T}(\vec{k}', z') \rangle \equiv (2\pi)^3 \delta(\vec{k} - \vec{k}') b(z) b(z') P_{\rm cdm}(k) D(z) D(z')$, with the tracer bias b. This gives

$$\begin{aligned} C_\ell = \frac{2}{\pi} \int dz b(z') W(z) D(z) \int dz' b(z') W(z') D(z') \\ \times \int k^2 dk P_{\rm cdm}(k) j_\ell(k\chi(z)) j_\ell(k\chi(z')). \end{aligned} \quad (2.31)$$

We use Limber's approximation (Loverde & Afshordi, 2008) to estimate the k integral for large ℓ as

$$\int k^2 dk P_{\rm cdm}(k) j_\ell(k\chi) j_\ell(k\chi') \approx P_{\rm cdm}\left(\frac{\ell + 1/2}{\chi}\right) \frac{\delta(\chi - \chi')}{\chi^2}, \quad (2.32)$$

and change variables $dz' = H_0 E(z') d\chi'$ to finally write

$$C_\ell = H_0 \int dz E(z) \left(\frac{b(z) W(z) D(z)}{\chi(z)} \right)^2 P_{\rm cdm} \left(\frac{\ell + 1/2}{\chi(z)} \right). \tag{2.33}$$

In a more general situation, the quantity of interest is not normalized, in which case a redshift dependent factor needs to be included, for example by using $b(z) \to b(z)\bar{T}(z)$, with $\bar{T}$ the mean of $\tilde{T}$ at redshift z. In section 4.4.3, $\bar{T}$ and b are discussed in the case of 21cm intensity mapping. See below for a brief discussion of this in the context of galaxy number counts, which allows to write equation 2.33 for the large-scale, angular galaxy power spectrum.

2.2.4 The galaxy bias

The galaxy bias $b_{\rm g}$ linearly relates the clustering of galaxies to that of the underlying dark matter background. The galaxy power spectrum is often split into two summands, $P_{\rm g}(k) = P_{\rm 1h} + P_{\rm 2h}$, where the one-halo term $P_{\rm 1h}$ describes the clustering of galaxies within the same dark matter halo, and the two-halo term $P_{\rm 2h}$ is the power spectrum of galaxies populating different halos. On scales larger than the size of a typical halo, $P_{\rm 1h}$ becomes negligible, $P_{\rm g}(k) \approx P_{\rm 2h}$. In what follows, we also ignore the internal structure of halos, which is reasonable on large scales and allows for an easy relation between the galaxy power spectrum and halos. Using the halo mass function $n_{\rm h}(m)$, the halo bias $b_{\rm h}$ and the mean number of galaxies within a halo of mass m $\langle N_{\rm g}|m\rangle$, one can write (Cooray & Sheth, 2002)

$$P_{\rm g}(k) = P_{\rm cdm} \underbrace{\left(\int dm n_{\rm h}(m) b_{\rm h}(m) \frac{\langle N_{\rm g}|m\rangle}{\bar{n}_{\rm g}} \right)^2}_{b_{\rm g}^2}, \tag{2.34}$$

where the factor on the right side is the galaxy bias. The mean number of galaxies is given by $\bar{n}_{\rm g} = \int dm n_{\rm h}(m) \langle N_{\rm g}|m\rangle$, and the halo bias can be calculated from gravitational collapse, giving results that agree well with simulations (Sheth & Tormen, 1999):

$$b_{\rm h} = 1 + \frac{q\nu - 1}{\tilde{\delta}} + \frac{2p/\tilde{\delta}}{1 + (q\nu)^p}. \tag{2.35}$$

Here $\nu(m, z) = \tilde{\delta}^2(z)/\sigma^2(m)$, $\tilde{\delta}(z) = \delta_{\rm c}/D(z)$, $\delta_{\rm c} = 1.686$ and the parameters $(p, q) = (0.3, 0.707)$. Using this galaxy bias, along with an appropriate window function $W(z)$ representing the galaxy population and magnitude threshold of the telescope, equation 2.33 describes the large scale angular clustering of galaxies (compare equation 7.14). Throughout this work, we will use two similar functions to calculate the galaxy bias. Chapter 6 takes $b_{\rm g} = 1 + 0.84z$ from LSST Science Collaboration et al. (2009) and in chapter 7 we use fits from Alonso et al. (2015b).

3 Forecasting methods

All genuine research presented in this thesis assesses the applicability of novel data analysis techniques on data obtained from yet to be finished instruments. Predicting or forecasting the constraining power of a given instrument-data analysis combination requires a set of statistical tools; the ones used for this thesis are reviewed here. After starting with Bayes theorem, an introduction to Fisher formalism will then present a quick way to estimate performance. Markov Chain Monte Carlo methods, giving much better precision at the cost of increased computation demand, are reviewed at the end of this chapter.

3.1 Bayes' theorem

The conditional probability $p(A|B)$, i.e. the likelihood of A given that B is true, can be rewritten in terms of $p(B|A)$ and the prior probability $p(B)$ using Bayes theorem (Kendall et al., 1987). This is useful when $p(B|A)$ is comparably easy to calculate, but $p(A|B)$ is not directly accessible, often the case in data analysis. It allows easy estimation of the likelihood of a cosmological model with parameters Θ being true, given a data set y. We write Bayes' theorem as

$$p(\Theta|y) = \frac{p(y|\Theta)p(\Theta)}{\int p(y|\Theta)p(\Theta)d\Theta}. \tag{3.1}$$

The prior probability $p(\Theta)$ is generally motivated either by results from other experiments, a physical understanding of the model, or set to be uninformative (see e.g. Jeffreys prior (Jeffreys, 1946)). The denominator in eq. 3.1 is a scaling factor, often called the *evidence* for the model, and only has to be considered when different models are compared. It is irrelevant for this work, where a model-independent approach is desired. In chapter 5, we exclusively used flat priors, i.e. priors which are zero outside a set parameter range, and equal to one inside.

The likelihood $\mathcal{L} \equiv p(y|\Theta)$ is generally calculated as (see also eq. 5.8):

$$\mathcal{L} = \exp\left(-\frac{1}{2}(\xi - \mu)^{\mathrm{T}}\mathrm{C}^{-1}(\xi - \mu)\right), \tag{3.2}$$

where ξ is a vector containing all measurements of observables and μ contains the model prediction of the observables given the fiducial model Θ. The covariance matrix C is determined by the total measurement error (instrumental and cosmic variance contributions).

3.2 Fisher matrix formalism

Fisher formalism is very useful for quick estimates of posterior parameter distributions, under the assumption that all involved probability distributions are Gaussian. A brief and concise starting guide can be found in Coe (2009). The Fisher matrix is simply the inverse of the parameter covariance matrix and can be calculated as

$$\mathcal{F}_{jk} = (C^{-1})^{jk} = \sum_b \frac{1}{\sigma_b^2}\frac{\partial f_b}{\partial \Theta^j}\frac{\partial f_b}{\partial \Theta^k}, \tag{3.3}$$

where $f_b(\Theta)$, for $b \in \{1, ..., B\}$, is the model prediction of an observed quantity y_b with Gaussian uncertainty σ_b and Θ denotes the fiducial parameters. We can also relate the Fisher matrix to the probability of the parameters given the data, $p(\Theta|y_b)$ (see eq. 3.1), as

$$\mathcal{F}_{jk} = -\left\langle \frac{\partial^2 \log p(\Theta|y_b)}{\partial\Theta^j \partial\Theta^k} \right\rangle_b. \tag{3.4}$$

A Fisher matrix can easily be transformed to a new parameter set Θ' using the transformation matrix $M_{jk} = \frac{\partial\Theta_j}{\partial\Theta'_k}$,

$$\mathcal{F}' = M^{\mathrm{T}}\mathcal{F}M. \tag{3.5}$$

The diagonal of the covariance matrix contains the Gaussian uncertainties, with all other parameters marginalized. If one instead wants to fix a certain parameter, i.e. assume perfect prior knowledge on it, its row and column

have to be removed from the Fisher matrix before inverting. Fisher matrices from different data-sets can be added to yield the combined constraints, i.e. $\mathcal{F} = \sum_i \mathcal{F}_i$. Their ease of use and computational speed makes Fisher matrices a great rough estimation method for parameter constraint forecasts, but only if they are expected to follow Gaussian distributions. A nice application in a cosmological context is presented in Albrecht et al. (2009). In more complex situations, or when more precision is desired, Markov Chain Monte Carlo methods deliver a computationally efficient means to sample and access the full posterior distribution.

3.3 Markov Chain Monte Carlo: a tool for forecasting and parameter estimation

Markov Chain Monte Carlo (MCMC) methods significantly improve the computational efficiency of complex model analyses in Bayesian statistics Kass et al. (1998). The range of applications is vast and spreads across many disciplines of science, data analysis in modern cosmology is almost unthinkable without it (see e.g. are Abbott et al., 2018; Planck Collaboration XIII, 2016; Lewis & Bridle, 2002; Audren et al., 2013). Chapter 5 in this work heavily relies on MCMC methods to derive model independent constraints on curvature. Without the efficient use of MCMC methods and algorithms, such an analysis would be extremely difficult, if not unfeasible. This section presents a brief overview of the method we used.

When forecasting for future instruments, the experimental covariance matrix (eq. 3.2) can also be derived using Fisher formalism. Depending on the complexity of the model, calculating eq. 3.2 can still be computationally challenging, making direct sampling very difficult. Furthermore, complex models often include a set of nuisance parameters α in Θ. Their distribution is not interesting itself and they need to be marginalized in order to obtain the relevant posterior. Denoting the parameters without the nuisance parameters as $\bar{\Theta}$, the exact result of a marginalized posterior is obtained by integrating

$$p(\bar{\Theta}|y) = \int p(\Theta, \alpha|y) d\alpha. \tag{3.6}$$

Given a large set of nuisance parameters α, this integral can be extremely difficult to compute. Fortunately, an MCMC method automatically provides samples from the marginalized distribution (Foreman-Mackey et al., 2013).

3.3.1 Sampling distributions

A widely known and easy to implement MCMC sampling algorithm is the Metropolis-Hastings algorithm (Hastings, 1970; Metropolis et al., 1953). From a starting point θ_0 in parameter space, it uses random numbers to sample the *jumping distribution*, which sets the step size to the candidate θ' for the first iteration θ_1. Any candidate θ' for sample $i+1$ is accepted or rejected based on the acceptance ratio $p(\theta'|y)/p(\theta_i|y) = r$. The candidate is accepted if either $r \geq 1$ or if a random number in the interval $[0, 1]$ is less than or equal to r. This measure prevents the algorithm from permanently remaining at a local maximum in the distribution. A Metropolis-Hastings algorithm set up with a well chosen starting point and jumping distribution will generate samples which quickly converge to the desired distribution after a burn-in period, which we discuss in more detail in subsection 3.3.2. However, finding a good jumping distribution is one of the major challenges. This distribution is parametrized with so-called tuning parameters, which often have to be hand-picked, and when ill chosen, they significantly increase the autocorrelation (see subsection 3.3.2) and burn-in time. Depending on the dimensionality of the problem, and the shape of the distribution, hand tuning the parameters for a Metropolis-Hastings based algorithm may quickly become impractical. Attempts to computationally determine the optimal tuning parameters often require long burn-in phases, where smaller samples are used to optimize the parameters (e.g. Dunkley et al., 2005; Widrow et al., 2008). For this work we used the openly available *python* package called *emcee* (Foreman-Mackey et al., 2013), which is based on the affine-invariant ensemble sampler proposed by Goodman & Weare (2010). An immense benefit of this sampler is the low number of only 1 or 2 tuning

parameters, as compared to $\propto N^2$ for Metropolis-Hastings with an N-dimensional model. Another major advantage is the simultaneous sampling of the distribution using a number of K walkers, which evolve independently. This again improves the autocorrelation and allows for efficient multiprocessing, distributing the walkers on different CPUs.

3.3.2 Convergence

With many convenient software packages available, MCMC samplers are easy and quick to set up. Arguably the trickiest part about it is judging the performance of an algorithm, and deciding on the necessary number of steps to sample the distribution sufficiently and accurately. A good summary of this topic is given in Cowles & Carlin (1996). This subsection elaborates on the techniques used in chapter 5.

Amongst many other options to quantify convergence, the Gelman Rubin test (Gelman & Rubin, 1992; Brooks & Gelman, 1998) stands out as a tool to help gauge the necessary number of elements in an MCMC sample. It exploits the presence of multiple chains to evaluate their convergence by comparison, making it particularly useful combined with the *emcee* package, which runs K walkers at the same time. We define $\bar{\sigma}^2$ as the mean of the variances of all chains, i.e. $\bar{\sigma}^2 = \frac{1}{K}\sum_{i=1}^{K}\hat{\sigma}_i^2$, where each walker has variance $\hat{\sigma}_i^2$. The posterior mean of all chains is $\bar{\mu} = \frac{1}{K}\sum_{i=1}^{K}\hat{\mu}_i$, with $\hat{\mu}_i$ the mean of walker i. If we write the variance of the mean of individual walkers as $V = \frac{1}{K-1}\sum_{i=1}^{K}(\hat{\mu}_i - \bar{\mu})^2$, the true full variance σ^2 can be estimated with a weighted sum

$$\bar{\sigma}_+^2 = \frac{n-1}{n}\bar{\sigma}^2 + V. \tag{3.7}$$

Following Brooks & Gelman (1998), the sampling variability of the overall mean $\bar{\mu}$ can be accounted for using a pooled posterior variance estimate $\hat{V} = \bar{\sigma}_+^2 + V/K$. The potential scale reduction factor (PSRF) is then defined as the ratio of the pooled posterior variance and the mean variance of all walkers,

$$\hat{R}_c = a\frac{\hat{V}}{\bar{\sigma}^2}. \tag{3.8}$$

The correction due to $a = (\hat{d}+3)/(\hat{d}+1)$ is usually small because the degrees of freedom estimate $\hat{d}$ tends to be very large at convergence. The PSRF is close to unity for a converged posterior, and can thus be used as a diagnostic. Depending on the requirements, the imposed conditions can be more or less stringent. It is important to remember, though, that even the common choices of $\hat{R}_c < 1.2$ or 1.1 are not always enough to guarantee convergence. It can help to also monitor $\bar{\sigma}^2$ and $\hat{V}$ separately and to keep track of $\hat{R}_c$ as a function of iteration number, as it may not be monotonously decreasing (Brooks & Gelman, 1998).

Once a chain is converged and long enough, the unconverged burn-in sample has to be removed. The remainder may still suffer from significant autocorrelation, which can lead to a bias towards tighter constraints. The autocorrelation time τ (e.g. Sokal, 1997) is defined as the minimum number of steps between two points in order for them to be fully uncorrelated. It is a useful concept to diagnose and correct for autocorrelation, and to estimate the necessary number of steps in the chain. The autocorrelation function $\bar{A}(t)$ for a finite chain f_i with n elements can be estimated as

$$\bar{A}(t) = \frac{1}{n-t}\sum_{i=1}^{n-t}(f_i - \mu)(f_{i+t} - \mu), \tag{3.9}$$

where μ denotes the mean of the chain, and we normalize $A(t) \equiv \bar{A}(t)/\bar{A}(0)$. Note that in practice, it is more efficient to compute A in Fourier space than by using equation 3.9 directly. The integrated autocorrelation time is

$$\tau = \sum_{t=-\infty}^{\infty} A(t) \tag{3.10}$$

and can be estimated in different ways; we used the software package *emcee*. A sample directly generated by MCMC methods generally suffers from non-negligible autocorrelation, which can be removed by 'thinning the chain by the correlation time τ', i.e. discarding all but the τ'th elements in the chain. Assuming that the number of elements in the chain is large enough, $n \gg \tau$, the resulting sample should be free from autocorrelation for $t \neq 0$ and thus accurately represent the true distribution. The concept of the autocorrelation

time is only useful when applied to a converged chain.

4 Radio cosmology

The Planck measurement of the CMB has almost reached the cosmic variance limit on large scales, but mapping of the more late-time structure in the universe suffers from significantly larger uncertainties, if any data is available at all. Planned optical telescopes, like *LSST* and *Euclid*, aim to vastly extend the volume of previous galaxy surveys. Their range is limited, however, by the requirement of resolving individual galaxies, which needs high sensitivities and thus long observation times, and by dust, which is a major limitation for optical surveys at higher redshifts. The addition of large radio telescopes to the set of cosmological instruments will supply vital information on a much deeper redshift range. This will open many observational windows, calling for new data analysis methods and strategies. One of these strategies is intensity mapping of the 21cm line emission of neutral hydrogen. Intensity mapping does not resolve individual sources but detects integrated emission of all objects within a given pixel. This technique will facilitate observations of particularly large volumes at the expense of weaker angular resolution.

Section 4.1 briefly reviews the planned radio and optical instruments used for this work. Then, sections 4.2, 4.3 and 4.4 summarize different types of planned radio surveys and corresponding cosmological probes, following Square Kilometre Array Cosmology Science Working Group et al. (2018) as a main reference. Special emphasis is put on 21cm intensity mapping, which forms the basis of chapters 5 - 7.

4.1 Planned radio and optical instruments for cosmology

Among the planned radio telescopes, this work specifically focuses on the Hydrogen Intensity and Real-time Analysis eXperiment (HIRAX), and the

Square Kilometre Array[1] (SKA). These complimentary instruments will share their site in the Karoo desert in South Africa. HIRAX is planned as a set of 1024 6 m radio dishes arranged in a close-packed square grid. This interferometer will operate on a frequency range of 400-800 MHz, which corresponds to a redshift range of 0.8-2.5. The design is primarily optimized to extract the BAO feature from the 3D power spectrum of 21cm intensity maps; see chapter 5 for more information. In contrast to more conventional telescope designs, HIRAX will not have a tracking machinery. It will instead use the earth's rotation to observe stripes of the sky by drift scanning, see also 5.2.2. After a certain amount of time, all dishes are manually rotated and pointed to a new direction, thus observing another stripe of the sky. Thanks to the large field of view, HIRAX is also expected to detect many transients, like Fast Radio Bursts (FRB), which are still poorly understood (Newburgh et al., 2016b), but might be used for cosmology (Walters et al., 2018).

The SKA is an immense international project. Initiated in the 1990s, it is planned to consist of individual antennas spread out across many countries in southern Africa and Australia. After completion of its precursors and pathfinders, first observations with a partial array of SKA phase 1 (SKA1) are scheduled to take place until 2020. An upgrade to SKA phase 2 (SKA2) during the 2020s is designed to increase collection area 10-fold (Garrett et al., 2010; Ekers, 2012; Huynh & Lazio, 2013). There are several pathfinder projects, like the Australian SKA Pathfinder[2] (ASKAP) (Schinckel et al., 2012), the Hydrogen Epoch of Reionization Array[3] (HERA) (DeBoer et al., 2017), the Murchison Widefield Array[4] (MWA) (Lonsdale et al., 2009) and the successor of the Karoo Array Telescope (KAT), MeerKAT[5] (Jonas & MeerKAT Team, 2016), whose construction in the Karoo in South Africa was finished in 2018. Apart from intensity mapping and astrophysical probes, it can also provide unrivaled HI galaxy surveys in the pre-SKA1 era

[1] www.skatelescope.org
[2] www.atnf.csiro.au/projects/askap
[3] reionization.org
[4] www.mwatelescope.org
[5] www.ska.ac.za/science-engineering/meerkat

(Cunnington et al., 2018). Section 4.4.4 documents Fisher forecasts provided for the MeerKLASS cosmological survey proposal (Santos et al., 2016).

SKA1 LOW, located in Western Australia, is a planned aperture array of 512 stations in a large core with three spiral arms, giving it a maximum baseline of 65 km, observing at 50 - 350 MHz. Its main science drivers are the Epoch of Reionization and pulsar physics (G. Labate et al., 2017).

This work puts special emphasis on SKA1 MID, located in the Karoo in South Africa. Observing at frequencies ranging from 350 to 1750 MHz, it will consist of all 64 MeerKAT dishes with 13.5 m diameter, whose construction has already been finished, and 133 SKA dishes with 15 m diameter (Square Kilometre Array Cosmology Science Working Group et al., 2018). MeerKAT is used as an independent instrument until completion of SKA1 MID, with which it will then be merged. The dish signals will be both correlated with each other (interferometry) and used in the so-called 'single dish mode', simply adding the autocorrelation signals of each one. The former allows resolving extremely small scales, while the latter makes scanning of large scale modes possible, which is vital for cosmological surveys, e.g. probing the matter power spectrum. The much larger dish size, as well as the longer separation of dishes (baselines) and the smaller total number of dishes compared to HIRAX, give SKA1 MID a very different set of properties, strengths and weaknesses, albeit observing much of the same frequency range. In particular, while HIRAX' interferometric resolution is optimized for a BAO detection, it misses larger scales due to its limited field of view. Observations in single dish mode do not suffer from this kind of restraints, large scale coverage being determined simply by the survey area. Therefore larger scales can be mapped by SKA1 MID in single dish mode, but also when working in interferometer mode it adds information on the smallest scales, thanks to extremely long baselines and large dish sizes. In order to maximize scale and frequency coverage, combining information obtained from several instruments like SKA and HIRAX is imperative and allows to extract the maximum amount of information from the data acquired; see chapter 7 for an analysis that greatly benefits from the combination of SKA1 MID and HIRAX. For more information on radio astronomy, Wilson et al. (2013)

provides a thorough resource, especially on the mentioned single dish observations, interferometry and aperture arrays.

It is also very advantageous to combine radio data sets with optical galaxy surveys. Although this work is focused on radio cosmology, analyses using real and simulated 'mock' data from optical surveys are additionally presented. Existing galaxy clustering data is used from data release III of the Sloan Digital Sky Survey[6] (SDSS) Sánchez et al. (2017), which allows BAO constraints from its galaxy counts with precise spectroscopic redshift information. Data collection with its dedicated 2.5 m optical telescope, located at the Apache Point Observatory[7] in New Mexico, started in 2000 and is ongoing still (Gunn et al., 2006). Among the large number of planned optical surveys, the Large Synoptic Survey Telescope[8] (LSST) stands out due to its large overlap of survey area with the SKA. LSST is a single large instrument with an 8.4 m primary mirror, currently under construction in Chile, with planned completion in 2019. Its extremely large field of view will make it a pristine survey telescope, locating billions of distant galaxies and measuring their photometric redshifts (LSST Science Collaboration et al., 2009).

4.2 Radio continuum

By using the integrated emission of a source over a very broad frequency range, a radio continuum survey is able to detect and resolve comparably weak and distant sources, and to a large extent even resolves shapes of galaxies. The main sources of radio continuum emission are active galactic nuclei and star formation (Wilman et al., 2008). Inevitably, such a survey lacks the redshift precision of an emission line survey, but photometric redshifts can be obtained up to a redshift of $z_{\mathrm{photo-max}} \sim 2.0$ (Square Kilometre Array Cosmology Science Working Group et al., 2018). Useful observables are the distribution of shapes of objects and number count statistics, thus the following probes stand out particularly for a radio continuum survey:

[6] www.sdss.org
[7] www.apo.nmsu.edu
[8] www.lsst.org

- *Weak gravitational lensing*
  The path of light propagating through the universe is bent by the matter it encounters, resulting in image distortions. The term weak lensing refers to the case of images distorted so weakly that a single lensed source does not allow for a detection of the deflection. An introduction to this statistical measurement is presented in Dodelson (2003). The very long observed wavelengths in the radio generally make it very hard to resolve shapes of individual sources. However, a large instrument like SKA1 can meet the resolution requirements needed for competitive weak lensing analyses in the radio (Square Kilometre Array Cosmology Science Working Group et al., 2018). Apart from autocorrelating cosmic shear measurements of a radio telescope, cross-correlations to the optical can be used to reduce systematic effects on galaxy shape measurements from either survey. This is based on the the assumption that shape measurements in the optical and radio do not suffer from the same systematic effects. Such a cross-correlation analysis retains most of the constraining power of the individual surveys, where the forecasts for SKA1 are comparable to the performance of experiments such as the Dark Energy Survey (DES) (Dark Energy Survey Collaboration et al., 2016). Weak lensing is sensitive to the geometry of the universe, and therefore an especially useful tool to constrain the equation of state of dark energy (Patel et al., 2010). An introduction to weak gravitational lensing can be found in Bartelmann & Schneider (2001); while Patel et al. (2010) presents an exploratory analysis in the radio.

- *Angular correlation*
  Without the requirement of resolving shapes, the angular correlation of radio galaxy number counts brings insight into the large scale distribution of galaxies, and thus of the underlying dark matter distribution. The resulting parameter constraints do not always improve upon those from presently available data like the CMB, but do provide a largely independent measurement (Camera et al., 2012; Ferramacho et al., 2014).

- *Cosmic dipole*
  Slight deviations from large scale isotropy of the universe are expected to be dominated by the proper motion of the solar system with respect to the CMB. However, other effects, like large scale structures, can contribute (Bengaly et al., 2018). From CMB data alone, it is difficult to distinguish between different contributions to the dipole, but a radio continuum survey can provide important independent measurements and thus allows us to disentangle the sources of the dipole signal. Available data seems to indicate good agreement of the dipole directions, but a considerable discrepancy, a factor of $2 - 5$, in the amplitude. See e.g. Blake & Wall (2002); Colin et al. (2017), and for a detailed study with SKA1 and SKA2 see Bengaly et al. (2018).

4.3 21cm galaxy clustering

The hyperfine 21cm line emission of neutral hydrogen (HI), caused by a forbidden spin flip of the electron, is of extremely low intensity. Detecting and resolving the 21cm line emission of galaxies is difficult even with next generation telescopes and thus limited to comparably low redshifts (e.g. $z \lesssim 0.7$ in the case of SKA1 and $z \lesssim 2.0$ for full SKA2 (Yahya et al., 2015)). In spite of this limitation, HI galaxy surveys will likely be very competitive and could provide the best dark energy figure of merit of all current or planned large-scale surveys (Yahya et al., 2015). On top of the positions and precise redshifts, which will be useful for clustering statistics, the sizes and 21cm line width of a subset of sources will also be available. The Tully-Fisher relation allows direct estimates of peculiar velocities from the 21cm line profile (Tully & Fisher, 1977; Koda et al., 2014), and can thus be used to sample the peculiar velocity field of galaxies, which among other things is a particularly useful tool to test theories of modified gravity, see e.g. Ivarsen et al. (2016). While it is still unclear how well sizes of galaxies can be measured with HI surveys, such data could be used to test the so-called Doppler magnification, which is an effect similar to weak gravitational

lensing, but caused by the peculiar motion of galaxies (Bonvin, 2008; Bonvin et al., 2017; Bacon et al., 2014).

When source sizes and line widths are unavailable, such a survey still allows us to measure the 3D power spectrum of galaxies to great precision in both angular and radial direction. An extremely interesting observable effect in the HI galaxy power spectrum is the Baryon Acoustic Oscillation (BAO) feature, discussed in subsection 2.2.2. Optical spectroscopic experiments have already detected BAO in the clustering of galaxies, but at different redshift ranges and sky coverage, see e.g. Alam et al. (2017); Kazin et al. (2014).

Redshift Space Distortions (RSD) are another interesting small-scale effect introducing anisotropic clustering in redshift space Percival et al. (2011); Kaiser (1987). RSDs occur on smaller scales than BAOs, but are expected to be detectable with HI galaxy redshift surveys. Measurements of this anisotropy allow for constraints in the galaxy bias and the linear growth rate $f(z)$ (Square Kilometre Array Cosmology Science Working Group et al., 2018)).

4.4 21cm intensity mapping

As stated before, the HI 21cm line emission is of extremely low intensity. Even next generation radio telescopes will be able to resolve individual sources only at low redshifts, unless survey geometries are kept narrow and deep. To detect this for large scale structure surveys at higher redshifts, it is necessary to use integrated emission of several sources within a given pixel, a technique called *21cm intensity mapping* (HI IM) (Battye et al., 2004; Peterson et al., 2005; Furlanetto et al., 2006). Trading angular resolution for larger survey volumes, the radial resolution of such a survey remains excellent thanks to the characteristic 21cm line. For the advancement of precision in cosmology, larger volumes are deemed more important than high angular resolution. Mapping them will allow us to test many extensions of ΛCDM cosmology, which often produce degeneracies in current data sets, see especially chapter 5 for a discussion on how mean spatial curvature can be measured in a cosmology with an entirely free dark energy equation of state.

For a review of the current state of emission line intensity mapping, see Kovetz et al. (2017).

Large single dish instruments like the Parkes telescope and the Green Bank telescope have already made detections using cross-correlations with other surveys (e.g. Anderson et al., 2018; Masui et al., 2013), and an upper limit on auto-correlation (Switzer et al., 2013), but most dedicated 21cm intensity mapping experiments are radio arrays using interferometry. The instruments used for the forecasts in this work are presented in subsection 4.1: HIRAX, MeerKAT and SKA1 MID. Another interesting example is the Canadian Hydrogen Intensity Mapping Experiment[9] (CHIME), which is similar to HIRAX, but in the northern hemisphere. It uses cylindrical reflectors and has no moving parts. The Hydrogen Epoch of Reionization Array[10] (HERA) is a specialized instrument for high-redshift 21cm intensity mapping, sharing the site with MeerKAT in the Karoo. It consists of a hexagonal grid of 14 m dishes made from PVC pipe stays covered in wire mesh.

4.4.1 Cosmological probes

The nature of a single HI intensity map has similarities to the CMB: both are intensity maps, not resolving individual sources. Thus a straightforward approach to analyzing HI IM data is to adjust techniques known from CMB analysis, like the angular power spectrum.

Following Battye et al. (2013), the observed mean brightness temperature of 21cm radiation can be written as

$$\bar{T}_{\rm obs}(z) = 44\mu{\rm K}\left(\frac{\Omega_{\rm HI}(z)h}{2.45\times10^{-4}}\right)\frac{(1+z)^2}{E(z)}, \tag{4.1}$$

with $E(z) = H(z)/H_0$, the Hubble rate H (eq. 2.10), Hubble constant H_0 and $h = H_0/100$ km sec^{-1} Mpc^{-1}. The HI density parameter $\Omega_{\rm HI} \equiv \rho_{\rm HI}/\rho_{\rm cr}$ (compare eq. 2.12) and HI bias $b_{\rm HI}$ are major uncertainties in the model, with

[9] https://chime-experiment.ca/
[10] https://reionization.org/

a more recent estimate of

$$\Omega_{\rm HI} b_{\rm HI} = 4.3 \pm 1.1 \times 10^{-4} \tag{4.2}$$

at 68% confidence at $z = 0.8$ (Switzer et al., 2013). Under the assumption of neutral hydrogen being a linear tracer of the dark matter field, the HI bias $b_{\rm HI}$ is used to relate the HI over-density to that of dark matter. The 3D HI power spectrum can then be written as

$$P_{\rm HI}(k, z) = \bar{T}_{\rm obs}(z)^2 b_{\rm HI}^2 \frac{k^3 P_{\rm cdm}}{2\pi^2}, \tag{4.3}$$

with the wavenumber k and the dark matter power spectrum $P_{\rm CDM}$ (Battye et al., 2013). The 3D power spectrum is a very useful observable especially for surveys probing large volumes. Working at the map level, we expand in terms of spherical harmonics and simplify using the Limber approximation (Limber, 1954; Loverde & Afshordi, 2008):

$$C_\ell^{\rm HI} = \frac{H_0}{c} \int dz E(z) \left(\frac{W(z) \bar{T}_{\rm obs}(z) D(z) b_{\rm HI}}{r(z)} \right)^2 P_{\rm cdm} \left(\frac{\ell + 1/2}{r(z)} \right), \tag{4.4}$$

with the redshift window function $W(z)$, the growth function $D(z)$ and the physical distance r (Battye et al., 2013). Measuring $C_\ell^{\rm HI}$ not only allows us to constrain the parameters controlling eq. 4.4, but by measuring the BAO feature in $P_{\rm cdm}$ (in angular and radial direction), both the Hubble rate $H(z)$ and the angular diameter distance $D_{\rm A}$ can be constrained over a large redshift range. Such measurements are well suited for constraining dark energy (Chang et al., 2008; Bull et al., 2015a; Bull et al., 2015b) or spatial curvature, as shown in chapter 5. The SKA1 MID with its long baselines will not be able to fully cover the angular BAO scales needed (Bull et al., 2015b), however, it will contribute angular as well as full radial BAO data to specialized BAO detection instruments like HIRAX or CHIME (Newburgh et al., 2016a; Bandura et al., 2014).

Probes of ultra large scale effects require single dish instruments with very high survey speeds for voluminous surveys, approaching or exceeding horizon scales (Bonvin et al., 2006; Challinor & Lewis, 2011; Yoo, 2010). One

example of such an effect is the scale dependent correction of the HI clustering bias $b_{\rm HI} \propto f_{\rm NL}/k^2$ due to primordial non-Gaussianities of the local type $f_{\rm NL}$ (Dalal et al., 2008; Matarrese & Verde, 2008). Cosmic variance is a major contributor to the error in large scale structure measurements and fundamentally limits the attainable precision, but there exist tricks to improve accuracies of some observables beyond this limit. One example is the multi-tracer technique, first proposed in Seljak (2009). It exploits observations of different tracers of the dark energy background to cancel out cosmic variance. In chapter 6, this technique is tested for a combination of simulated SKA HI IM and LSST optical galaxy survey data. Apart from potentially detecting primordial non-Gaussianities, this technique could allow measurements of General Relativistic effects, which manifest themselves mostly on extremely large scales and thus suffer significantly from cosmic variance (Alonso et al., 2015b). Cross-correlations between the HI intensity distribution and optical galaxies are also useful for other probes and analysis methods, as they are free of all systematic errors which affect one of the surveys alone.

Intensity mapping of the HI 21cm emission line will provide a plethora of other probes. One hopes to test neutrino masses and several inflationary models of the early universe (Villaescusa-Navarro et al., 2015). Intensity mapping experiments will also attend to one of the biggest open questions in cosmology: the nature of dark matter. At intermediate and small scales, the so-called free streaming of warm dark matter models is expected to produce a suppression of power in the power spectrum. Deep and narrow surveys at low frequencies could measure this characteristic suppression and thus provide independent constraints on warm dark matter (Viel et al., 2012; Carucci et al., 2015).

The accuracy of photometric redshifts in future optical galaxy surveys is crucial for their constraining power, the availability of precise spectroscopic redshifts remaining limited. Cross-correlating a galaxy survey with an HI intensity survey could potentially improve photometric redshift determination (Alonso et al., 2017; Cunnington et al., 2018; Square Kilometre Array Cosmology Science Working Group et al., 2018). Although

individual sources are not resolved in intensity mapping, cross-correlations between a foreground HI IM and a background map, e.g. an optical galaxy survey, can be used for gravitational lensing analyses. For example, it could be possible to detect the cosmic magnification effect, whereby the foreground HI distribution would increase or decrease the apparent magnitude of background galaxies, thus introducing a cross-correlation signal in well separated redshift slices. This idea is examined in chapter 7.

4.4.2 Foreground contamination

A successful HI IM survey will have to overcome a number of technical and theoretical challenges, from data infrastructure, instrument calibration, radio frequency interference, to foreground removal and data analysis. For the work presented in this thesis, the removal of cosmic foreground radiation is important, especially because it can leave residuals and because it removes some of the long wavelength radial modes of the signal (Liu & Tegmark, 2011; Thyagarajan et al., 2015; Bowman et al., 2009). There are different sources of galactic and extra-galactic emission in the frequency range observed by a 21cm experiment, most importantly galactic synchrotron emission (GSE), free-free (galactic and extra galactic) emission and extra galactic point sources (de Oliveira-Costa et al., 2008; Liu et al., 2009a). The dominant contribution to foregrounds is GSE. Foregrounds exceed the cosmological HI signal by $4-5$ orders of magnitude; however, it is possible to clean signals leaving only small foreground residuals. The publicly available package `CRIME`[11] (Alonso et al., 2014) is useful to generate simulated foreground maps of five different sources (unpolarized and polarized) GSE, galactic and extragalactic free-free emission and extragalactic radio point sources.

Isotropic foregrounds are simulated (in `CRIME`) using the power spectrum from Santos et al. (2005)

$$C_\ell(\nu_1,\nu_2) = A\left(\frac{l_{\rm ref}}{l}\right)^\beta \left(\frac{\nu_{\rm ref}^2}{\nu_1\nu_2}\right)^\alpha \exp\left(-\frac{\log^2(\nu_1/\nu_2)}{2\xi^2}\right), \tag{4.5}$$

[11] `https://github.com/damonge/CRIME`

where A, α, β and ξ are model parameters, given in Alonso et al. (2014) (ξ is the frequency-space correlation length of the foreground emission). Radio galaxies, active galactic nuclei and 'normal' galaxies will contribute to foreground (or background) emission as point sources. Several surveys map unresolved sources at the wavelengths relevant for HI intensity mapping and can be used to estimate their angular power spectra (e.g. Di Matteo et al., 2002). As pointed out in Alonso et al. (2014), extragalactic point sources likely trace the same matter distribution as the HI signal, which potentially leads to a correlation between foregrounds and signal. Ionized electrons produce both a galactic and extragalactic low-frequency radio background via free-free emission (e.g. Oh, 1999; Tegmark et al., 2000), which significantly contributes to intensity mapping foregrounds.

Anisotropic synchrotron emission is by far the dominant contribution, caused by high energy cosmic ray electrons accelerated by the galactic magnetic field (Rybicki & Lightman, 1979; Pacholczyk, 1970). In `CRIME` it is calculated by extrapolating the Haslam map (Haslam et al., 1982) to the required frequency, and adding structure (the Haslam map has poor resolution) from a Gaussian realization of the power spectrum in 4.5. The intensity of unpolarized synchrotron emission follows a simple power law,

$$T_{\mathrm{sync}}(\nu) \propto \frac{1}{\nu^{\beta}}, \tag{4.6}$$

with the spectral index β depending on the line of sight. The frequency dependence of polarized synchrotron emission, however, is affected by the Faraday rotation effect, introducing much more fluctuation with frequency and making it more difficult to model (see fig. 4.1). Any leakage of this into the unpolarized signal, due to instrumental issues, would make the synchrotron radiation much harder to subtract from the cosmological signal. In the absence of extensive data on polarized synchrotron emission and the structure of the galactic magnetic field, modeling based on observations alone is difficult (Haverkorn et al., 2008; Testori et al., 2008; Wolleben et al., 2006). Other options include using existing models and the statistical properties of synchrotron emission (Waelkens et al., 2009; Alonso et al., 2014). Figure 4.1 shows the frequency dependence of the cosmological signal as well as all five

types of foregrounds simulated with `CRIME`. The severity of polarization leakage depends on instrumental calibration, but generally increases towards the galactic plane (Alonso et al., 2014).

Foreground removal techniques usually rely on the spectral smoothness of foregrounds. Most recent studies suggest that using frequency information in a line of sight approach is more promising than the use of angular information (Harker et al., 2009; Gleser et al., 2008; Harker et al., 2010; Liu et al., 2009b; Wang et al., 2006). Several methods exist, e.g. independent component analysis, polynomial fitting or principal component analysis (PCA). As a simple example, the foregrounds can be fitted with low order polynomials and subtracted from the signal, leaving the cosmological signal's small scale variations largely intact. In chapter 6 we used PCA with the publicly available package[12] `fg_rm`. The frequency covariance matrix can be computed by averaging over the number N_θ of lines of sight (Alonso et al., 2015a)

$$C_{ij} = \frac{1}{N_\theta} \sum_{n=1}^{N_\theta} T(\nu_1, \hat{n}_n) T(\nu_2, \hat{n}_n), \tag{4.7}$$

where $T(\nu, \hat{n})$ is the brightness temperature for line of sight $\hat{n}$ at frequency ν. This matrix is then diagonalized, $U^{\mathrm{T}} C U = \mathrm{diag}(\lambda_1, ..., \lambda_{N_\nu})$, where N_ν is the number of frequency bins. The number N_{fg} of largest eigenvalues λ_i is identified, and the matrix U_{fg} is constructed to contain only the corresponding columns of U. The foreground maps s are then calculated by projecting the brightness temperature maps on this basis of eigenvectors, i.e.

$$s = U_{\mathrm{fg}}^{\mathrm{T}} T. \tag{4.8}$$

Using an appropriate number N_{fg}, subtracting these maps removes most of the foreground contamination. The cosmological signal is left largely intact, albeit long-wavelength radial modes are lost. See chapter 6 for a discussion of this problem. The small foreground residuals might still be non-negligible in some cases. They are potentially problematic in the HI auto correlation power spectrum, but they are very unlikely to remain in cross-correlations with optical galaxies. Furthermore, depending on the aggressiveness of the

[12] `http://intensitymapping.physics.ox.ac.uk/codes.html`

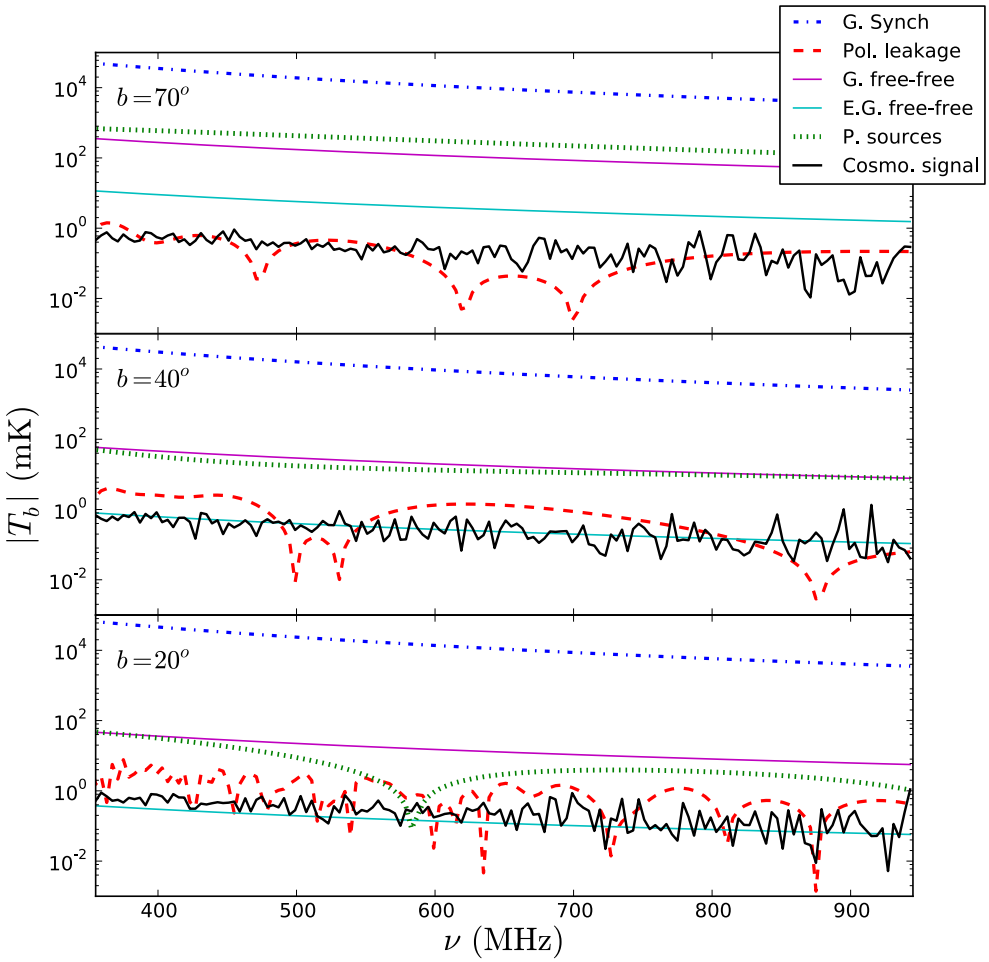

FIGURE 4.1: Picture taken from Alonso et al. (2014). It shows the frequency dependence of the foreground and cosmological signals (T_b) along lines of sight with different galactic latitudes, given in the top left corner of each panel. Note that polarization leakage varies much more at latitudes close to the galactic plane, which makes its removal difficult. This is due to the frequency-dependent Faraday rotation affecting polarized synchrotron emission.

foreground routine used, large scale modes of the radial HI power spectrum are inevitably lost. Even though much of the cosmological information is contained in the shorter wavelengths and the large scale angular modes remain unaffected by foreground cleaning, this is still the limiting factor in certain analyses. See a discussion of foreground residuals as well as loss of modes in the multi-tracer technique in chapter 6. A comparison of different foreground removal methods can be found in Alonso et al. (2015a).

4.4.3 The 21cm signal model

The HI bias $b_{\rm HI}$ relates the linear dark matter overdensity to the large scale structure of neutral hydrogen. After reionization, hydrogen in the intergalactic gas is ionized by radiation from the first sources in the universe. Large amounts of HI only remain inside comparably dense collapsed structures (damped Lyα absorbers, DLA) within galaxies, shielding them from the ionizing radiation (e.g. Pritchard & Loeb, 2012). Therefore, the HI bias can be related to the halo bias similarly to the galaxy bias, but instead of the mean number of galaxies in a given halo, one uses the mean mass of neutral hydrogen in a halo $M_{\rm HI}(m)$, and instead of the mean number density of galaxies, the density $\rho_{\rm HI} = \int dm n_{\rm h}(m) M_{\rm HI}(m)$. This leads to the simple expression for the hydrogen bias on large scales (Padmanabhan et al., 2015)

$$b_{\rm HI} = \int dm n_{\rm h}(m) b_{\rm h}(m) \frac{M_{\rm HI}(m)}{\rho_{\rm HI}}, \tag{4.9}$$

where $b_{\rm h}$ is given in equation 2.35 and $n_{\rm h}$ is the halo mass function.

The mean observed brightness temperature of HI is given by the redshifted 21cm line emission brightness temperature at late times (e.g. Battye et al., 2013)

$$\bar{T}_{21}^{\rm obs} = \frac{\bar{T}_{21}^{\rm em}}{1+z} = \frac{3A_{21}\hbar c^3}{16 f_{\rm em}^2 k_{\rm B} M_{\rm H}} \frac{(1+z)\rho_{\rm HI}(z)}{H(z)}, \tag{4.10}$$

where $k_{\rm B}$ is Boltzmann's constant, $\nu_{\rm em} = 1420.4$ MHz is the rest frame emission frequency, $\hbar$ is the reduced Planck constant, c is the speed of light, $M_{\rm H}$ is the mass of the hydrogen atom and A_{21} is the spontaneous emission coefficient of the 21cm transition. For simplicity, $\bar{T}_{21}^{\rm obs}$ will often be referred to as $\bar{T}_{21}$.

Both the HI brightness temperature and bias are still poorly constrained from observations. In this work, different fitting functions will be used. The fits vary slightly, but are all valid for comparably low redshifts ($z \lesssim 3.7$) and linear scales. Chapter 5 and 6 use Bull et al. (2015b) for the modeling of $b_{\rm HI}$ and $\bar{T}_{21}$, while in chapter 7 we use fits from Alonso et al. (2015b) for the hydrogen bias, and Santos et al. (2017) for the brightness temperature. For a good summary of the physics governing the 21cm signal before and after reionization, see e.g. Pritchard & Loeb (2012).

4.4.4 Forecasts for MeerKLASS

The Large Area Synoptic Survey for MeerKAT (MeerKLASS) is proposed to cover ~ 4000 deg^2 over 4000 hours and could potentially provide the first ever measurement of the BAO feature using the 21cm intensity mapping technique.

We used the same Fisher forecasting code as in chapter 5, i.e. an adapted version of the open-source python script provided in Bull et al. (2015b). The forecasts are made for MeerKAT with 64 dishes of 13.5 m diameter and the redshift dependent system temperatures of the L and UHF-band receivers. The set of redshift dependent cosmological parameters is the matter fluctuation σ_8 at 8 h^{-1}Mpc times the growth rate f, the Hubble rate H, the angular diameter distance D_A and the BAO amplitude A, as defined in Bull et al. (2015b), marginalizing all other parameters. For more information on the Fisher forecasting technique, see chapter 3.

To find the optimal survey area for the relevant set of parameters, we forecasted for different combinations of redshift binning, survey area and integration time. Figures 4.2 to 4.5 plot signal to noise as a function of survey area for three different integration times (red: 1000, blue: 2000 and yellow: 4000 hours) and different redshift bins in each figure. For low redshift bins, maximal survey area is always beneficial, i.e. for all parameters and integration times. For higher redshift bins, this behavior changes. For lower integration times especially, a smaller survey area $S_{\rm area}$ of $4000 \leq S_{\rm area} \leq 10000 {\rm deg}^2$ is preferred for BAO detection, angular diameter distance and $f\sigma_8$. Long surveys with 4000 hours integration time always benefit from using the maximum sky area possible. The black dashed vertical

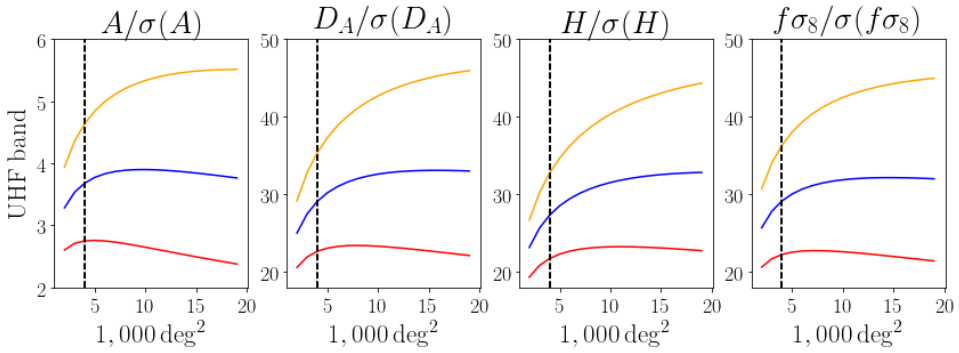

FIGURE 4.2: Forecast parameter signal to noise as a function of survey area for a wide high-redshift bin with z from $0.46 \rightarrow 0.86$. The red, blue and yellow lines correspond to 1000, 2000 and 4000 hours integration time respectively. This is the highest redshift bin considered, using the UHF detector for MeerKAT. For 1000 hours all parameters benefit from survey areas ≤ 10000.

lines in each panel correspond to the survey area proposed for MeerKLASS Santos et al. (2017).

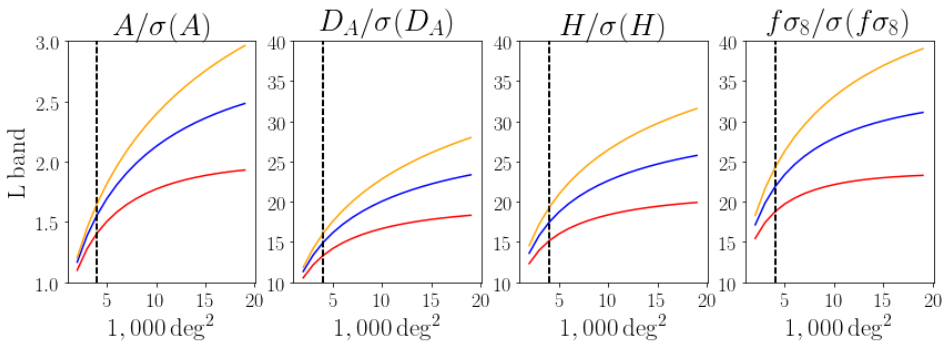

FIGURE 4.3: Forecast parameter signal to noise as a function of survey area for a narrow redshift bin with z from $0.12 \rightarrow 0.22$. The red, blue and yellow lines correspond to 1000, 2000 and 4000 hours integration time respectively. In this case high survey area always yields better constraints.

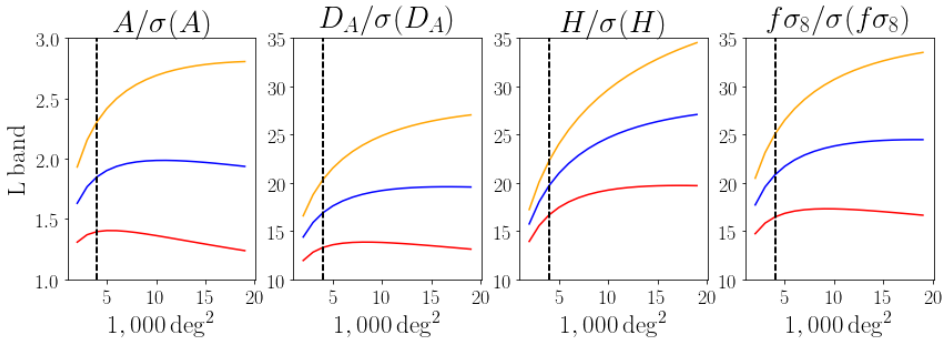

FIGURE 4.4: Forecast parameter signal to noise as a function of survey area for a narrow redshift bin bin with z from $0.47 \rightarrow 0.57$. The red, blue and yellow lines correspond to 1000, 2000 and 4000 hours integration time respectively.

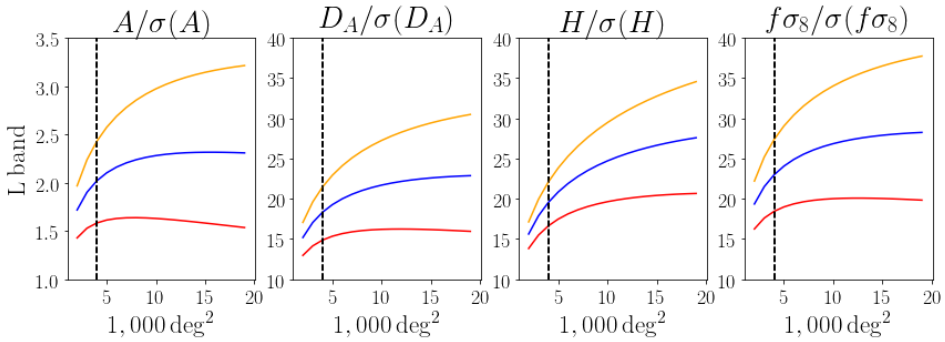

FIGURE 4.5: Forecast parameter signal to noise as a function of survey area for a narrow redshift bin with z from $0.35 \to 0.45$. The red, blue and yellow lines correspond to 1000, 2000 and 4000 hours integration time respectively. Here all parameters except the BAO amplitude prefer maximal survey areas.

5 Model-independent curvature determination with 21cm intensity mapping experiments

This work was published in the journal Monthly Notices of the Royal Astronomical Society (MNRAS) (Witzemann et al., 2018) and also made available online on the arXiv with number 1711.02179. I lead this project, provided all results, calculations and derivations, figures, as well as the majority of text. The collaborators M. G. Santos, A. Weltman and C. Clarkson guided the project and its presentation, defined the scientific rationale and edited the text. M. Spinelli provided advice on statistics and MCMC methods. P. Bull contributed technical advice on the methods, calculations and coding, guidance on presentation and checking of results as well as the choice of figures. In addition to editorial work he also provided text in the introduction and throughout the work. He and M. Santos were mainly responsible for noticing the bias in the analysis method from Knox (2006) (see fig. 5.3).

Recent precision cosmological parameter constraints imply that the spatial curvature of the Universe is essentially dynamically negligible – but only if relatively strong assumptions are made about the equation of state of dark energy (DE). When these assumptions are relaxed, strong degeneracies arise, making it hard to disentangle DE and curvature and thereby degrading the constraints. In this chapter, we show that forthcoming 21cm intensity mapping experiments such as HIRAX are ideally designed to carry out model-independent curvature measurements, as they can measure the clustering signal at high redshift with sufficient precision to break many of the degeneracies. We consider two different model-independent methods,

based on 'avoiding' the DE-dominated regime and on non-parametric modeling of the DE equation of state respectively. Our forecasts show that HIRAX will be able to improve upon current model-independent constraints by around an order of magnitude, reaching percent-level accuracy even when an arbitrary DE equation of state is assumed. In the same model-independent analysis, the sample variance limit for a similar survey is another order of magnitude better.

5.1 Introduction

Most viable models predict that only a very small amount of curvature should remain after the end of inflation – smaller even than the Hubble-scale curvature perturbations generated by quantum fluctuations. While some theories can generate observable amounts of curvature, they tend to either be somewhat contrived (e.g. see Bucher et al., 1995; Cornish et al., 1996), or are likely to be accompanied by large-scale anomalies that would be visible in the CMB (Aslanyan & Easther, 2015). Furthermore, several major classes of inflationary theories explicitly predict that curvature should be small. False vacuum eternal inflation would be ruled out by a detection of the curvature density parameter at the $\Omega_{\rm K} < -10^{-4}$ level, for example, while slow-roll eternal inflation would be ruled out if $\Omega_{\rm K} > +10^{-4}$ (Kleban & Schillo, 2012; Guth & Nomura, 2012).

Recent cosmological parameter constraints, most notably from the Planck CMB temperature and polarization spectra combined with baryon acoustic oscillation (BAO) constraints (Planck Collaboration XIII, 2016), have placed upper limits on curvature of $|\Omega_{\rm K}| < 5 \times 10^{-3}$ (95% CL) – still a factor of 50 in precision away from being able to put any serious pressure on eternal inflation (Vardanyan et al., 2009; Leonard et al., 2016). However, this figure is only achieved after making strong assumptions about the nature of dark energy (DE), i.e. that it behaves exactly like a cosmological constant, with an equation of state of $w = -1$. In fact, the equation of state of DE remains unknown, with many candidate theories predicting slightly different equations of state that can vary substantially with redshift (e.g. Huterer & Peiris, 2007; Marsh et al., 2014; Raveri et al., 2017).

When w is allowed to vary, the uncertainty increases on all parameters, as the data must now constrain several additional degrees of freedom. A common choice of parametrization, $w(a) \approx w_0 + w_a(1-a)$, introduces only two additional degrees of freedom, but more general 'non-parametric' analyses (e.g. see Nesseris & Sapone, 2014) can introduce many more. Many observables also depend on combinations of cosmological functions, like the Hubble rate, for which there is at least a partial degeneracy between $w(z)$ and $\Omega_{\rm K}$ (since, at the background level, an arbitrary DE equation of state can partially mimic the redshift scaling of curvature). This goes beyond the well-known 'geometric degeneracy', in which $\Omega_{\rm K}$ and $\Omega_{\rm DE}$ are degenerate when constrained by the primary CMB power spectrum alone – even probes that constrain distances or the Hubble rate at multiple redshifts are susceptible to some (typically strong) degree of correlation between $\Omega_{\rm K}$ and w (Clarkson et al., 2007; Hlozek et al., 2008). The degeneracies that exist in distances and the Hubble rate pull in opposing directions however, implying that a combined measurement, using the BAO feature or similar, can reduce the degeneracy significantly – even with no assumptions on $w(z)$, as we show here (see also Takada & Dore, 2015).

It is also possible to sidestep the problem of modeling $w(z)$ entirely, if one is willing to make a relatively mild assumption about the nature of DE. If the energy density of DE becomes negligible at some point in the past, i.e. $\Omega_{\rm DE}(z) \to 0$ beyond some $z > z_M$, it is possible to construct combinations of distance measures such that the DE-dependent part cancels out (Knox, 2006). In principle, this results in an observable that depends only on the matter and curvature contributions to the Friedmann equation at $z > z_M$, sufficiently deep into the matter-dominated regime. For typical values of cosmological parameters, matter domination occurs at $z \gtrsim 2$, and so only high-redshift probes such as the Lyman-alpha forest or 21cm intensity mapping (IM) can be used for this test.

21cm intensity mapping is a relatively new technique that measures the combined 21cm spectral line emission from many unresolved galaxies in each pixel (Kovetz et al., 2017). By trading angular resolution for spectral resolution and sensitivity, one can rapidly survey large cosmological volumes

while retaining most cosmological information on large scales. Since the underlying galaxy distribution is a biased tracer of the cosmic matter distribution, so too are the measured intensity maps. By using these in a similar way to other galaxy clustering observables (e.g. for BAO measurements: Chang et al., 2008; Bull et al., 2015a; Villaescusa-Navarro et al., 2017), one can measure distances out to significantly higher redshift than a typical optical galaxy survey (Bull et al., 2015b). This is especially true of 21cm IM, which uses the 21cm line from neutral hydrogen (HI) as a tracer. Since HI is ubiquitous in the universe out to relatively high redshift, and since radio telescopes can readily be built to cover very large frequency (and thus redshift) ranges, 21cm IM is well-suited to performing large, high-redshift cosmological surveys – and thus testing curvature in a model-independent way.

In this chapter, we study the ability of forthcoming 21cm IM experiments to constrain curvature in a model-independent way. Our particular focus is on the *Hydrogen Intensity and Real-time Analysis eXperiment* (HIRAX; Newburgh et al., 2016b), a radio interferometer currently under construction in South Africa. We assume a Planck 2015 flat ΛCDM fiducial cosmology throughout, with $\Omega_{\rm K} = 0$, $\Omega_{\rm M} = 0.316$, $\Omega_b = 0.049$, $\Omega_{\rm rad} = 9.13 \times 10^{-5}$, and $h = 0.67$ (Planck Collaboration XIII, 2016).

5.2 Forecasting for HIRAX

5.2.1 Noise power spectrum

The closely packed square dish arrangement of HIRAX creates a particularly high density of short baselines. We assume a square grid of 32×32 points with a separation of 7 m (6 m dish diameter + 1 m free space in between). For such a set up, the baselines range from 7 m to ~ 307 m. In what follows, we neglect the geographical location (i.e. longitudinal coordinates) and assume an observation pointed at the zenith and at HIRAX' mean observational frequency of $\bar{\nu} = 600$ MHz. From the square grid it is straight forward to count the number of dish pairs separated by a distance x, denoted by $N(x)$. We transform variables from physical distance x to unit-less

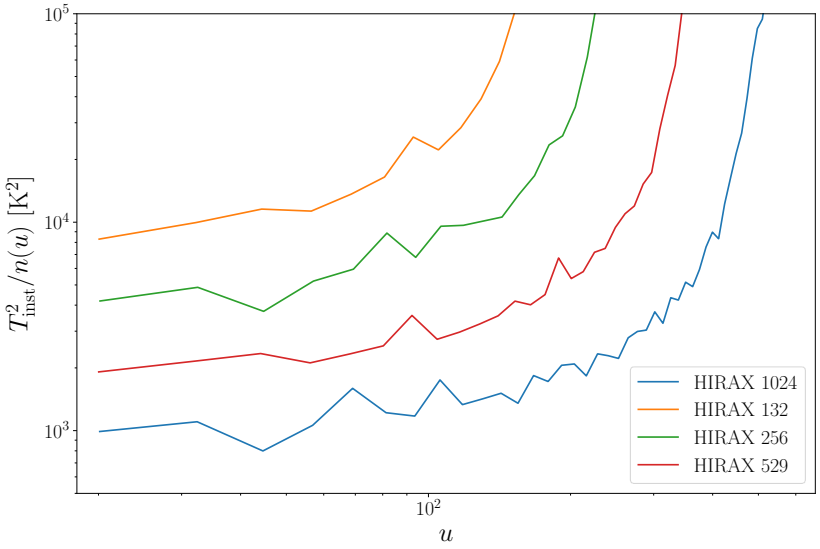

FIGURE 5.1: A comparison of $T^2_{\rm inst}/n(u)$, which is proportional to the instrumental noise, for the different HIRAX setups considered. The mean observing frequency is set to $\nu = 600$ MHz.

$u = x\bar{\nu}/c$, with the speed of light c, and calculate the baseline density n in these discrete coordinates as $n(u) = N(u)/(\pi((u + \Delta u)^2 - u^2))$, where Δu denotes the difference between two adjacent baselines u. We follow Bull et al. (2015b) to calculate the noise properties of HIRAX with this baseline density $n(u)$ and to derive the corresponding Fisher forecasts, see fig. 5.1. The noise power spectrum is calculated as

$$C^N = \frac{T^2_{\rm sys}}{\nu_{21} t_{\rm tot}} \frac{\lambda^4 S_{\rm area}}{A_e^2 F_{\rm fov}} \frac{1}{n(u)}, \tag{5.1}$$

where $T_{\rm sys}$ is the system temperature, ν_{21} is the rest frame frequency of the 21 cm line emission, $t_{\rm tot}$ is the total integration time, λ the observation wavelength, the field of view is calculated as $F_{\rm fov} = (\lambda/D_{\rm dish})^2$, $A_{\rm e}$ is the effective collecting area and $S_{\rm area}$ denotes the survey area. Figure 5.1 shows the inverse baseline density times the instrument temperature squared, which is proportional to the instrument noise, for HIRAX with 1024, 529, 256 and 132 dishes.

5.2.2 Drift scanning

The dish mounts of HIRAX are designed to be simple and cheap, without a tracking machinery. It will rely on drift scanning, i.e. the earth's rotation, combined with manual changes of the pointing angle, to observe an extremely large sky area of up to 15000 deg^2. The pointing direction will be changed once the corresponding stripe of the night sky is mapped with the required depth. The width of a stripe corresponds to the beam width of HIRAX, $\Delta\Theta = \Theta_{\mathrm{BEAM}}$. The length of the stripe depends on the observation time per day, the time per pointing t_p, and on the pointing declination in celestial coordinates. We assume 12 hours observation per day (observation fraction $f_{\mathrm{obs}} = 0.5$), i.e. observation only during nighttime. For a pointing on the celestial equator, at the same time every day, the stripe length Φ will be:

$$\Phi = \begin{cases} 2\pi\left(f_{\mathrm{obs}} + \frac{t_p/\mathrm{days}-1}{365-1}(1-f_{\mathrm{obs}})\right) & t_{\mathrm{p}} < 1 \text{ a} \\ 2\pi & t_{\mathrm{p}} \geq 1 \text{ a}, \end{cases} \tag{5.2}$$

which follows from basic geometry and celestial mechanics. Here $2\pi f_{\mathrm{obs}}$ is the stripe length of one single day, and $2\pi(t_p/\mathrm{days}-1)(1-f_{\mathrm{obs}})/(365-1)$ ensures $\Phi(t_p \equiv 365 \text{ days}) = 2\pi$ for $0 < f_{\mathrm{obs}} \leq 1$. With the beam width Θ and the declination of the pointing dec, the covered survey area of one pointing of t_p days is $\Phi\Theta\cos(\mathrm{dec})$. For a given survey strategy, this can be used to determine the appropriate date to manually rotate the dishes to a new pointing direction.

5.2.3 Survey optimization

We investigate the optimal survey strategy for curvature measurements with HIRAX. This is generally dependent on the model of dark energy and on the set of priors used. Figure 5.2 shows the normalized curvature constraint as a function of survey area for four different dark energy scenarios using the simple w_0, w_a parametrization and a fixed integration time of one year. The use of informative priors, here the DETF Planck priors from Albrecht et al. (2006), shifts the optimal survey area to significantly larger areas. Also allowing more freedom for dark energy, in this case by marginalizing both w_0 and w_a, shifts the optimal survey towards larger areas.

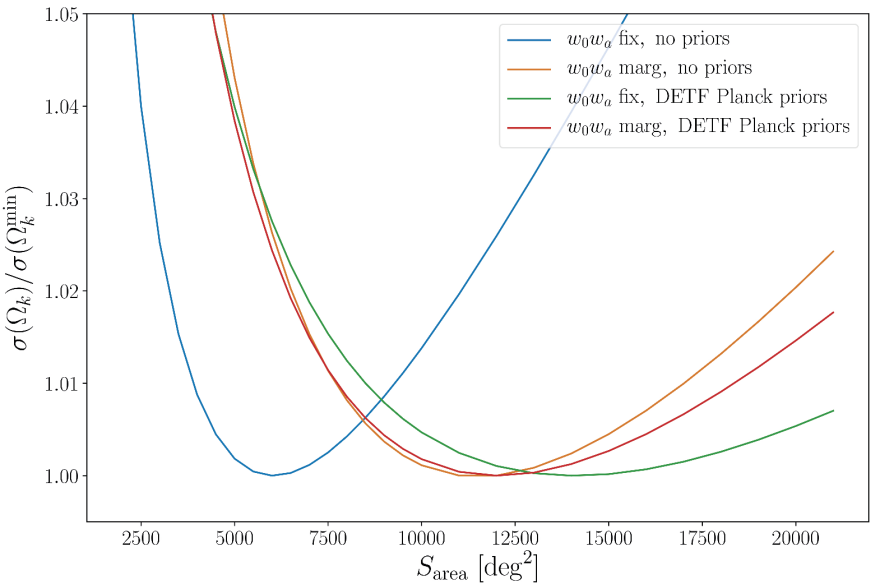

FIGURE 5.2: Optimizing the survey area with respect to the Ω_k forecasts. The optimum greatly depends on the model and priors used, but in most cases considered here it lies around $S_{\rm area} \sim 13000$ [deg]^2.

5.3 Curvature measurements in the presence of dark energy

We now present two different methods for obtaining curvature constraints that are independent of the assumed dark energy model, at least in principle. The first (Sect. 5.3.1) is based on constructing combinations of observables that do not depend on the low redshift, dark energy-dominated regime. The second (Sect. 5.3.2) uses a non-parametric approach to modeling the DE equation of state (EOS), marginalizing over its value in many redshift bins to produce curvature constraints that are independent of any assumed functional form for $w(z)$. For comparison, we also compare with a simple, commonly used 2-parameter dark energy model in Sect. 5.3.3.

5.3.1 Avoiding the dark energy era

One way of obtaining model-independent curvature constraints is to try to avoid the DE era entirely. We extend the approach described in Knox (2006)

to derive a combination of distance measures that is linearized in the spatial curvature, $k \equiv -\Omega_{\rm K} H_0^2$, and which is relatively independent of the dark energy contribution to those distances.

In a FLRW universe with line element $ds^2 = -dt^2 + a^2 dr^2/(1-kr^2)$, the comoving distance is given by $\chi = \int_0^r dr'/(1-kr'^2)$. The series expansion of $r(\chi, k)$ for small k is then $r \approx \chi - \frac{\chi^3 k}{6} + \mathcal{O}(k^2)$, regardless of the sign of k. We identify the coordinate distance $r = \tilde{D}_A(\chi, k) = D_A/a$, where $\tilde{D}_A$ is the comoving angular diameter distance, so that $\tilde{D}_A(\chi, k) \approx \chi - \chi^3 k/6$ to first order in k. The comoving distance is additive, i.e. $\chi_{\rm OL} = \chi_{\rm OM} + \chi_{\rm ML}$, where $\chi_{\rm OL}$ is the comoving distance from the observer to the last scattering surface (LSS), $\chi_{\rm OM}$ is the comoving distance from the observer to an intermediate redshift $z_{\rm M}$, where we assume that dark energy can be neglected, and $\chi_{\rm ML}$ is the distance from $z_{\rm M}$ to the LSS. Solving $\tilde{D}_{\rm OL} = \tilde{D}_A(\chi_{\rm OL}, k) \approx \chi_{\rm OL} - \chi_{\rm OL}^3 k/6$ for k gives, to first order,

$$k = 6\left(\frac{\tilde{D}_{\rm OM} + \chi_{\rm ML} - \tilde{D}_{\rm OL}}{(\tilde{D}_{\rm OL})^3 - (\tilde{D}_{\rm OM})^3}\right), \tag{5.3}$$

where $\tilde{D}_{\rm OM}$ and $\tilde{D}_{\rm OL}$ denote the comoving angular diameter distances from the observer to $z_{\rm M}$ and the LSS respectively. Both are directly observable, but $\chi_{\rm ML}$ is not. (Note that Eq. 5.3 differs from the Knox (2006) result by a minus sign.)

To obtain curvature constraints using this method, we use the Planck Collaboration XIII (2016) measurement of $\tilde{D}_{OL}$, and the HIRAX forecasts or SDSS measurements (Sánchez et al., 2017) of $\tilde{D}_{\rm OM}$, plus simple error propagation, to estimate the error on k. We can then approximate $\chi_{\rm ML}$ by neglecting curvature and DE for $z > z_M$, to give

$$\begin{aligned} \chi_{\rm ML} &\approx H_0 \int_{z_{\rm M}}^{z_*} dz/\sqrt{\Omega_{\rm M}(1+z)^3 + \Omega_{\rm rad}(1+z)^4} \\ &= \frac{-2}{H_0\Omega_{\rm M}}\sqrt{\frac{\Omega_{\rm M}}{1+z} + \Omega_{\rm rad}}\Bigg|_{z_{\rm M}}^{z_*} \equiv \chi_{\rm ML}^{\rm md}(z_{\rm M}), \end{aligned} \tag{5.4}$$

where $\Omega_{\rm rad}$ is the fractional energy density in radiation, including photons and neutrinos. The corresponding expression in Knox (2006) also neglected

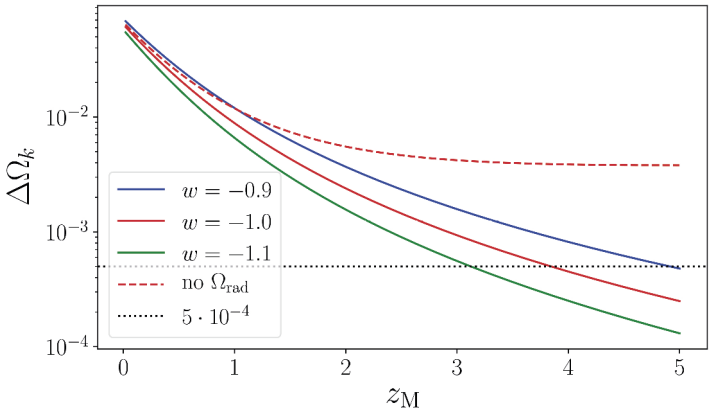

FIGURE 5.3: Bias on the recovered value of $\Omega_{\rm K}$ using the avoidance method, as a function of minimum redshift, z_M, for several input values of w. The red dashed line shows the behavior of the original method from Knox (2006), which neglected radiation, for $w = -1.0$. The dotted line shows roughly the level of the 'curvature floor', or minimum observable curvature (Vardanyan et al., 2009; Leonard et al., 2016).

radiation, but this would bias $\Omega_{\rm K}$ at around the 10^{-2} level, as shown in Fig. 5.3. For models close to ΛCDM, the relative difference between $\chi^{\rm md}_{\rm ML}$ and the true $\chi_{\rm ML}$ (including DE and curvature) quickly drops below 10^{-2} for $z_M \gtrsim 1.5$. The bias in $\Omega_{\rm K}$ for a handful of different values of w are also shown in Fig. 5.3. The implication is that curvature measurements made only at higher redshifts are much less sensitive to the detailed DE behavior, although the choice of minimum redshift will depend on the target precision on $\Omega_{\rm K}$. For example, to ensure a bias below $\Delta\Omega_{\rm K} \approx 10^{-2}$ and 10^{-3} for a reasonable spread of w values, one would take $z_M \gtrsim 1.3$ and $\gtrsim 4$ respectively.

5.3.2 Non-parametric dark energy marginalization

As shown above, trying to avoid the DE-dominated regime still results in a mild model dependence, as the choice of z_M and the expected bias in $\Omega_{\rm K}$ both depend on the DE EOS. There is also the issue that a large amount of low-redshift data must be discarded. In this section we consider an alternative

model-independent approach, based on a piecewise constant parametrization of the EOS. For a sufficiently large number of bins, this allows us to closely approximate essentially any arbitrary EOS. Marginalizing over the w values in all bins then produces curvature constraints that are free of any assumptions about the particular form of $w(z)$, at least in principle.

We define a general piecewise EOS by setting $w(z) \equiv w_i$ for $z_i < z < z_{i+1}$, $i = 1 \ldots N_{\rm bins}^{\rm DE}$, and choose a binning that is equally spaced in scale factor in this instance. The fractional dark energy density is then given by

$$\Omega_{\rm DE}(z) = \Omega_{\rm DE,0}\,(1+z)^{3(1+w_\eta)} \prod_{i=2}^{\eta} (1+z_i)^{3(w_{i-1}-w_i)}\,, \tag{5.5}$$

where η is chosen such that $z_\eta \leq z < z_{\eta+1}$ for a given z.

To obtain curvature constraints using this method, we perform a Markov Chain Monte Carlo (MCMC) analysis to simultaneously fit $\Omega_{\rm K}$, all of the $\{w_i\}$, and several other cosmological parameters to simulated HIRAX and cosmic variance-limited data. The errors on these data were obtained using a Fisher matrix-based likelihood that will be described in Sect. 5.4. We also include the Planck constraints on the distance to last scattering, $D_A(z_*)$, to provide a high-redshift anchor point. We use the `emcee` affine-invariant ensemble sampler implemented by Foreman-Mackey et al. (2013) to run the MCMC, and then marginalize over all w_i values (and other cosmological parameters) to obtain the marginal distribution for $\Omega_{\rm K}$.

Fig. 5.4 shows the correlations between $\Omega_{\rm K}$ and the marginalized parameters for an example MCMC run with 10 EOS bins. For a sufficiently large number of bins, the correlation between $\Omega_{\rm K}$ and any individual w_i is relatively mild, but remains non-negligible. The w_i values themselves can be very strongly correlated with one another, however.

5.3.3 Series expansion of dark energy

In order to better compare our results to the literature, we also derive curvature constraints using the common EOS parametrization $w(z) = w_0 + w_a \frac{z}{(1+z)}$, which

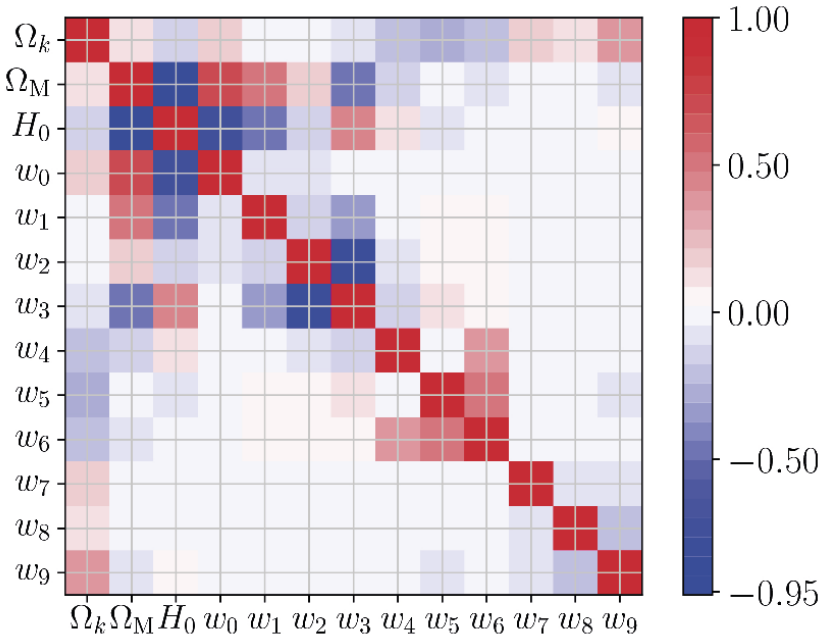

FIGURE 5.4: Parameter correlation matrix for HIRAX, for a piecewise dark energy EOS with 10 bins. The correlation matrix was estimated from the MCMC posteriors.

gives a dark energy density of

$$\Omega_\mathrm{DE}(z) = \Omega_{\mathrm{DE},0}\,\exp\bigl(-3w_a z/(1+z)\bigr)(1+z)^{3(1+w_0+w_a)}. \tag{5.6}$$

This parametrization is quite restrictive in that it cannot reproduce the curvature degeneracy in expansion rate data, and so constraints derived using this model will be model dependent. As in the previous section, we perform an MCMC analysis to find the posterior for Ω_K, marginalizing over all other parameters including w_0 and w_a.

5.4 Forecasts for IM experiments

We now present forecasts for the precision of the model-independent curvature tests that could be performed with forthcoming IM experiments, using HIRAX as an example. To establish the maximum precision of this technique, we also consider two 'futuristic' cosmic variance-limited (i.e. thermal noise-free)

surveys, with the same array configuration as HIRAX, but redshift ranges of $z = 0.3 - 3$ (CV1) and $2 - 5$ (CV2). Such a survey could in principle be accomplished by the future SKA phase 2 (see e.g. Santos et al. 2015). Note that we do not extend CV1 all the way to $z = 0$ as it becomes sensitive only to non-linear scales at low redshifts. For HIRAX we assume the following parameters: frequency resolution, $\delta\nu = 0.4\,\mathrm{MHz}$, total bandwidth $\Delta\nu = 400\,\mathrm{MHz}$, with $\nu_{\mathrm{min}} = 400\,\mathrm{MHz}$ (giving a redshift range of 0.8 to 2.5), system temperature $T_{\mathrm{sys}} = 50\,\mathrm{K}$, the total integration time is assumed to be $t_{\mathrm{int}} = 1\,\mathrm{yr}$ $(2\,\mathrm{yr})$, sky fraction $f_{\mathrm{sky}} = 0.25$ (0.5), dish diameter $D_{\mathrm{dish}} = 6\,\mathrm{m}$ and the number of dishes $N_{\mathrm{dish}} = 1024$. Unless stated otherwise we always refer to HIRAX with $t_{\mathrm{int}} = 1\,\mathrm{yr}$ and $f_{\mathrm{sky}} = 0.25$. The dishes are assumed closely packed, arranged in a square grid with 1 m of space in between. The CV-limited surveys share the same baseline distribution, but cover the redshift ranges from above and have $f_{\mathrm{sky}} = 1$ with no thermal noise.

We begin by assuming that the example surveys will perform measurements of the full anisotropic power spectrum, decomposing it in the radial and transverse directions to obtain constraints on $H(z)$ and $D_A(z)$ respectively. Using the 21cm IM Fisher forecasting code from Bull et al. (2015b) and the specifications of the respective surveys, we obtain covariance matrices for $\{H(z_j), D_A(z_j);\ j = 1...N\}$ in a series of N redshift bins $\{z_j\}$ set by the experiment frequency resolution. We impose a non-linear cutoff scale at $z = 0$ of $k_{\mathrm{NL},0} = 0.2\ \mathrm{Mpc}^{-1}$, which evolves with redshift according to the results from Smith et al. (2003), $k_{\mathrm{MAX}} = k_{\mathrm{NL},0}(1+z)^{2/(2+n_s)}$, where n_s is the spectral index of primordial scalar perturbations. In Section 5.4.2 we examine the dependence of our results on $k_{\mathrm{NL},0}$ and compare to the more conservative choice of $k_{\mathrm{NL},0} = 0.14\ \mathrm{Mpc}^{-1}$.

The form of each covariance matrix is

$$\mathrm{C}(z_j) = \begin{pmatrix} \sigma^2_{D_\mathrm{A}}(z_j) & \sigma_{\mathrm{D_A,H}}(z_j) \\ \sigma_{\mathrm{D_A,H}}(z_j) & \sigma^2_{\mathrm{H}}(z_j) \end{pmatrix}. \tag{5.7}$$

In obtaining these, we have marginalized over redshift-space distortions (i.e. the growth rate and bias in each bin), as well as the non-linear scale σ_{NL}. The measurements are assumed to be uncorrelated between bins and, optimistically,

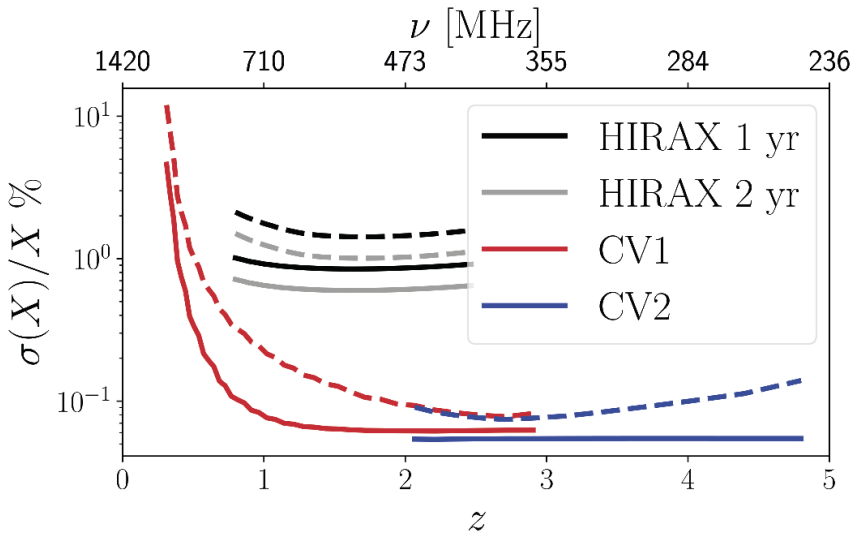

FIGURE 5.5: Forecast fractional errors on H (solid lines) and D_A (dashed lines) for HIRAX and the two CV-limited surveys. We assumed a constant frequency binning with 20 MHz width. The D_A constraints are slightly worse due to (angular) beam smoothing.

we have neglected foreground contamination. Instrumental noise, including a realistic baseline distribution, is included in the Fisher matrix calculation however. The errors on D_A and H are shown in Figure 5.5.

These covariance matrices, plus the fiducial cosmology, provide the input data of the next step, which is to perform an MCMC analysis to extract the curvature, using each of the model-independent methods described above. The cosmological parameters that we sample are $\Theta = \{\Omega_{\rm K}, w_i, \Omega_{\rm M}, H_0\}$, where $i = 1...N_{\rm bins}^{\rm DE}$. For simplicity we set the mock data equal to the fiducial functions: $D_j \equiv D_A(z_j, \Theta_{\rm fid})$ and $H_j \equiv H(z_j, \Theta_{\rm fid})$, where $\Theta_{\rm fid}$ is the fiducial set of cosmological parameters, i.e. we do not add noise to the fiducial data vector.

Using the definitions $\mu_j = (D_j, H_j)$ and $\xi_j = (D_{\rm A}(z_j, \Theta), H(z_j, \Theta))$ and omitting additive constants, we can write the log-likelihood function for the MCMC analysis as

$$\log \mathcal{L} = -\frac{1}{2}\sum_{j=1}^{N}(\xi_j - \mu_j)^{\rm T}{\rm C}^{-1}(z_j)(\xi_j - \mu_j). \tag{5.8}$$

We use only flat priors, with ranges: $w_i \in [-3, 2]$, $\Omega_\mathrm{K} + \Omega_\mathrm{M} \in [0, 1]$, $\Omega_\mathrm{M} \in [0, 1]$, $\Omega_\mathrm{K} \in [-0.5, 0.5]$, $h \in [0.1, 1]$. We also include CMB angular diameter distance data from Planck as additional data points in the MCMC analysis. The standard deviation of the sound horizon at recombination r_*, of the acoustic peak scale Θ_*, and of the mean redshift of the last scattering surface z_* are taken from Planck Collaboration XIII (2016). With $\Theta_* = (r_*/D_{A,*})/(1 + z_*)$, standard error propagation gives $\sigma(D_{A,*}) = 0.044$ Mpc at $z_* = 1090.09$. The contribution of neutrinos and radiation to the mean energy density is assumed to be fixed at $\Omega_\mathrm{rad} = 9.13 \times 10^{-5}$, also from the Planck results.

5.4.1 Convergence of the curvature constraints

The constraints on the cosmological parameters yielded by a given experiment generally depend on the choice of dark energy model. In our case, the constraints depend on the choice of the binning of $w(z)$, and on the number of bins $N_\mathrm{bins}^\mathrm{DE}$. In Figure 5.6, we show the behavior of $\sigma(\Omega_\mathrm{K})$ as a function of $N_\mathrm{bins}^\mathrm{DE}$ for a binning that is equally-spaced in scale factor, a. For a given experiment the curvature constraints converge once the number of bins is large enough, suggesting that the dependence on the particular form of the DE equation of state model has been removed after this point. We find convergence for $N_\mathrm{bins}^\mathrm{DE} \gtrsim 8$ for SDSS, 10 for HIRAX, and 16 for CV1 and CV2.

5.4.2 Results

Table 5.1 lists the 68% errors on Ω_K for different methods of marginalizing out dark energy. While the entries for Planck and SDSS use actual data, we used Fisher forecasts for the planned/hypothetical surveys HIRAX, CV1, and CV2, as described above. The posteriors for HIRAX and CV1 for the $w =$ const. and piecewise constant models are shown in Figure 5.7, where we also compare the full H and D_A constraints to what would be measured using D_A data only.

One can clearly see how much the degeneracy depends on the choice of the dark energy model. While measurements of D_A alone are enough to constrain Ω_K reasonably well for constant $w(z) \equiv w$, this is not the case for

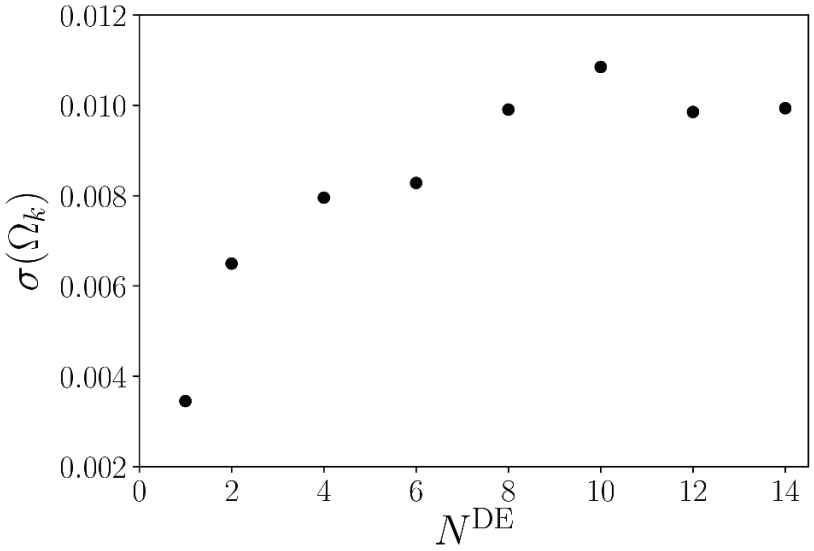

FIGURE 5.6: Forecast 1σ constraints on curvature for HIRAX as a function of the number of DE equation of state bins that are marginalized over, $N^{\rm DE}_{\rm bins}$. The constraints converge for $N^{\rm DE}_{\rm bins} \gtrsim 8$.

the much more general piecewise constant model, which requires $H(z)$ measurements as well to reach an appreciable level of precision. Even for a model with an arbitrarily large number of EOS bins, though, combining $H(z)$ and $D_A(z)$ breaks the curvature-dark energy degeneracy and allows for constraints as good as $\sigma(\Omega_{\rm K}) \approx 2 \times 10^{-3}$ for the cosmic variance-limited surveys. The 2 yr survey for HIRAX is a factor of $\sqrt{2}$ better than 1 yr in the avoidance analysis. When the other methods are used the improvement is somewhat weaker, tightening the constraints by about 30% in the piecewise DE model. CV1 slightly outperforms the higher redshift CV2, even though it covers higher redshifts that are less sensitive to dark energy. This is due to the array setup we assumed being designed for BAO detection in the lower redshift range, so its resolution is worse at higher redshift.

The avoidance method, on the other hand, can yield constraints at the $\sim 10^{-4}$ level in the cosmic variance-limited case, with error-bars a factor of a few smaller than the piecewise constant model for HIRAX. This improvement in precision must be balanced against the potential bias that is introduced by simply ignoring dark energy, as illustrated in Fig. 5.3. Making the expected

	Avoidance	$w \equiv$ const	$w_0 w_a$	Piecewise
Planck	—	-52^{+49}_{-55}	—	—
SDSS	—	$+39^{+29}_{-70}$	—	$+76^{+65}_{-50}$
HIRAX 1 yr	$0.0^{+2.0}_{-2.0}$	$-2.0^{+3.3}_{-3.6}$	$-1.3^{+6.2}_{-7.0}$	$+9.35^{+13.9}_{-7.76}$
HIRAX 2 yr	$0.0^{+1.4}_{-1.4}$	$-2.0^{+2.8}_{-2.9}$	$-2.0^{+5.3}_{-6.0}$	$7.6^{+10.3}_{-6.6}$
CV1	$0.0^{+0.07}_{-0.07}$	$-0.9^{+1.4}_{-1.4}$	$-0.9^{+1.4}_{-1.4}$	$+0.4^{+1.7}_{-1.7}$
CV2	$0.0^{+0.07}_{-0.07}$	$-1.1^{+1.6}_{-1.6}$	$-1.1^{+1.6}_{-1.6}$	$-0.1^{+2.1}_{-1.9}$

TABLE 5.1: Measured (Planck/SDSS) and forecast (HIRAX/CV) constraints on $\Omega_{\rm K}$ at 68% confidence (in units of 10^{-3}), for different dark energy models and analysis methods. For the piecewise constant model, 10 bins were assumed for HIRAX with both 1 and 2 yr integration, 8 for SDSS, and 16 for CV1 and CV2. Planck CMB distance constraints are included in all of these results. For the avoidance approach, a cutoff of $z_M = 2$ was imposed; the expected bias $\Delta\Omega_{\rm K}$ was not included in the errors, but is large (see Fig. 5.8).

bias smaller than the error-bars will require either the reintroduction of a (possibly much simpler) dark energy model, or a higher redshift cutoff z_M. The effect of changing the cutoff is shown in Fig. 5.8; we see that $z_M \gtrsim 2$ is sufficient for the HIRAX measurement to not be dominated by the bias for $w = -1$, while $z_M \gtrsim 4.5$ is needed for CV2.

Note that all of these results can depend on the choice of nonlinear cutoff scale, $k_{\rm MAX}$. If a more conservative value of $k_{\rm NL,0} = 0.14$ Mpc^{-1} is chosen, we find $\Omega_{\rm K} = (9.6^{+14.1}_{-7.5}) \times 10^{-3}$ (68% CL) for HIRAX with the piecewise DE model. This is consistent with the results for the more optimistic choice of $k_{\rm NL,0} = 0.2$ Mpc^{-1} that was used throughout this work.

5.5 Conclusions

In this work, we showed what constraints can be achieved on the curvature when assuming a completely generic dark energy model. We started by Fisher forecasting errors on D_A and H for HIRAX and two cosmic variance-limited surveys, then derived curvature constraints in two different ways that were designed to largely avoid any dependence on the chosen dark energy model.

In the first approach, an extension of the one presented in Knox (2006), we made the assumption that dark energy could be neglected above some $z > z_M$, far into the matter-dominated regime. This largely removes the dependence of the curvature constraints on the DE EOS, at the cost of throwing away information at lower redshift. It is able to produce quite tight constraints on $\Omega_{\rm K}$ however, and while the method is biased, this can be reduced with an appropriate choice of z_M. For a target precision of $\sigma(\Omega_{\rm K}) \sim 10^{-4}$, a redshift cut of $z_M \gtrsim 4$ or more would be necessary.

In the second approach, we adopted a piecewise constant parametrization of the dark energy EOS $w(z)$ and used an MCMC method to sample from the posterior of $\Omega_{\rm K}$, marginalized over the values of $w(z)$ in each bin. This does not require any low-z information to be discarded, is unbiased in principle, and requires fewer assumptions than the first method. The constraints obtained depend on the choice of binning, especially on the number of bins $N_{\rm bins}^{\rm DE}$, but converge once $N_{\rm bins}^{\rm DE}$ is high enough (~ 10 for HIRAX). Generally, this method produces constraints that are an order of magnitude weaker than the avoidance method, but this is reduced to only a factor of $2-3$ when the bias of the latter is factored in.

In conclusion, neither the avoidance nor non-parametric marginalization method is able to reach the target precision of $\sigma(\Omega_{\rm K}) \sim 10^{-4}$ set by eternal inflation models, at least with the instrumental setup we assumed. Confirming the results from Leonard et al. (2016), we conclude that future constraints of that level would likely require strong assumptions on, or knowledge of, dark energy. A possible exception is if the avoidance method is used at very high redshift, $z_M \gtrsim 5$, where the bias should be significantly reduced.

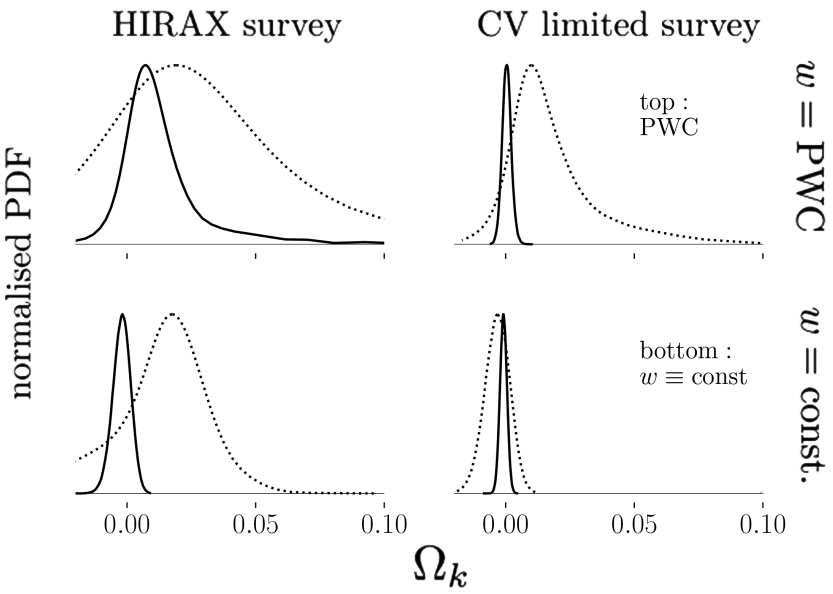

FIGURE 5.7: The (rescaled) posterior distributions of Ω_K for HIRAX (left) and CV1 (right). The bottom row is for a dark energy model with constant w, and the top row is for a model with 10 bins (HIRAX) and 16 bins (CV1) in the piecewise constant parametrization of the EOS. Solid lines correspond to the full analysis, while the dotted lines use D_A measurements only.

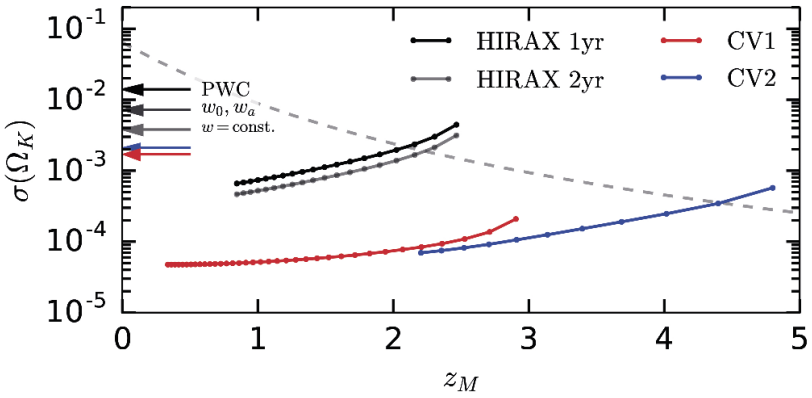

FIGURE 5.8: Constraints on Ω_K as a function of cutoff redshift, z_M, for the avoidance method. The dashed gray line shows $\Delta\Omega_K$ in a $w = -1$ model (c.f. Fig. 5.3). The horizontal bars mark the 68% CL limits for HIRAX for all of the other methods (black/gray), and for just the PWC method for CV1 and CV2 (red/blue).

6 Simulated multi-tracer analyses with HI intensity mapping

This work was published in the journal Monthly Notices of the Royal Astronomical Society (MNRAS) (Witzemann et al., 2019b) and also made available online on the arXiv with number 1808.03093. I lead this project, and was in charge of all results, data analysis, simulations and figures, as well as the majority of text. Collaborator M. Santos provided guidance, editorial work and defined the scope of this project. J. Fonseca contributed parts of the introduction and advice. D. Alonso assisted the use of his code for running simulations, foreground cleaning and calculating masked power spectra. He also suggested the structure and presentation of the work, provided derivations, text (entire section 6.3, subsections 6.2.1, 6.4.1 and parts of other sections) and editorial work throughout.

In this chapter, we use full sky simulations, including the effects of foreground contamination and removal, to explore multi-tracer synergies between a SKA-like 21cm intensity mapping survey and a LSST-like photometric galaxy redshift survey. In particular, we study ratios of auto- and cross-correlations between the two tracers as estimators of the ratio of their biases, a quantity that should benefit considerably from the cosmic variance cancellation of the multi-tracer approach. We show how well we should be able to measure the bias ratio on very large scales (down to $\ell \sim 3$), which is crucial to measure primordial non-Gaussianity and general relativistic effects on large scale structure. We find that, in the absence of foregrounds but with realistic noise levels of such surveys, the multi-tracer estimators are able to improve on the sensitivity of a cosmic-variance

contaminated measurement by a factor of $2-4$. When foregrounds are included, estimators using the 21cm auto-correlation become biased. However, we show that cross-correlation estimators are immune to this effect and do not incur any significant penalty in terms of sensitivity from discarding the auto-correlation data. However, the loss of long-wavelength radial modes, caused by foreground removal in combination with the low redshift resolution of photometric surveys, reduces the sensitivity of the multi-tracer estimator. Even so, it is still better than the cosmic variance contaminated scenario, even in the noise free case. Finally we explore various alternative avenues to avoid this problem.

6.1 Introduction

Probing the physics of the primeval universe is one of the main drivers for observational studies of the cosmos. The Gaussianity of the primordial cosmological perturbations remains an open question, answering it will provide great insight into the details of the dynamics of the very early universe. The current state of the art are the Planck bounds derived from the Cosmic Microwave Background (CMB), for local-type primordial non-Gaussianity (PNG) they read $f_{\rm NL} \simeq 0.8 \pm 5.0$ (Planck Collaboration et al., 2016). Furthermore, local PNG introduces a scale dependence in the bias between the Dark Matter (DM) halos and the astrophysical objects used as tracers of the matter distribution (Dalal et al., 2008; Matarrese & Verde, 2008).

This scale dependence becomes relevant on large cosmological (horizon) scales. At the same time, general-relativistic effects become important on such ultra-large scales (past the matter-radiation equality peak), opening the possibility of testing the theory of gravity in this new regime and finding possible hints of deviations to General Relativity (for a comprehensive review on "GR effects" see e.g. Challinor & Lewis (2011); Bonvin & Durrer (2011); Bonvin (2014)). The next generations of Large Scale Structure (LSS) surveys

such as the Square Kilometer Array (SKA)[1], Euclid[2] and the Large Synoptic Survey Telescope (LSST)[3], promise to be able to target such effects by observing ever larger volumes of the universe. Several forecasts show that they will improve on the Planck constraint on PNG (see, e.g. Giannantonio et al., 2012; Camera et al., 2013, 2015; Alonso et al., 2015b; Raccanelli et al., 2016). Despite the improvements, errors on local PNG from single tracers of the matter distribution will still be unable to push $\sigma(f_{\rm NL})$ below 1, which is vital to distinguishing between single-field and multi-field inflation (see, e.g. de Putter et al., 2017).

The crucial limitation on these surveys comes from cosmic variance, which limits measurements on the largest scales. A decade ago Seljak (2009) proposed a statistical method, often referred to as the multi-tracer technique, to overcome cosmic variance (see also McDonald & Seljak 2009; Hamaus et al. 2011; Abramo & Leonard 2013). The basic idea is that, by comparing two tracers, we can measure the ratio of their biases without requiring to measure the underlying dark matter distribution they trace. This avoids cosmic variance, caused by the stochasticity in the particular realization of the matter distribution we observe. This possibility also shifts the target set-up of future surveys to probe these large scale effects, since smaller volumes thanks to lower noise (e.g. large integration times or higher number densities) may be preferred over larger volumes that provide sufficient samples of the modes of interest (as long as such smaller volumes include the target scales).

Several authors have extensively used the technique to forecast how combinations of future surveys and different DM tracers will impact on the prospects of measuring $f_{\rm NL}$ as well as other horizon-scale GR effects (Yoo et al., 2012; Ferramacho et al., 2014; Yamauchi et al., 2014; Alonso & Ferreira, 2015; Fonseca et al., 2015; Fonseca et al., 2017; Abramo & Bertacca, 2017; Fonseca et al., 2018; Schmittfull & Seljak, 2018). While some combinations do not break the $\sigma(f_{\rm NL}) < 1$ threshold, others have the potential to provide transformational constraints. Such a technique thus

[1] www.skatelescope.org
[2] www.euclid-ec.org
[3] www.lsst.org

greatly extends the potential to probe the physics of inflation and General Relativity with near-future experiments.

Despite the plethora of works studying the potential and applicability of the multi-tracer technique, little has been done to test and assess the performance of the technique within realistic observational settings for future surveys (although the technique has been employed in some analysis of current data (Blake et al., 2013; Ross et al., 2014; Marín et al., 2016), with an emphasis on redshift-space distortions). Questions on what estimators to use and whether they will be biased by contaminants still remain unanswered. This chapter attempts to examine the potential of the multi-tracer technique in a realistic analysis. We will focus on the combination of an HI intensity mapping (IM) survey carried out by a SKA-like facility (Santos et al., 2015) with a LSST-like photometric galaxy survey (LSST Science Collaboration et al., 2009). This combination is a natural choice since both surveys will observe the largest cosmological volumes in an overlapping region of the sky in both the radio and optical/infra-red regimes. Moreover, such surveys will be affected by different sky systematics.

The detection of the notoriously faint HI 21cm signal is observationally challenging. While the emission of individual sources is only likely to be detectable at comparably low redshifts, a technique called *intensity mapping* promises to probe the HI content of large volumes (Chang et al., 2008; Switzer et al., 2013; Battye et al., 2004). This method removes the constraint of resolving sources, and instead measures the integrated emission of all objects within a wide angular pixel. While trading angular resolution for larger survey volumes, intensity maps of the 21cm emission are also contaminated by several sources of foreground radiation, which are often many orders of magnitude brighter than the cosmological signal. Much research has already been done on this topic (e.g. Di Matteo et al., 2002; Oh & Mack, 2003; Santos et al., 2005; Jelić et al., 2010; Moore et al., 2013; Shaw et al., 2015; Wolz et al., 2014) and the main contributors have been identified as galactic synchrotron emission, free-free emission from galactic and extra-galactic origin and point sources. A discussion of cleaning methods for all of these foreground sources can be found in Alonso et al. (2014). While

the residuals after foreground removal should be small, much of the large-scale radial information is removed from the cosmological signal along with the foregrounds.

On the other hand, optical galaxy surveys will be affected by galactic dust extinction and star contamination, as well as several observational systematics, which can affect the observed clustering on large scales (Ross et al., 2011). Cross-correlations between HI intensity and galaxy number count maps are free of systematic effects relevant for only one of the surveys. This is expected to be the case for most foreground residuals, but there could be non-negligible effects of foreground point sources due to thermal dust, which is discussed in the context of intensity maps of carbon monoxide and ionized carbon fine structure emission in Switzer (2017) and Pullen et al. (2018). Apart from improving the reliability of measurements (e.g. Masui et al., 2013; Pourtsidou et al., 2017), cross-correlations can also be used to constrain HI properties (Pourtsidou et al., 2016) or to calibrate photometric redshift estimates (Schulz, 2010).

We explore the multi-tracer technique in the presence of foregrounds in the HI intensity maps using realistic simulations of the observational process. For this purpose we construct estimators of the bias ratios and assess their performance and error. For simplicity we neglect the presence of PNG on the tracer biases, making the bias ratios scale independent, which is expected to have a negligible impact on the estimator errors. We will focus on IM foregrounds, which are likely to be the main contaminant, and neglect the effects of possible systematics in the optical data. Crucially, we wish to determine how sensitive the cancellation of cosmic variance is to IM foreground cleaning and to the observational specifications of each experiment.

This chapter is organized as follows: in section 6.2 we discuss possible multi-tracer estimators that can be used to extract the bias ratio of the two tracers and in particular focus on estimators that can be free from foreground or systematic contamination. In section 6.3 we describe the simulations done for both experiments (SKA1-MID and LSST) and the foreground cleaning method. In section 6.4 we discuss the results, addressing the performance and

error sources of the estimators and possible biases. In particular, we discuss the limitations of the current approach and show possible avenues to improve on this technique. We conclude in section 6.5.

6.2 Multi-tracer estimators

6.2.1 Signal modeling

Our basic observable is the projected fluctuation of a given tracer of the matter distribution on the sky $\Delta(\hat{\mathbf{n}})$. Under the assumption that, on sufficiently large scales, $\Delta(\hat{\mathbf{n}})$ is linearly related to the matter overdensity $\delta_M(t, \mathbf{x})$, the relation between both quantities can be modeled as:

$$\Delta(\hat{\mathbf{n}}) = \int_0^\infty dz\, b(z)\, \phi(z)\, \delta_M(t(z), \chi(z)\hat{\mathbf{n}}), \tag{6.1}$$

where χ is the comoving radial distance, and $b(z)$ and $\phi(z)$ are the bias and selection functions associated with this tracer. For simplicity we have neglected the contributions from redshift-space distortions, magnification and other relativistic effects (Challinor & Lewis, 2011; Bonvin & Durrer, 2011; Bruni et al., 2012; Jeong et al., 2012; Yoo et al., 2012; Hall et al., 2013; Yoo & Desjacques, 2013). This simplifying approximation should not have any significant impact on the final results presented here, since RSDs are suppressed by the broad redshift kernels used and all other terms are highly sub-dominant (Yoo & Seljak, 2015; Alonso et al., 2015a; Alonso & Ferreira, 2015; Fonseca et al., 2015).

Given two tracers a and b, the angular cross-power spectrum is defined as the two-point function of their harmonic coefficients, and can be related to the matter power spectrum $P(k, z)$ as (Di Dio et al., 2014):

$$C_\ell^{ab} \equiv \langle \Delta^a_{\ell m} \Delta^{b*}_{\ell m} \rangle = \frac{2}{\pi} \int_0^\infty dk\, k^2 W^a_\ell(k) W^b_\ell(k), \tag{6.2}$$

$$W^a_\ell(k) = \int dz\, b_a(z) \phi_a(z) j_\ell(k\chi(z)) \sqrt{P(k, z)}, \tag{6.3}$$

Under Limber's approximation (Limber, 1954; Loverde & Afshordi, 2008), this expression can be simplified to

$$C_\ell^{ab} = \int d\chi \frac{b_a \phi_a \, b_b \phi_b \, H^2(\chi)}{\chi^2} \, P\left(z(\chi), k = \frac{\ell + 1/2}{\chi}\right), \tag{6.4}$$

where H is the expansion rate.

In this analysis we have used two different types of tracers: the overdensity of galaxy number counts, which we will label as Δ^g, and the temperature fluctuations in the 21cm line emission caused by neutral hydrogen (HI), $\Delta^{\rm H}$. In the case of galaxy clustering, we approximate the linear galaxy bias as $b_{\rm g} = 1 + 0.84z$ (LSST Science Collaboration et al., 2009), which is an estimate of the results from (Weinberg et al., 2004). On the other hand, as described in Section 6.3.2, the presence of spectrally smooth radio foregrounds makes it infeasible to measure the average 21cm brightness temperature $\bar{T}_{21}$, and it is therefore completely degenerate with the linear bias function associated with this tracer: $b_{\rm H}(z) = \bar{T}_{21}(z)\, b_{\rm HI}(z)$, where $b_{\rm HI}$ is the linear clustering bias associated with the cosmic overdensity of neutral hydrogen [4]. We model both quantities after Bull et al. (2015b).

Finally, the observed fluctuations Δ^a are inevitably contaminated by noise. In the case of galaxy clustering, this is associated with shot-noise due to the discrete nature of the sources used to reconstruct the true underlying distribution. In this case, the noise power spectrum is simply given by the inverse number density of tracer sources in units of Sr^{-1},

$$N_\ell^{gg} = \frac{1}{\bar{n}}. \tag{6.5}$$

For 21cm, the combination of instrumental noise and beam smoothing, caused by the telescope's finite size, effectively erases all modes below the telescope resolution. For an angular Gaussian beam, the harmonic coefficients of the

[4] Note that although this is the case in our analysis, there do exist ways to extract the average HI brightness temperature, for example using cross-correlations, or HI galaxy surveys (Wolz et al., 2017).

beam, multiplying the signal in harmonic space, can be simply modeled as

$$B_\ell = \exp\left(-\frac{\ell(\ell+1)\theta^2_{\rm FWHM}}{16\log 2}\right), \tag{6.6}$$

where $\theta_{\rm FWHM}$ if the beam full-width at half-maximum (FWHM) at a given frequency. The instrumental noise can then be modeled as an additive Gaussian random field with flat power spectrum. For single-dish observations, this is simply given by (Bull et al., 2015b)

$$N_\ell^{\rm HH} = \frac{T^2_{\rm sys} 4\pi f_{\rm sky}}{N_{\rm dish}\Delta\nu t_{\rm tot}}. \tag{6.7}$$

Here $T_{\rm sys}$ is the system temperature, $f_{\rm sky}$ is the total observed sky fraction, $N_{\rm dish}$ is the number of dishes in the instrument, $t_{\rm tot}$ is the total integration time and $\Delta\nu$ is the frequency bandwidth for the particular sky map under consideration.

It is worth noting that we assume no cross-noise term between galaxies and HI. This is expected to be present if the HI-emitting star-forming galaxies form a significant fraction of the galaxy sample, however we assume this shot-noise contribution to be subdominant. We also neglect any correlated $1/f$-like noise component for intensity mapping. We refer the reader to Harper et al. (2018) for a more detailed discussion of correlated noise in the context of foreground contamination and removal.

6.2.2 The Surveys

Our forecasts focus on the combination of 21cm intensity maps, constructed from the SKA data, with optical observations of the galaxy distribution as could be achieved by LSST. We describe the models used for both data-sets here.

We assume the first phase of SKA (in particular SKA-1 MID (Santos et al., 2015)) to consist of 197 dishes, which will use a total of $t_{\rm tot} = 10.000$ h integration time to produce intensity maps covering $\sim 60\%$ of the sky. We assume a combination of single-dish surveys carried out with band 1 and band 2 receivers, and we use a frequency range of $\nu \in (390, 1300)$ MHz,

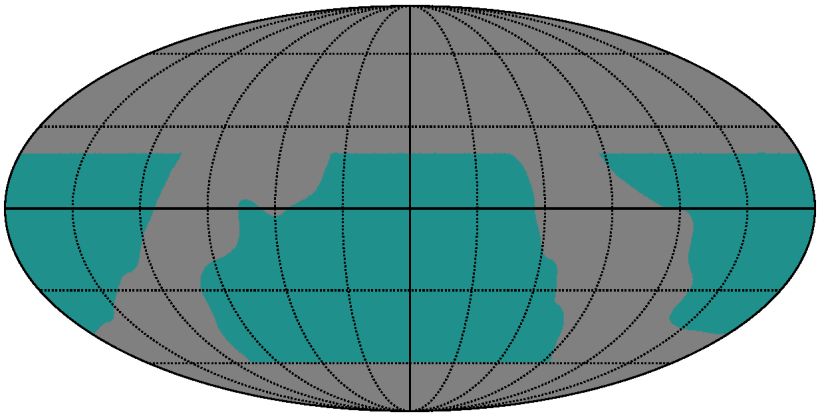

FIGURE 6.1: Sky mask used in our analysis, shown in Mollweide's projection and equatorial coordinates. The masked area is shown in gray. The footprint corresponds to the sky observable from the LSST and SKA with the regions of highest galactic emission (both in synchrotron and dust) removed. The total unmasked area is 16900 deg^2 ($f_{\rm sky} = 0.41$.)

corresponding to a redshift interval $0.1 \leq z \leq 2.65$. Since we work with individual redshift bins at a time, our results are always valid for the receiver type that covers the relevant redshift range. We will assume single-dish observations, which are limited in angular resolution by a beam that we model as Gaussian with a FWHM given by $\theta_{\rm FWHM} = 1.22\,\lambda/D_{\rm dish}$, where λ is the observed wavelength and $D_{\rm dish}$ is the dish diameter. We assume a diameter $D_{\rm dish} = 14.5$m[5], which corresponds to an angular resolution of $\ell \lesssim 90$ in multipoles and a beam full width half maximum (FWHM) of ~ 2 degrees at redshift $z = 1$. Finally, we add white noise as described in the previous section, with a smoothly-varying system temperature $T_{\rm sys}$ following the values given in Square Kilometre Array Cosmology Science Working Group et al. (2018). Further particulars regarding the specific simulated intensity maps used in this analysis are described in Section 6.3.1

For LSST, we use the redshift distribution modeled in Alonso et al.

[5]SKA-1 MID will consist of a combination of 15 and 13.5m dishes, and we use 14.5 as an approximation to the mean dish diameter. This choice should not affect the final results of this study.

(2015a), which yields an integrated number density of 43 galaxies per arcmin^2, in agreement with LSST Science Collaboration et al. (2009). As described in Section 6.3.1, we do not make a precise modeling of the photometric redshift accuracy that LSST will achieve, and instead work with redshift bins wide enough ($\Delta z = 0.1$) to simulate the loss of small radial scales. We do this in order to facilitate the interpretation of the auto-correlation and cross-correlation estimators presented in the next section. A more realistic treatment would either account for the difference in radial window function between the 21cm and optical bins, or re-weight the 21cm frequency channels contributing to each bin to mimic the photo-z window function as closely as possible.

We assume almost complete overlap between SKA and LSST, given their common observable sky. After accounting for contamination from galactic synchrotron (radio) and dust (optical), the final common footprint, displayed in Fig. 6.1, covers 41% of the sky.

6.2.3 The Estimators

Under the assumption that the bias functions vary slowly over the support of the selection functions, and in the limit where the selection functions for both tracers are the same ($\phi^g = \phi^{\rm H} \equiv \phi$), the three different auto and cross-power spectra described in Section 6.2.1 can be written as:

$$\begin{aligned} C_\ell^{gg} &= b_g^2\, C_\ell + N_\ell^{gg}, \\ C^{{\rm H}g} &= b_g \bar{T}_{21} b_{\rm HI}\, B_\ell\, C_\ell, \\ C_\ell^{\rm HH} &= \bar{T}_{21}^2 b_{\rm HI}^2\, B_\ell^2\, C_\ell + N_\ell^{\rm HH}, \end{aligned} \tag{6.8}$$

where C_ℓ is the angular power spectrum of the matter overdensity projected along the line of sight with ϕ. At smaller scales both b_g and $b_{\rm HI}$ are generally thought to be scale dependent and an additional cross-shot-noise term would have to be included in $C^{{\rm H}g}$, (Wolz et al., 2017; Anderson et al., 2018; Villaescusa-Navarro et al., 2018). The focus on large scales motivates our neglect of these effects throughout this work.

On a realization-by-realization basis, the measured values of these quantities will be subject to sample variance, due to the stochastic nature of both the underlying matter fluctuations and the instrumental and shot noise. For signal-dominated modes, the realization-dependent fluctuations will coincide for the three power spectra, and therefore it is possible to constrain certain parameters beyond the limit imposed by sample variance if only a single tracer was available (Seljak, 2009). One obvious example of this is the ratio of the tracer bias functions, which in an ideal noiseless case could be measured exactly by taking ratios of the power spectra above. In this work we will focus on the quantity

$$\epsilon \equiv \frac{b_{\rm HI}\bar{T}_{21}}{b_g}, \tag{6.9}$$

for which we propose two different estimators:

$$\hat{\epsilon}_{{\rm A},\ell} \equiv \sqrt{\frac{\hat{C}_\ell^{\rm HH} - N_\ell^{\rm HH}}{B_\ell^2\left(\hat{C}_\ell^{gg} - N_\ell^{gg}\right)}}, \tag{6.10}$$

$$\hat{\epsilon}_{{\rm X},\ell} \equiv \frac{\hat{C}_\ell^{{\rm H}g}}{B_\ell\left[\hat{C}_\ell^{gg} - N_\ell^{gg}\right]}, \tag{6.11}$$

where all hatted quantities (e.g. $\hat{C}_\ell^{\rm HH}$) are measurements in a given realization. In addition to this, we will also consider a third estimator making use of both the auto and cross-correlation, which combines $\epsilon_{\rm A,\ X}$ in an inverse-variance-weighted manner:

$$\epsilon_{\rm opt} = \frac{\sum_{i,j}\mathsf{C}^{-1}_{ij}\epsilon_j}{\sum_{ij}\mathsf{C}^{-1}_{ij}}, \tag{6.12}$$

where C is the covariance matrix of the two previous estimators computed from simulations.

These three estimators can be understood as different limits of a more general maximum-likelihood estimator combining the three cross-correlations simultaneously, which allow us to explore the impact of foreground contamination in the 21cm maps.

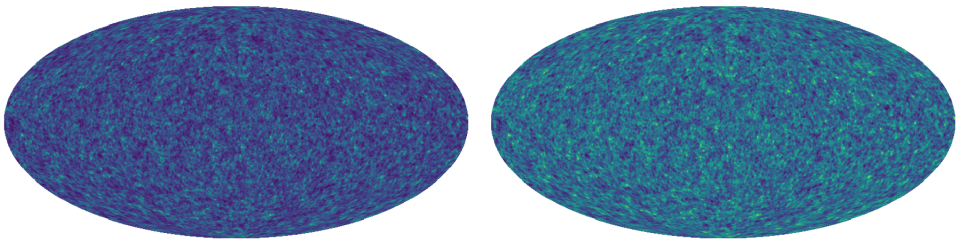

FIGURE 6.2: Galaxy (left) and HI map at 1050 MHz ($z \simeq 0.35$) with a redshift bin width of $\Delta z = 0.1$. We choose a low-redshift bin in order to make the tight correlation between both maps more visually apparent. Both maps trace the same DM background, and show the pure cosmological signal, before inclusion of foregrounds, beam smoothing or noise. Note that the HI maps were generated in much thinner bins of $\Delta\nu = 1$ MHz. Noise, beam and foreground simulation was done in these thin bins, and those maps were later merged to match the thicker bins of the galaxy maps.

6.3 Simulated Forecasts

6.3.1 The Simulations

We produce synthetic signal simulations of both the galaxy distribution and 21cm maps using the publicly available code `CoLoRe`[6]. `CoLoRe` efficiently generates intensity maps for any arbitrary line-emitting species and source catalogs tracing the same dark matter distribution (with their respective biases $b_{\rm HI}(z)$ and $b_{\rm gal}(z)$). `CoLoRe` first generates a Gaussian realization of the linearized density field at $z = 0$ along with the corresponding linear radial velocity field. It then linearly evolves density and velocity to the redshift of each grid point in the simulation and produces a 3D cube of the physical matter density in the lightcone using a log-normal transformation (described in e.g. Coles & Jones (1991))[7] For the galaxy sample the density field is biased and then Poisson-sampled using the galaxy number density $N(z)$. For 21cm, the density field is used to generate a biased HI density, which we then

[6] `https://github.com/damonge/CoLoRe`

[7] Note that `CoLoRe` is also able to produce physical density fields through other more accurate methods (e.g. 1st and 2nd-order Lagrangian perturbation theory, but we chose the log-normal for simplicity and performance reasons). This choice should be irrelevant given that our analysis focuses on relatively large scales.

interpolate into spherical shells that we output as sky maps. For simplicity, we switch off the effect of redshift-space distortions, and therefore the redshift of each source is calculated without accounting for the local velocity field. We simulate a cubic box with 2048^3 Cartesian grid points and a length large enough to encompass the comoving volume to redshift $z = 2.7$. This yields a grid resolution of $\Delta x \simeq 4\,h^{-1}$Mpc. The initial Gaussian density field is smoothed with a Gaussian kernel of size $R_G = 5\,h^{-1}$Mpc to avoid grid artifacts as well as the non-linear distortions induced by the log-normal transformation. This scale is significantly smaller than those we focus on, or than the SKA beam, and therefore the impact of this smoothing on our results is negligible.

We generate 21cm intensity maps with a frequency resolution of $\Delta\nu = 1$ MHz. To each of these maps we first add the simulated foreground maps, smooth them using the SKA Gaussian beam and add the instrumental noise as described above. To study the case of ideal noise-free cosmic-variance cancellation we also simulate equivalent maps of the galaxy overdensity without shot noise. We simulate these as an alternative intensity mapping species with unit mean temperature and a bias given by the galaxy bias. The foregrounds are simulated using `ForGet`, part of the publicly available `CRIME` package[8] (Alonso et al., 2014). We consider 4 unpolarized foreground sources, including galactic synchrotron, galactic and extragalactic free-free emission and extragalactic point sources.

From these outputs we produce maps of the 21cm temperature fluctuations and of the galaxy overdensity on thin radial bins with an equivalent frequency width $\Delta\nu = 1\,$MHz. After the foreground cleaning stage, described in section 6.3.2, the resulting 21cm maps are merged to thicker bins with a width of $\Delta z = 0.1$, and the same is done to estimate the galaxy overdensity in bins of the same width.

Finally, in order to study the statistical properties of our estimators, we generate $N_{\rm sim} = 200$ simulations of the dark matter background, using different seeds for the Gaussian density field. Each simulation is populated with the HI and galaxy distributions, using different seeds for the noise realization and

[8] `https://github.com/damonge/CRIME`

foreground maps. All simulations assume a ΛCDM cosmological model with parameters $(\Omega_M, \Omega_b, n_s, \sigma_8, h) = (0.3, 0.05, 0.96, 0.8, 0.7)$.

Figure 6.2 shows simulated maps of the galaxy overdensity (left) and the HI temperature (right) using this procedure at a redshift $z \simeq 0.35$. Both maps are very strongly correlated, and display similar structures. This tight correlation is the basis for the cosmic-variance cancellation implicit in multi-tracer studies.

6.3.2 Foreground Removal

Foreground removal methods for 21cm intensity mapping (Chapman et al., 2013; Wolz et al., 2014; Shaw et al., 2014, 2015; Alonso et al., 2015a; Zuo et al., 2018) try to separate the cosmological and foreground signals by making use of their different spectral properties: while foregrounds are expected to have a smooth dependence with frequency, which should also be highly correlated across the sky, the cosmological signal follows the large-scale structure, and therefore contains power across a large range of Fourier scales (both in frequency and angles).

Let $\mathbf{d}$ be a vector containing our measurements of the brightness temperature along a fixed line of sight. In general it will contain contributions from foregrounds $\mathbf{f}$, cosmological signal $\mathbf{c}$ and instrument noise $\mathbf{n}$:

$$\mathbf{d} = \mathbf{f} + \mathbf{c} + \mathbf{n} = \mathbf{f} + \mathbf{s}, \tag{6.13}$$

where we have grouped all noise-like components into $\mathbf{s} \equiv \mathbf{c} + \mathbf{n}$. Most foreground removal methods recover an estimate of $\mathbf{s}$ by linearly filtering the data:

$$\mathbf{s}_c = \mathsf{W} \cdot \mathbf{d}, \tag{6.14}$$

using a filter W that minimizes the presence of foreground residuals on $\mathbf{s}$. For instance, principal component analysis (PCA) corresponds to a filter $\mathsf{W} = 1 - \mathbf{U}_{\rm PC}$, where $\mathsf{U}_{\rm PC}$ is the matrix of principal eigenvectors of the data covariance matrix. As another example, a linear fit to a set of smooth functions of frequency, stored in the columns of a matrix A, would correspond to a choice of filter

$$\mathsf{W} = 1 - \mathsf{A}\left(\mathsf{A}^T\mathsf{S}\mathsf{A}\right)^{-1}\mathsf{A}^T\mathsf{S}^{-1}, \tag{6.15}$$

where S is the covariance of $\mathbf{s}$.

After filtering, the cleaned signal

$$\mathbf{s}_c = \mathsf{W}\mathbf{s} + \mathsf{W}\mathbf{f} \tag{6.16}$$

will contain both a version of the original signal where typically the longer-wavelength radial modes have been down-weighted ($\mathsf{W}\mathbf{s}$), as well as foreground residuals ($\mathsf{W}\mathbf{f}$), unless a perfect knowledge of the foreground spectral behavior can be achieved. This has two main consequences when it comes to using s_c for cosmology:

- Unless foregrounds have been perfectly removed (which is never the case), the auto-correlation of the 21cm data will be contaminated by foreground residuals that must be marginalized over (unless we can convince ourselves that their amplitude lies below the noise level at the relevant length scales).

- Even when cross-correlating with other tracers of the large-scale structure, the loss of radial modes implied by the filter W must be taken into account and corrected for in the model for the cross-correlation.

The first effect is inherent to 21cm auto-correlations, and can only be overcome if the residual contamination is sufficiently small, or if a sufficiently accurate foreground model can be built to marginalize over their contribution. However, since we always know the filter W used by the foreground cleaning pipeline, the second effect can be modeled and taken into account. In general, the action of W will be to remove power from the largest radial scales, thus reducing the overall amplitude of any projected clustering statistic. Characterizing this reduction exactly requires a full model of the 3D power spectrum, however we will take a simpler approximate method here, similar to the procedure used in e.g. Masui et al. (2013); Switzer et al. (2013). We model the impact of W on the angular power spectrum as a scale-dependent, multiplicative transfer function $\mathcal{T}_\ell$. I.e.:

$$\tilde{C}_\ell^{\mathrm{HH}} = \mathcal{T}_\ell^2\, C_\ell^{\mathrm{HH}}, \quad \tilde{C}_\ell^{\mathrm{Hg}} = \mathcal{T}_\ell\, C_\ell^{\mathrm{H}g}. \tag{6.17}$$

Here $\tilde{C}_\ell$ and C_ℓ denote power spectra computed after foreground removal and in the absence of foregrounds respectively, and $\tilde{C}_\ell^{\rm HH}$ does not include the contribution from foreground residuals (i.e. it is only the auto-correlation of the first term in Eq. 6.16). We estimate the transfer function from our simulations as:

$$\mathcal{T}_\ell = \frac{\langle C_\ell^{\tilde{\rm H}\rm H}\rangle - N_\ell^{\tilde{\rm H}\rm H}}{\langle C_\ell^{\rm HH}\rangle - N_\ell^{\rm HH}}, \tag{6.18}$$

where $C_\ell^{\rm HH}$ is the auto-correlation of a foreground-free simulation, $C_\ell^{\tilde{\rm H}\rm H}$ is the cross-correlation between a foreground-cleaned and a foreground-free simulation (we have subtracted the noise bias from both power spectra), and $\langle\,\rangle$ denotes averaging over all simulations.

After accounting for this loss of modes, the estimators $\epsilon_{\rm A,\ X}$ in Equations 6.10 and 6.11 above become

$$\epsilon_{{\rm A},\ell} \equiv \sqrt{\frac{\hat{C}_\ell^{\rm HH} - N_\ell^{\rm HH}}{(\mathcal{T}_\ell B_\ell)^2\left(\hat{C}_\ell^{gg} - N_\ell^{gg}\right)}}, \tag{6.19}$$

$$\epsilon_{{\rm X},\ell} \equiv \frac{\hat{C}_\ell^{{\rm H}g}}{\mathcal{T}_\ell\, B_\ell\left[\hat{C}_\ell^{gg} - N_\ell^{gg}\right]}, \tag{6.20}$$

6.4 Results

6.4.1 Theoretical expectation

Before we set off to use our simulations to study the feasibility of multi-tracer methods for intensity mapping, it is instructive to produce a theoretical estimate of the expected performance of our estimators, in order to better understand the simulated results, as well as the main sources of cosmic variance cancellation.

From the expressions for $\epsilon_{\rm A}$ and $\epsilon_{\rm X}$ in Eqs. 6.10 and 6.11, we can write, for one particular realization:

$$\hat{\epsilon}_{{\rm A},\ell} = \epsilon_{{\rm A},\ell}\sqrt{\frac{1+\Delta\hat{C}_\ell^{\rm HH}/(C_\ell^{\rm HH}-N_\ell^{\rm HH})}{1+\Delta\hat{C}_\ell^{gg}/(C_\ell^{\rm gg}-N_\ell^{gg})}}, \tag{6.21}$$

$$\hat{\epsilon}_{{\rm X},\ell} = \epsilon_{{\rm X},\ell}\frac{1+\Delta\hat{C}_\ell^{g{\rm H}}/C_\ell^{g{\rm H}}}{1+\Delta\hat{C}_\ell^{gg}/(C_\ell^{gg}-N_\ell^{gg})}, \tag{6.22}$$

where, as before, all hatted quantities (e.g. $\hat{\epsilon}_{{\rm X},\ell}$) are measurements of the equivalent non-hatted observables in a given realization, and $\Delta\hat{C}_\ell^{XY}$ is the fluctuation around the mean C_ℓ^{XY} in a given realization. Linearizing with respect to these fluctuations, we obtain:

$$\frac{\hat{\epsilon}_{{\rm A},\ell}-\epsilon_{{\rm A},\ell}}{\epsilon_{{\rm A},\ell}} \approx \frac{1}{2}\left(\frac{\Delta\hat{C}_\ell^{\rm HH}}{C_\ell^{\rm HH}-N_\ell^{\rm HH}} - \frac{\Delta\hat{C}_\ell^{gg}}{C_\ell^{gg}-N_\ell^{gg}}\right), \tag{6.23}$$

$$\frac{\hat{\epsilon}_{{\rm X},\ell}-\epsilon_{{\rm X},\ell}}{\epsilon_{{\rm X},\ell}} \approx \frac{\Delta\hat{C}_\ell^{g{\rm H}}}{C_\ell^{g{\rm H}}} - \frac{\Delta\hat{C}_\ell^{gg}}{C_\ell^{gg}-N_\ell^{gg}}. \tag{6.24}$$

To first order, the inverse-squared signal-to-noise ratio can be found by taking the expectation value of the square of the above quantities, obtaining:

$$\left(\frac{S}{N}\right)^{-1}_{{\rm A},\ell} = \frac{1}{2}\left[\frac{{\rm Cov}_\ell^{\rm HH,HH}}{(C_\ell^{\rm HH}-N_\ell^{\rm HH})^2} + \frac{{\rm Cov}_\ell^{gg,gg}}{(C_\ell^{gg}-N_\ell^{gg})^2} - 2\frac{{\rm Cov}_\ell^{\rm HH,}gg}{(C_\ell^{\rm HH}-N_\ell^{\rm HH})(C_\ell^{gg}-N_\ell^{gg})}\right]^{1/2} \tag{6.25}$$

$$\left(\frac{S}{N}\right)^{-1}_{{\rm X},\ell} = \left[\frac{{\rm Cov}_\ell^{g{\rm H},g{\rm H}}}{(C_\ell^{g{\rm H}})^2} + \frac{{\rm Cov}_\ell^{gg,gg}}{(C_\ell^{gg}-N_\ell^{gg})^2} - 2\frac{{\rm Cov}_\ell^{g{\rm H},gg}}{C_\ell^{g{\rm H}}(C_\ell^{gg}-N_\ell^{gg})}\right]^{1/2}, \tag{6.26}$$

where ${\rm Cov}_\ell^{WX,YZ} \equiv \langle\Delta\hat{C}_\ell^{WX}\Delta\hat{C}_\ell^{YZ}\rangle$. For Gaussian fields, a simplified estimate of the covariance matrix (that does not account for e.g. survey geometry) is

(Knox, 1995):

$$\mathrm{Cov}_\ell^{WX,YZ} = \frac{C_\ell^{WY}C_\ell^{XZ} + C_\ell^{WZ}C_\ell^{XY}}{(2\ell+1)f_{\rm sky}\Delta\ell}, \tag{6.27}$$

where $f_{\rm sky}$ is the survey sky fraction and $\Delta\ell$ is the width of the C_ℓ bandpowers used in the analysis.

Substituting this result into the equations above we obtain a final expression for the theoretical signal-to-noise ratio:

$$\left(\frac{S}{N}\right)^{-1}_{{\rm A},\ell} = \frac{1}{\sqrt{2n_\ell}}\left[\frac{(C_\ell^{\rm HH})^2}{(C_\ell^{\rm HH}-N_\ell^{\rm HH})^2} + \frac{(C_\ell^{gg})^2}{(C_\ell^{gg}-N_\ell^{gg})^2} - \frac{2(C_\ell^{g\rm H})^2}{(C_\ell^{\rm HH}-N_\ell^{\rm HH})(C_\ell^{gg}-N_\ell^{gg})}\right]^{1/2}, \tag{6.28}$$

$$\left(\frac{S}{N}\right)^{-1}_{{\rm X},\ell} = \frac{1}{\sqrt{n_\ell}}\left[1 + \frac{C_\ell^{\rm HH}C_\ell^{gg}}{(C_\ell^{g\rm H})^2} - \frac{2C_\ell^{gg}(C_\ell^{gg}-2N_\ell^{gg})}{(C_\ell^{gg}-N_\ell^{gg})^2}\right]^{1/2}, \tag{6.29}$$

where $n_\ell \equiv (2\ell+1)f_{\rm sky}\Delta\ell$ is the number of available modes in a given bandpower.

Inspecting Eqs. 6.28 and 6.29, the idea of cosmic variance cancellation becomes apparent: for perfectly correlated tracers ($C_\ell^{g\rm H} \equiv \sqrt{C_\ell^{\rm HH}C_\ell^{gg}}$), and in the absence of noise ($N_\ell^{gg}, N_\ell^{\rm HH} \to 0$), the negative terms in these equations, originating from the covariance between numerator and denominator in the estimators, exactly cancel the positive terms, and we obtain $(S/N)^{-1} \to 0$. This cosmic variance cancellation would not be possible if the observables entering the estimators were not strongly correlated, as would be the case if, for instance, the 21cm maps and galaxy catalog covered non-overlapping regions of the sky. In this case, $\mathrm{Cov}_\ell^{\rm HH,gg} = 0$, and the signal-to-noise ratio for a cosmic-variance limited version of $\epsilon_{{\rm A},\ell}$ would read:

$$\left(\frac{S}{N}\right)^{-1}_{{\rm CV},\ell} = \frac{1}{\sqrt{2n_\ell}}\left[\frac{(C_\ell^{\rm HH})^2}{(C_\ell^{\rm HH}-N_\ell^{\rm HH})^2} + \frac{(C_\ell^{gg})^2}{(C_\ell^{gg}-N_\ell^{gg})^2}\right]^{1/2}. \tag{6.30}$$

We will make use of these theoretical estimates (Eqs. 6.28, 6.29 and 6.30) in the next section to validate the results of our simulated results in the absence of foregrounds.

6.4.2 Foreground-free results

In order to quantify the full power of the cosmic variance cancellation in the estimators described in Section 6.2.3, we first explore the results from simulations without foregrounds or foreground removal, while including noise, masking and beam smoothing. In this case, all the radial modes are present in the HI data (i.e. the transfer function is $\mathcal{T}_\ell = 1$), and can be used to constrain the bias ratio. The upper panel of Figure 6.3 shows the signal-to-noise ratio of all estimators as a function of multipole ℓ for the redshift bin centered around $z = 0.8$. For concreteness, the quantity plotted is

$$\left(\frac{\mathrm{S}}{\mathrm{N}}\right)_\ell = \frac{\epsilon_\ell^{\rm true}}{\sigma_\ell}, \tag{6.31}$$

where

$$\epsilon_{\mathrm{A},\ell}^{\rm true} \equiv \sqrt{\frac{\langle C_\ell^{\mathrm{HH}}\rangle}{\langle C_\ell^{gg}\rangle}}\Bigg|_{\mathrm{FG-free}}, \quad \epsilon_{\mathrm{X},\ell}^{\rm true} \equiv \frac{\langle C_\ell^{\mathrm{Hg}}\rangle}{\langle C_\ell^{gg}\rangle}\Bigg|_{\mathrm{FG-free}}, \tag{6.32}$$

and

$$\sigma_\ell^2 = \langle \epsilon_\ell^2\rangle - \langle \epsilon_\ell\rangle^2. \tag{6.33}$$

Here, angle brackets denote averaging over all simulations. Note that we define $\epsilon_\ell^{\rm true}$ as the value of the estimator found in foreground-free simulations, and not as the bias ratio given in Eq. 6.9. This is due to the fact that the bias functions and the background 21cm temperature vary slightly within the redshift bin, giving rise to a non-negligible scale dependence of the estimators that would be interpreted as a bias when compared with averages of ϵ over redshift, even for foreground-free simulations. For comparison, the figure also shows results for an additional estimator ϵ_{CV^+}, defined as a version of ϵ_{A} in which the auto-power spectra of 21cm and galaxies are computed from simulations with different seeds. The aim of this estimator is to show the results that would be obtained in the absence of cosmic-variance cancellation (e.g. as would be the case when trying to constrain f_{NL} from a single tracer). Note that we calculate ϵ_{CV^+} in different scenarios, also including instrumental noise, therefore it is not necessarily limited by cosmic-variance.

The signal-to-noise ratio (SNR) of all estimators is shown in the top panel of Figure 6.3, which shows how it should be possible to significantly increase

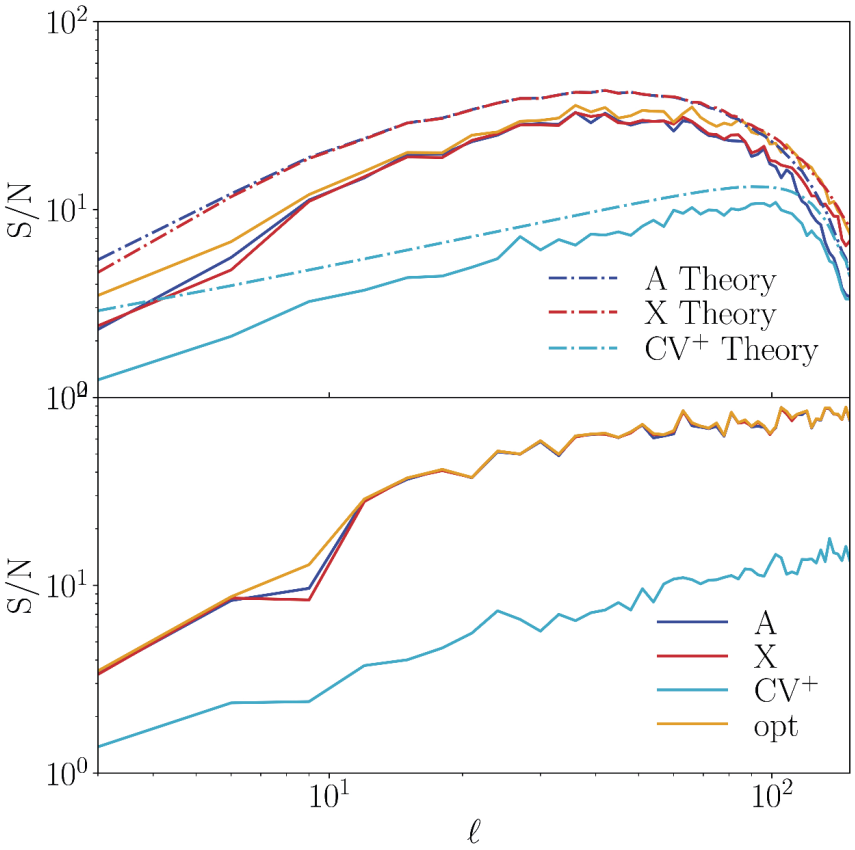

FIGURE 6.3: The signal-to-noise ratio for all estimators in the no foregrounds case (top) and no foregrounds, no noise and no beam case (bottom). Results from the simulations (solid lines) give slightly lower signal-to-noise than the theoretical predictions (dotted-dashed lines) in the upper panel from section 6.4.1. Naturally, $\epsilon_{\rm opt}$ (yellow) has the smallest variance, while $\epsilon_{\rm A}$ and $\epsilon_{\rm X}$ perform similarly (blue and red, respectively). All of them beat the cosmic variance estimator $\epsilon_{\rm CV^+}$ (cyan), in the foreground-free case including noise and beam by a factor of 2-4, and in the noiseless case by a factor of 3-8. It is worth noting that little or no sensitivity is lost by discarding all 21cm auto-correlation information and using only cross-correlations (red vs. orange lines).

the sensitivity within the multipole range $\ell \lesssim 100$ by a factor of up to ~ 4 with respect to the CV-dominated case. This is true for both $\epsilon_{\rm A}$ and $\epsilon_{\rm X}$, which achieve very similar sensitivities. The tight correlation between both estimators implies that the improvement associated with combining both into $\epsilon_{\rm opt}$ is mild, and that very little information is lost by using only cross-correlation information and discarding the 21cm auto-correlations. For comparison, we show the theoretical predictions derived in the previous section as dashed lines. The theory lines follow the same trends as the simulated results, although they predict a SNR that is ~ 1.3 times higher than the simulations, owing to the approximations that go into their derivation. In all cases, no significant cosmic variance cancellation can be achieved beyond the scale of the SKA beam ($\ell \sim 100$), and the overall SNR drops significantly.

The impact of noise on cosmic-variance cancellation can be further explored in a more idealized scenario, by making use of noiseless maps (i.e. simulations containing no 21cm instrumental noise or galaxy shot noise, as described in Section 6.3.1). The results, in terms of S/N, are shown in the lower panel of Fig. 6.3. Even in this idealized situation it is not possible to achieve exact cosmic variance cancellation ($S/N \longrightarrow \infty$), and the relative improvement with respect to the CV-dominated case asymptotes at a factor of $\sim 4-5$. This is caused by two factors: the redshift evolution of the bias functions within the relatively thick redshift bins, and the non-linear lognormal transformation used by `CoLoRe` to guarantee positive-definite density fields. Both effects produce slight differences in the galaxy and HI maps that prevent exact cosmic variance cancellation. We can only expect the impact of both effects to increase in a more realistic situation, in the presence of uncertain and scale-dependent bias relationships. As expected, the absence of noise allows this level of CV cancellation to be sustained beyond $\ell \sim 100$, in comparison with the results described above.

Although the results presented here are encouraging in terms of the large relative improvement with respect to the CV limit, their validity must be verified when foregrounds are included.

6.4.3 Foreground removal

To remove the foregrounds from our simulations, we use the Principal Component Analysis method (PCA), as described in Alonso et al. (2015a). In short, the method is based on de-projecting the principal eigenmodes of the frequency-frequency covariance matrix estimated from the data, under the assumption that those modes are the ones most contaminated by foregrounds. The level of conservativeness in the foreground removal stage can be parametrized by the number of de-projected modes, which we will refer to as the number of foreground degrees of freedom $N_{\rm FG}$.

In order to estimate the number of foreground degrees of freedom that must be de-projected in our simulations, we ran the foreground removal algorithm on all of them for different values of $N_{\rm FG}$. For each value, we use, as a diagnostic for foreground contamination, the relative systematic deviation in the angular power spectrum as a function of frequency and angular scale, defined as

$$\zeta_\ell(\nu) = \left\langle \frac{C_\ell^{\rm clean}(\nu)}{C_\ell^{\rm free}(\nu)} - 1 \right\rangle . \tag{6.34}$$

Here $C_\ell^{\rm free}$ and $C_\ell^{\rm clean}$ are the power spectra for foreground-free simulations and for simulations in which $N_{\rm FG}$ foreground modes have been subtracted respectively. The optimal $N_{\rm FG}$ was then determined as the minimum value that achieves an acceptable degree of foreground removal over a large fraction of the $\ell-\nu$ plane. This quantity is shown in Fig. 6.4 for the cases $N_{\rm FG} = 7$ and $N_{\rm FG} = 9$. Green colors represent a higher power spectrum with respect to the true one, and are a sign of foreground contamination, while purple areas represent lower power spectrum amplitudes and denote a loss of signal-dominated modes caused by over-fitting. As mentioned in Section 6.3.2, the latter effect can be corrected analytically once the foreground removal transformation has been established (e.g. through the transfer function $\mathcal{T}_\ell$), and therefore we seek to minimize foreground contamination. In view of the results shown in this figure, we chose to use $N_{\rm FG} = 9$ as our fiducial value. The transfer function associated with this choice of $N_{\rm FG}$, as defined in Section 6.3.2, is shown in Figure 6.5 for all different redshift bins as a function of scale.

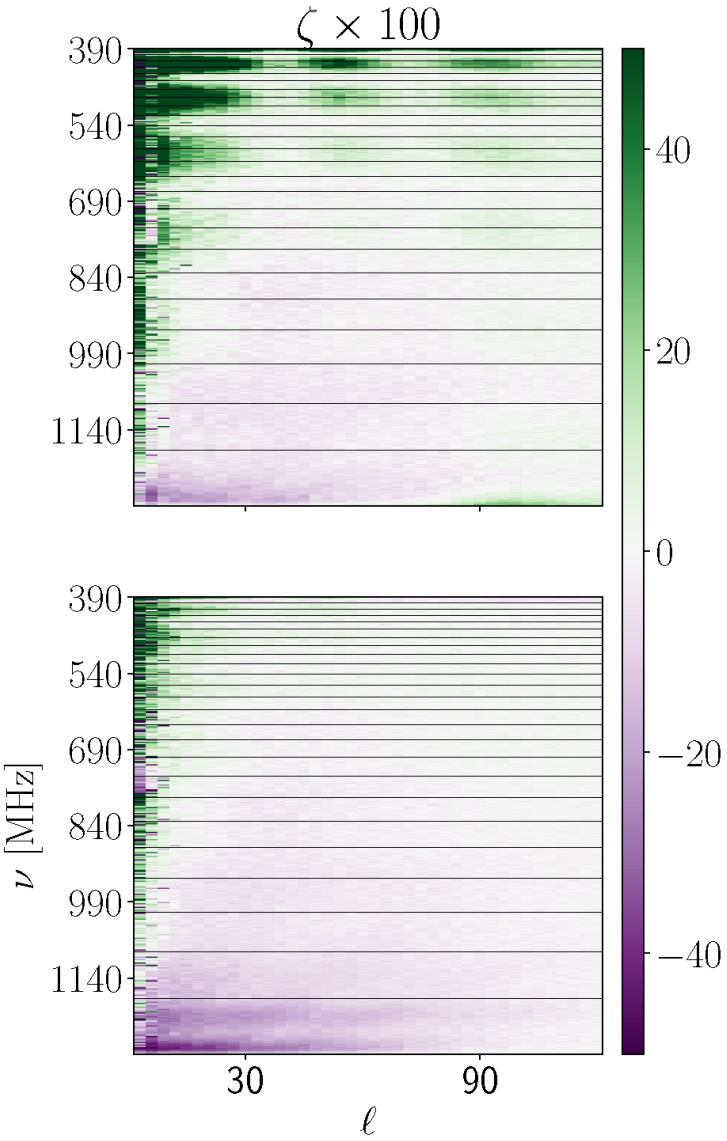

FIGURE 6.4: We demonstrate the effectiveness of foreground cleaning with 7 (top) and 9 degrees of freedom (bottom). The relative difference ζ is defined in Eq. 6.34. For our purposes (measuring large scales), cleaning with 7 degrees of freedom is clearly not sufficient as it leaves visible residuals on scales up to $\ell \lesssim 100$. Therefore the choice of $N_{\rm FG} = 9$ is adopted throughout this work unless otherwise stated. The horizontal lines indicate the frequency binning used in this analysis, corresponding to a fixed width in redshift of $\Delta z = 0.1$.

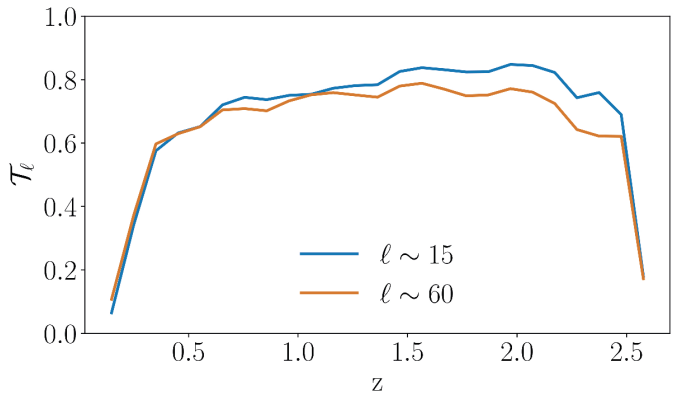

FIGURE 6.5: The foreground removal transfer function $\mathcal{T}_\ell(z)$ for $9 \leq \ell \leq 21$ (blue) and $54 \leq \ell \leq 66$ (orange). The transfer function shows only a mild scale dependence, but drops significantly at the edges of the redshift range, where foreground removal is less efficient (see (Alonso et al., 2015a)).

6.4.4 Results in the presence of foregrounds

As described in Section 6.3.2, the effect of foregrounds is two-fold:

1. Foreground contamination in the auto-correlation will lead to a bias in $\epsilon_{\rm A}$ that can be statistically significant;

2. Foreground removal will erase some of the long-wavelength modes in the signal. This reduces the number of common modes between the foreground-cleaned intensity maps and the galaxy distribution, thereby degrading the performance of the multi-tracer technique.

We first quantify these two effects and then elaborate on their root causes and possible ways around them.

Sensitivity and bias

The impact of the loss of long-wavelength modes in the method's sensitivity can be studied through the signal-to-noise ratio defined in Section 6.4.2. The results are shown in Fig. 6.6 as solid lines for $\epsilon_{\rm A}$, $\epsilon_{\rm X}$ and $\epsilon_{\rm opt}$ as a function of scale for a redshift bin at $z = 1$. The figure also shows the results for the cosmic-variance dominated estimator $\epsilon_{\rm CV^+}$ described in Section 6.4.2 as a solid cyan line. When comparing with the CV limit in the presence of foregrounds

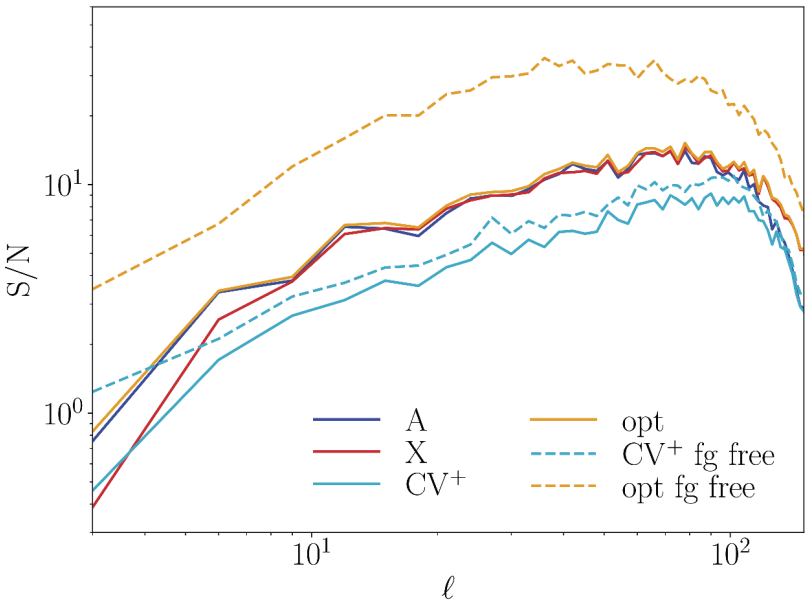

FIGURE 6.6: The signal-to-noise ratio for all estimators in the full analysis plus $\epsilon_{\rm opt}$ and $\epsilon_{\rm CV^+}$ in the foreground-free case, as references. The inclusion of foregrounds in the analysis introduces a significant degradation in sensitivity, and only a slight improvement (a factor ~ 1.5) over the foreground-free cosmic-variance limit (dashed cyan line) is possible.

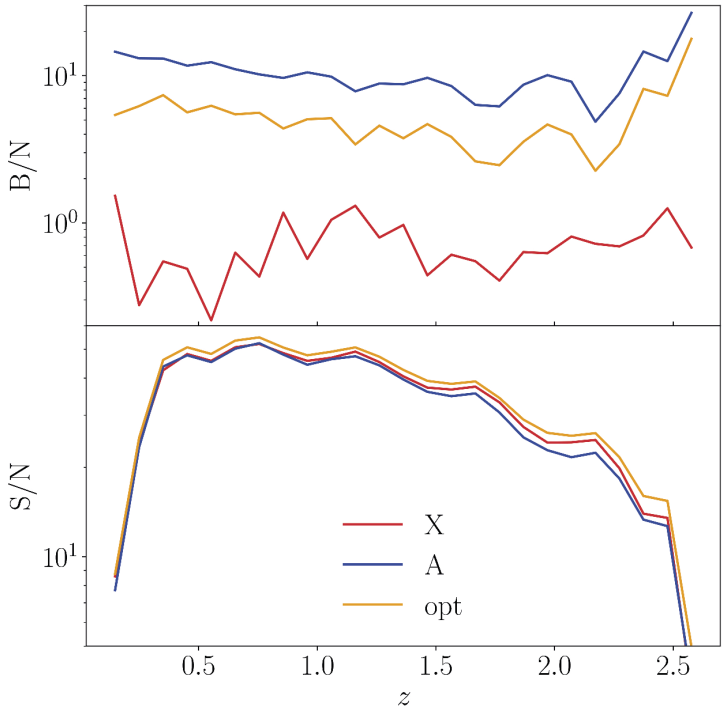

FIGURE 6.7: The signal-to-noise (bottom) and bias-to-noise ratio (top) as a function of redshift, for ϵ_A (blue), ϵ_X (red) and ϵ_{opt} (yellow) in the full analysis. The bias for ϵ_{opt} and ϵ_A increases for low and high redshifts, because foreground cleaning is less effective there (see also figures 6.4 and 6.5). The bias in ϵ_X is compatible with 1σ fluctuations, thanks to lack of foreground residuals in the HI $-$ galaxy cross-correlation. Foreground cleaning still introduces a random error in all estimators, which is highest at the upper and lower ends of the frequency range, similar for all estimators.

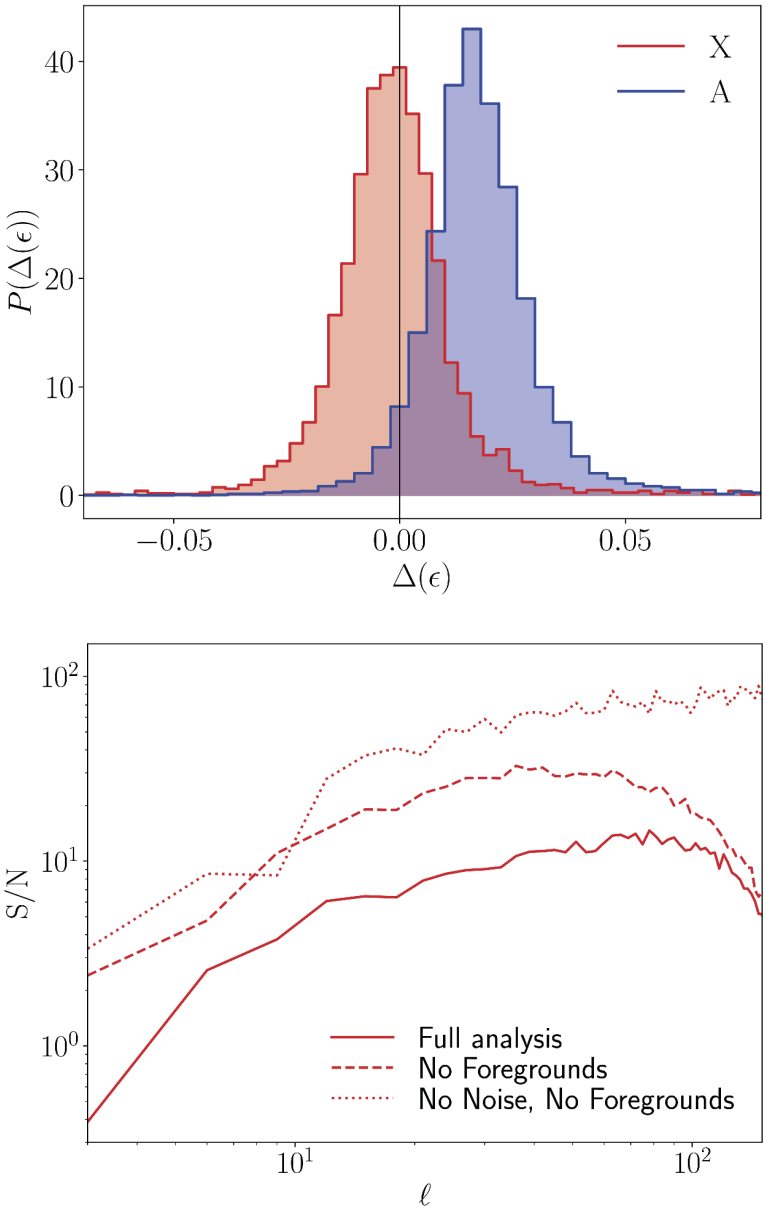

FIGURE 6.8: *Upper panel:* Distribution of $\Delta(\epsilon) = \epsilon - \epsilon^{\text{true}}$ for ϵ_{A} (blue) and ϵ_{X} (red) in the full analysis on the range $0 \leq \ell \leq 81$. The systematic error in ϵ_{A} is due to the effects of foreground cleaning combined with the low radial resolution of the galaxy maps. *Lower panel:* The signal-to-noise ratio of ϵ_{X} for the full analysis (solid line), without foregrounds (dashed line) and without foregrounds or noise (dotted line). At large scales up to $\ell \lesssim 80$ foregrounds are the dominant source of uncertainty for ϵ_{X}.

we observe that all estimators are able to improve upon $\epsilon_{\rm CV^+}$, although now only by a factor of ~ 2. However, when comparing with the full constraining power in the absence of foregrounds, shown as a dashed orange line for $\epsilon_{\rm opt}$ and as a dashed cyan line for $\epsilon_{\rm CV^+}$ in the same figure, we observe a significant loss in S/N and that the impact of foregrounds prevents the estimators from producing a significant improvement in sensitivity with respect to an analysis without CV-cancellation (as would be the case of a single-tracer galaxy survey). We explore this effect in more detail below.

To explore the first effect described at the beginning of this section (the foreground bias), we start by defining the "bias-to-noise" ratio for a given estimator as

$$\left(\frac{B}{N}\right)_\ell \equiv \frac{\langle\epsilon_\ell\rangle - \epsilon_\ell^{\rm true}}{\sigma_\ell}, \tag{6.35}$$

where $\epsilon_\ell^{\rm true}$ and σ_ℓ are defined in Section 6.4.2. We compute this quantity for all redshift bins and multipoles, and then estimate a scale-averaged B/N as a quadrature sum of the ℓ-dependent ratio

$$\left(\frac{B}{N}\right)(z) = \sqrt{\sum_{\ell=0}^{\ell_{\rm max}} \left(\frac{B}{N}\right)_\ell^2 (z)}, \tag{6.36}$$

where the sum is taken over the range of relevant multipoles, depending on redshift. This quantity is shown in the upper panel of Fig. 6.7 as a function of redshift for the three estimators considered here. While the bias of the cross-correlation-based estimator $\epsilon_{\rm X}$ is compatible with $\sim 1\sigma$ fluctuations, the use of auto-correlations through either $\epsilon_{\rm A}$ or $\epsilon_{\rm opt}$ produces noticeable biases of up to 10σ, caused by foreground contamination. The lower panel of the same figure shows the integrated S/N ratio (estimated as a quadrature sum over power spectrum multipoles), and reinforces our conclusion that all estimators achieve similar sensitivities, and therefore we do not incur in any significant loss by dropping all auto-correlation information and using only cross-correlations for which foregrounds do not induce any bias. For the results in both panels of this figure $\ell_{\rm max} = 81$.

Finally, we summarize the main findings of this section in Fig. 6.8. The upper panel shows the distribution of $\epsilon_{\rm A} - \epsilon^{\rm true}$ and $\epsilon_{\rm X} - \epsilon^{\rm true}$ across all

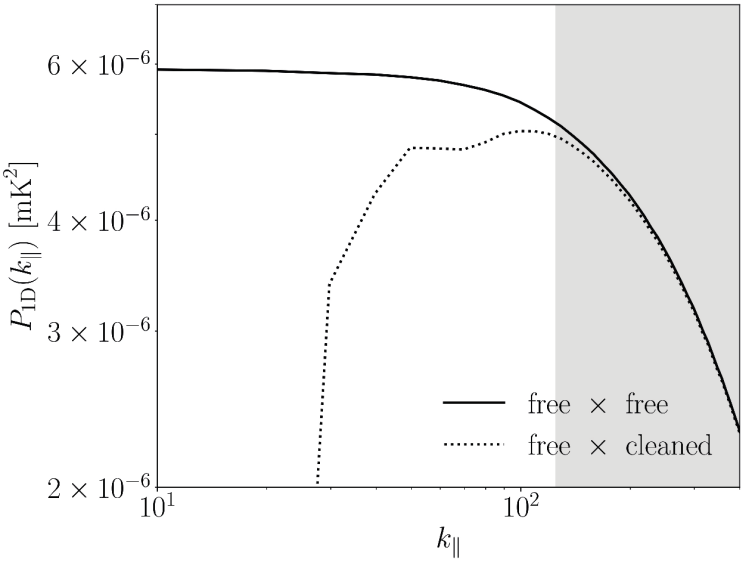

FIGURE 6.9: Radial HI power spectrum, averaged over 200 simulations, showing the auto-correlation of foreground free-maps (solid line) and the cross-correlation of foreground-free and foreground-cleaned maps (dotted line). Note that we use a non-standard dimensionless radial coordinate ν/ν_{21} (see Eq. 6.37), and therefore the wave number $k_\parallel$ is also dimensionless. The loss of long-wavelength radial modes is apparent in the drop of the dotted line for $k_\parallel \lesssim 100$. The gray shaded area indicates the smoothing scale due to the redshift bin width of $\Delta z = 0.1$, associated with the LSST photo-z uncertainty. Unfortunately this is where foreground cleaning works best and the solid and dotted lines agree, limiting the scale overlap between both types of observations.

simulations and ℓ values for a bin at $z \sim 0.8$. The distributions are close to Gaussian, and the ϵ_A shows a clear foreground bias. The lower panel shows the degradation in sensitivity caused by instrumental noise (dotted line to dashed line) and by the partial removal of signal due to foregrounds (dashed line to solid line).

The effects of foregrounds

We have carried out a number of tests to further understand the effects of foregrounds on multi-tracer analyses, and to explore different avenues to

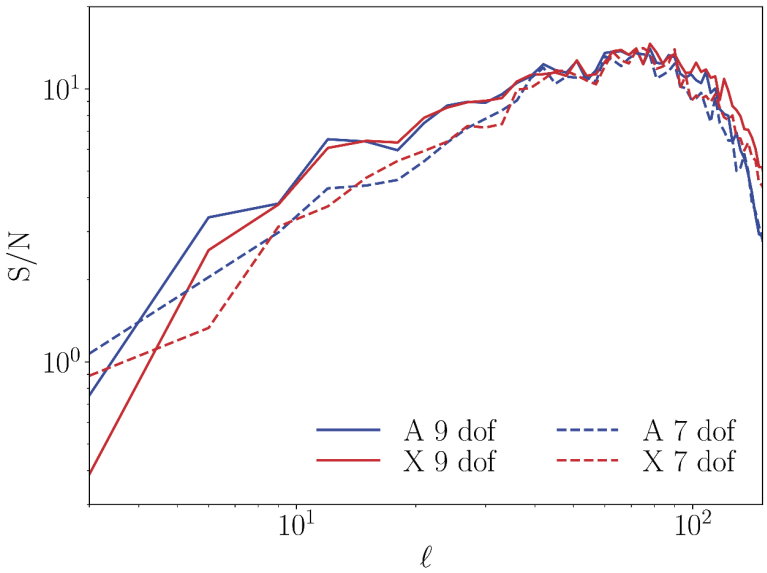

FIGURE 6.10: The signal-to-noise ratio for $\epsilon_{\rm X}$ (red) and $\epsilon_{\rm A}$ (blue) with noise and foregrounds, comparing results obtained from cleaning with 9 (solid lines) and 7 foreground degrees of freedom (dashed lines). The contribution of foreground residuals to the estimator noise outweighs the potential improvement in sensitivity due to the milder subtraction of long-wavelength modes, and the $N_{\rm FG} = 7$ case yields a poorer results than our fiducial choice of $N_{\rm FG} = 9$.

mitigate these effects.

As we have seen, the cross-correlation estimator $\epsilon_{\rm X}$ is immune to foreground bias and its use does not incur in any significant penalty in terms of sensitivity. Therefore, the main impact of foregrounds in 21cm observations is the loss of long radial wavelength modes present in the galaxy distribution. To quantify this effect we have studied the radial 1D power spectrum $P_{\rm 1D}(k_\parallel)$, defined as the variance of the line-of-sight Fourier coefficients of our 21cm maps. In practice we estimate this observable, as outlined in Villaescusa-Navarro et al. (2017), by computing the Fourier transform for a given pixel across all frequencies:

$$\Delta T(k_\parallel, \hat{\mathbf{n}}) = \int \frac{d\nu}{\nu_{21}\sqrt{2\pi}} \exp\left[i\frac{\nu k_\parallel}{\nu_{21}}\right] \Delta T(\nu, \hat{\mathbf{n}}). \tag{6.37}$$

Note that we use ν/ν_{21}, as a radial coordinate, where $\nu_{21} = 1420\,{\rm MHz}$ is the frequency of the 21cm line, and therefore the radial wavenumber $k_\parallel$ is dimensionless[9]. The 1D power spectrum is then computed as the covariance between two fields ΔT_1 and ΔT_2:

$$P_{1D}(k_\parallel) = \frac{\Delta\nu}{\nu_{21}2\pi} \left\langle {\rm Re}\left[\Delta T_1(k_\parallel)\Delta T_2^*(k_\parallel)\right]\right\rangle, \tag{6.38}$$

where the average is taken across all unmasked pixels and all simulations.

Figure 6.9 shows two 1D power spectra, computed from the auto-correlation of the foreground-free simulations (solid line) and from the cross-correlation of the foreground-clean and foreground-free simulations (dotted line). Although both power spectra match on small scales ($k \gtrsim 200$), the loss of long-wavelength radial modes becomes apparent on larger scales, where the amplitude of the cross-correlation becomes significantly smaller than the foreground-free power spectrum. On the other hand, the radial smearing effect of photometric redshifts will erase all structure on scales smaller than the photo-z error σ_z. Since $\nu/\nu_{21} = (1+z)^{-1}$, we can associate σ_z with a threshold wavenumber $k_{\rm ph} \equiv \pi(1+z)^2/\sigma_z$. At $z \sim 1$ and assuming $\sigma_z = 0.03\,(1+z)$, we obtain $k_{\rm ph} \sim 200$, which coincides with the scale at which the mode loss to foregrounds becomes noticeable. The bin width

[9] In practice the Fourier transform is computed as a discrete Fourier transform (Frigo & Johnson, 2005).

$\Delta z = 0.1$ would correspond to a scale $k_{\parallel} \sim 125$, and so effectively all the modes within the shaded region of Fig. 6.9 are erased in the data, due to the top-hat smoothing. The range of radial scales over which a significant overlap between 21cm observations and an LSST-like galaxy sample can be found becomes significantly reduced, which has a negative impact on the cosmic variance cancellation of the estimators studied here.

To circumvent this problem we have explored a few alternative avenues:

- **Foreground degrees of freedom.** To reduce the number of modes lost to foreground removal it is worth exploring the possibility of subtracting a smaller number of degrees of freedom at that stage. As discussed in Section 6.4.3, this will produce significant foreground residuals that will bias the auto-correlation but, since $\epsilon_{\rm X}$ is immune to this bias, its sensitivity might benefit significantly from the presence of additional signal modes. However, although the foreground residuals will not contribute to the bias of $\epsilon_{\rm X}$, they will also provide a contribution to its variance, and therefore there will be a balance between the preservation of long-wavelength modes and the contribution of foreground residuals to the noise.

  Figure 6.10 shows the S/N ratio of $\epsilon_{\rm A}$ (blue) and $\epsilon_{\rm X}$ (red) for the fiducial case, in which $N_{\rm FG} = 9$ foreground degrees are subtracted (solid lines) and for an alternative scenario with $N_{\rm FG} = 7$ (dashed lines). No significant improvement is obtained in both cases, and in fact we observe a reduction in sensitivity on large scales. Therefore, at least for this setup, the contribution of foreground residuals to the estimator variance outweighs the impact of the additional signal degrees of freedom allowed by a more lenient removal stage. More efficient foreground removal methods preserving more information from the signal while at the same time removing all residuals on large scales could potentially improve this result.

- **Thinner redshift bins.** The large photo-z uncertainties that can realistically be achieved by an experiment like LSST will make the use of redshift bins smaller than $\Delta z \sim 0.1$ pointless. This is due to the

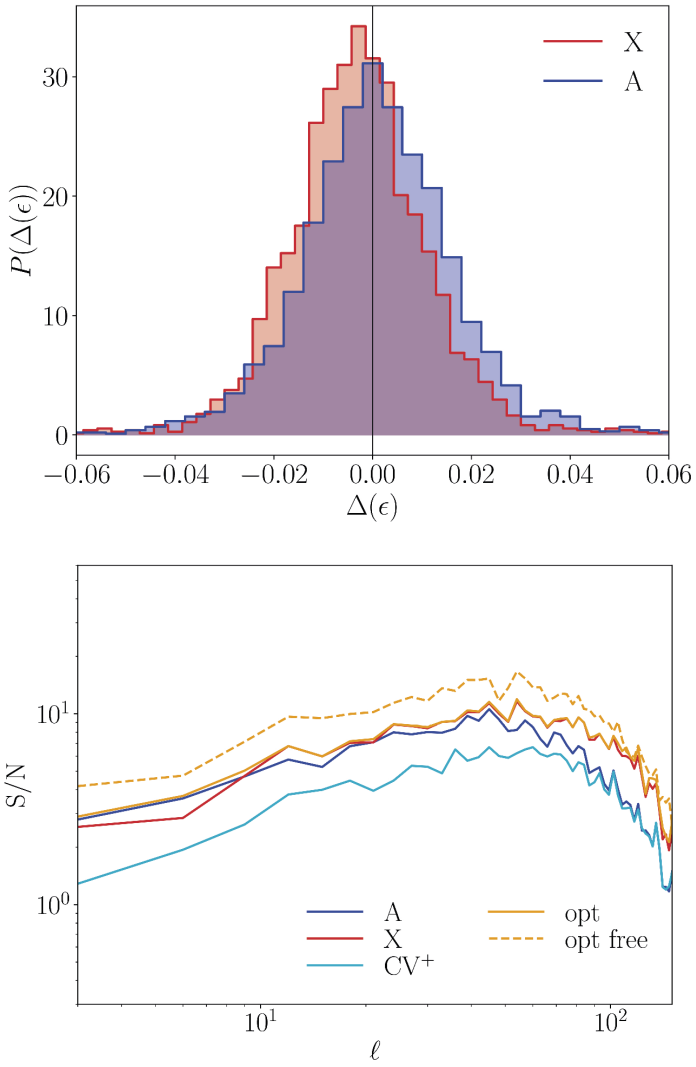

FIGURE 6.11: *Lower panel:* Similarly to fig. 6.6, but working in thin bins of $\Delta\nu = 1$ MHz for both the galaxy and HI maps. We show the signal-to-noise ratio for all estimators in the full analysis, and $\epsilon_{\rm opt}$ in the foreground free case. The latter is worse due to the smaller information content in the much thinner bin, but notably all solid lines actually outperform the respective results obtained from thick bins. This is due to the much bigger overlap of radial modes in the galaxy and HI power spectra when precise galaxy redshifts are assumed. Note that the full constraining power in this case would be realized by combining the information from the much larger number of redshift bins. *Upper panel:* same as fig. 6.8, but also for the thin frequency bin. While the shape and size of the distributions of $\epsilon_{\rm X}$ (red) and $\epsilon_{\rm A}$ (blue) hardly change, the bias in $\epsilon_{\rm A}$ becomes negligible, due to the larger relative number of overlapping radial modes between the 21cm and galaxy data.

strong correlations between narrower bins induced by the photo-z scatter. Nonetheless, it is worth exploring the possible cosmic-variance cancellation gains if a better redshift precision were available. To do so, we have repeated our analysis making use of redshift bins with width $\Delta z = 0.02$.

The results of this exercise are shown in Fig. 6.11 for a bin centered around $z \sim 0.8$. The the lower panel corresponds to the signal-to-noise as a function of scale, and shows an improvement of a factor ~ 2 with respect to the cosmic-variance-limited case for all estimators. Although this is comparable with the results shown for individual bins with $\Delta z = 0.1$, the number of uncorrelated bins available in this case is 5 times larger, and therefore the total signal-to-noise increases significantly. The upper panel of the same figure shows the distributions of $\epsilon_{\rm A}$ and $\epsilon_{\rm X}$ for the same redshift bin across all simulations and values of ℓ. The significant bias in $\epsilon_{\rm A}$ observed in Fig. 6.8 is now gone, owing to the relative increase in radial modes on which the 21cm signal dominates over foreground residuals.

As we emphasized above, although higher redshift resolution improves the performance of multi-tracer methods for 21cm intensity mapping, photometric redshift surveys are unlikely to achieve the required redshift accuracy. On the other hand, although spectroscopic surveys can easily reach that level of radial resolution, they can only do so for a substantially smaller number of objects, and the larger shot noise will inevitably affect the performance of the multi-tracer technique. The most promising option is perhaps intensity mapping of other emission lines (e.g. the CO line (Padmanabhan, 2018)), as long as the instrumental noise can be reduced sufficiently.

- **Matching scales.** Finally, another possibility would be to subject the galaxy overdensity data to the same linear transformation that down-weights the long wavelength modes in the 21cm maps. If this can be done with sufficient accuracy, the resulting auto and cross-power spectra should manifest the same fluctuations around the mean on a

realization-by-realization basis, and a higher degree of CV cancellation could be expected from the estimators used here, based on ratios of those quantities.

Note that in a more optimal analysis, where the full data from the 21cm maps and the galaxy overdensity are used, including all the signal-dominated radial and angular modes (instead of just the power spectrum ratios of matching redshift bins), this is unlikely to provide any advantage over preserving all of the modes in the latter probe. A likelihood evaluation of the full data would automatically produce the cancellation of cosmic variance on all common modes, and would use the additional galaxy long-wavelength modes to increase the final constraints further.

Thus, to summarize: although multi-tracer methods applied to 21cm data in cross-correlation with photometric redshift surveys do improve the constraining power beyond the cosmic variance limit, this improvement is strongly hampered by the loss of long-wavelength modes, common to both data-sets, due to the presence of foreground contamination and low z resolution. Multi-tracer analyses using 21cm observations are therefore more likely to achieve a better performance when combined with other intensity mapping data or spectroscopic surveys, assuming the noise amplitude of the latter (instrumental or shot-noise) can be reduced sufficiently.

6.5 Discussion

21cm intensity mapping and photometric redshift surveys are two promising techniques to study the three-dimensional distribution of matter in the universe on large scales. A number of cosmological observables, such as the level of primordial non-Gaussianity, benefit from the combined analysis of multiple proxies of the same density inhomogeneities in what is known as the "multi-tracer" technique. In this chapter we have explored the feasibility of multi-tracer analyses that exploit the combination of the two aforementioned probes, for the particular case of 21cm observations to be carried out by an SKA-like instrument and an LSST-like galaxy sample. For concreteness, we have

Case	$\epsilon_{\rm A}$	$\epsilon_{\rm X}$	$\epsilon_{\rm CV^+}$	$\epsilon_{\rm opt}$
No noise, no FG	1291	1292	192	1306
No FG	495	502	154	509
No noise	299	298	155	312
Full analysis	178	183	120	192

TABLE 6.1: Signal-to-noise from combining all redshift bins for all estimators and all modeling scenarios of this work. Here using 9 degrees of freedom for the foreground cleaning and a redshift bin width of $\Delta z = 0.1$. While $\epsilon_{\rm A}$ uses the HI and galaxy auto-correlations, $\epsilon_{\rm X}$ uses the HI-g cross-correlation and g-g auto-correlation and $\epsilon_{\rm opt}$ is the inverse variance-weighted sum of both (eqs. 6.10 - 6.12). The estimator $\epsilon_{\rm CV^+}$ on the other hand uses auto-correlations with different DM realizations for the galaxy and HI populations and shows the constraints achievable in the absence of multi-tracer cosmic variance cancellation.

focused our analysis on two estimators of the bias ratio for both samples, $\epsilon_{\rm A}$ and $\epsilon_{\rm X}$, described in Section 6.2.3. Since these estimators make use of the 21cm auto-correlation and its cross-correlation with galaxies respectively, they allow us to explore both the bias induced on $\epsilon_{\rm A}$ by the presence of foreground residuals, and the potential loss of information associated with dropping auto-correlation information ($\epsilon_{\rm X}$). For completeness, we also consider an optimal inverse-variance combination of both estimators, $\epsilon_{\rm opt}$, that uses all the data available.

In the absence of foregrounds, we show that both $\epsilon_{\rm A}$ and $\epsilon_{\rm X}$ are able to achieve similar sensitivities, with little improvement when using $\epsilon_{\rm opt}$ due to the tight correlation between both estimators. When compared with the cosmic-variance contaminated measurement of the same bias ratio, we show that these estimators are able to improve the signal-to-noise by a factor of $\sim$ 4-5, even when compared to the cosmic-variance-contaminated, noise-free case, showcasing the tremendous potential gains of the multi-tracer technique.

The impact of the presence of foregrounds in the 21cm data is twofold. On the one hand, residuals after foreground removal produce an offset in the HI auto-correlation which biases both $\epsilon_{\rm A}$ and $\epsilon_{\rm X}$ at high significance. We show

however, that $\epsilon_{\rm X}$ is immune to this bias, while preserving the same statistical power as the two other estimators. On the other hand, foreground removal is based on the separation of foregrounds and cosmological signal through their different spectral behavior, effectively down-weighting the radial long-wavelength modes where foregrounds dominate. Since photometric redshifts effectively erase all structure along the line of sight on all but the largest scales, the overlap between SKA and LSST in the $k_\parallel$-$k_\perp$ plane reduces significantly, partially spoiling the cosmic variance cancellation. We show that, in this case, the sensitivity of all estimators drops by more than a factor of ~ 2, and that the improvement in signal-to-noise ratio with respect to a cosmic-variance-limited measurement made in the same circumstances is now only a factor ~ 2. This drops to a smaller $\sim 50\%$ improvement when we compare either estimator with the cosmic-variance-limited measurement without foregrounds. These results are summarized in Table 6.1, which shows the cumulative signal-to-noise (quadrature-summed over all multipoles and redshift bins) for the three estimators as well as the CV limit in different scenarios regarding the presence of noise and foregrounds.

We have also explored two possible ways to overcome this problem. First, a less aggressive foreground removal that leaves a larger fraction of foreground residuals in the maps, would also leave a larger number of long-wavelength modes untouched, increasing the scale overlap between LSST and SKA. In practice, however, we have seen that the contribution of the foreground residuals to the estimator uncertainties in fact decrease the total SNR when a smaller number of foreground degrees of freedom are subtracted. Another way to increase the scale overlap between both experiments would be to reduce the size of the redshift bins used in the analysis. Although this is not a real possibility for photometric surveys, since structures can never be resolved on scales smaller than the photo-z uncertainty, this case allows us to explore other possible synergies with either spectroscopic surveys or intensity mapping observations of other emission lines. Our results show that in this case the gain in sensitivity associated with the multi-tracer technique is likely restored, with the added advantage that the foreground bias is also reduced due to the larger fraction of signal-dominated modes. An analysis pairing HI

intensity maps with a spectroscopic survey would work with maps in thin redshift slices and therefore need to take into account cross-correlations between adjacent redshift bins as well as redshift space distortions. A large area survey would most likely suffer from high shot noise degrading the results, but the potential of a low-volume survey with a large number density of galaxies could be interesting. Another promising way forward for these types of analyses may be the combination of intensity mapping observations for different emission lines, even though two emission line surveys might suffer from foreground residual cross-correlations.

In a follow up work we plan to study these new avenues in more detail, first by considering constraints on $f_{\rm NL}$ directly, and including estimators that can deal naturally with the mismatch in the modes that are removing in different surveys does allowing a more perfect cancellation. We will also consider other foreground cleaning methods that might be less aggressive on cleaning this large scales and new tracers with higher redshift resolution.

2013MNRAS.434.1239B

7 Prospects for cosmic magnification measurements using HI intensity mapping

This project (Witzemann et al., 2019a) was submitted to the journal Monthly Notices of the Royal Astronomical Society (MNRAS) and is available on the arXiv with number 1907.00755. As the leading author, I was in charge of all results, calculations and figures, as well as most text. A. Pourtsidou provided the scientific rationale and guidance, checked results, and also provided text and editorial work. M. Santos edited the text and contributed important suggestions to guide and improve this work.

In this chapter, we investigate the prospects of measuring the cosmic magnification effect by cross-correlating neutral hydrogen intensity mapping (HI IM) maps with background optical galaxies. We forecast the signal-to-noise ratio for HI IM data from SKA1-MID and HIRAX, combined with LSST photometric galaxy samples. We find that, thanks to their different resolutions, SKA1-MID and HIRAX are highly complementary in such an analysis. We predict that SKA1-MID can achieve a detection with a signal-to-noise ratio of ~ 10 on a multipole range of $\ell \lesssim 200$, while HIRAX can reach a signal-to-noise ratio of ~ 30 on $200 < \ell < 2000$. We conclude that measurements of the cosmic magnification signal will be possible on a wide redshift range with foreground HI intensity maps up to $z \lesssim 2$, while optimal results are obtained when $0.6 \lesssim z \lesssim 1.3$.

7.1 Introduction

Traveling through the Universe, the path of light is deflected by the mass distribution it encounters. Images of distant light sources are distorted by the intervening matter along the line of sight (LOS), an effect well described by General Relativity. As a result, distortions of shapes, magnifications and even duplicate images are observed and are generally classified as weak or strong gravitational lensing.

Weak gravitational lensing or cosmic shear is a coherent distortion of the shapes of galaxies, and has been routinely detected using optical galaxy surveys, with the first detections reported almost two decades ago (see, for example, Bacon et al. (2000); Kaiser et al. (2000); van Waerbeke et al. (2000); Wittman et al. (2000)). Ongoing and forthcoming large scale structure surveys like CFHTLens (Heymans et al., 2012), DES (Abbott et al., 2016), Euclid (Amendola et al., 2018), and LSST (Abate et al., 2012), will give precise cosmic shear measurements and use them to constrain the properties of dark energy. The accuracy and robustness of weak lensing measurements depends on the control of various systematic effects such as intrinsic alignments, point spread function, seeing and extinction, as well as photometric redshift calibration (Mandelbaum, 2018). In addition, Stage IV lensing surveys with Euclid and LSST will need accurate theoretical modeling of nonlinear clustering and baryonic effects down to very small scales to achieve their goals. Further improvements will come from the use of galaxy-galaxy lensing cross-correlations (van Uitert et al., 2018).

In addition to the distortion of galaxy shapes, there is another form of lensing, cosmic magnification, which can be measured even when the sizes and shapes of sources are inaccessible. This makes it particularly attractive as it is free from many systematics such as the point spread function and intrinsic alignments (see, for example, Zhang & Pen (2006), which discussed the possibility of using radio galaxy surveys to detect this effect). Magnification occurs when intervening structure between an observer and a source acts to magnify or demagnify the object, i.e. sometimes allowing the observer to see objects otherwise too faint (Bartelmann & Schneider, 2001). However, the apparent observed area can also be increased, which leads to an

apparent decrease in number counts if the total number is conserved. Only slightly altering the observed structures, this effect is notoriously difficult to measure (see e.g. the discussion in Hildebrandt et al. (2009)). Several promising techniques exist, but there have been only a few, and controversial, detections (see discussion and references in Scranton et al. (2005)). The first time this signal was measured with high significance was the 8σ detection achieved in Scranton et al. (2005) using the Sloan Digital Sky Survey and the galaxy-quasar cross-correlation. A more recent analysis with DES galaxies is presented in Garcia-Fernandez et al. (2018).

Measurements of cosmic magnification probe the galaxy halo occupation distribution, dark matter halo ellipticities and the extent of galaxy dust halos (Scranton et al., 2005; Menard et al., 2010) – they are complementary to shear-shear measurements, and they can be used to break parameter degeneracies (Van Waerbeke et al., 2010). Similar to cosmic shear, cosmic magnification provides constraints on the galaxy-matter correlation, but without the requirement of measuring shapes, it suffers from less systematic errors and can be extended to sources at much higher redshifts (Scranton et al., 2005). In addition to probing the matter distribution directly, magnification also plays an important role in *geometrical methods* to measure dark energy parameters independently of the matter power spectrum (Jain & Taylor, 2003; Bernstein & Jain, 2004; Taylor et al., 2007). These methods use galaxy-lensing correlations and therefore depend on estimates of the galaxy density. This is directly affected by magnification, which can therefore introduce systematic errors unless corrected for (Scranton et al., 2005; Hui et al., 2007; Ziour & Hui, 2008; Bonvin & Durrer, 2011).

A straightforward approach to measure magnification uses the angular cross-correlation between foreground and background galaxy counts (see e.g. Hildebrandt et al., 2009), where galaxy-magnification or magnification-magnification cross-correlations would be major contributors to a non-zero signal.

Following a similar line of thought, we propose to use HI intensity maps acting as foreground lenses, magnifying a background distribution of galaxies. A motivation for using HI is that intensity maps have no lensing corrections

at first order due to flux conservation (Hall et al., 2013), which removes magnification-magnification correlations between foreground and background. This potentially decreases the signal, but also helps interpretation by removing additional terms in the signal calculation. In addition, the excellent redshift resolution of the foreground HI maps allows to combine measurements using different slices of the HI distribution. Using HI intensity maps also mitigates the danger of overlapping foreground and background sources, which results to a clustering (not lensing) signal. Furthermore, radio and optical observations are subject to different systematic effects, which are expected to drop out in cross-correlation. In the following, we derive forecasts for a potential detection of the magnification signal, using noise properties for the planned radio telescopes SKA1-MID (Square Kilometre Array Cosmology Science Working Group et al., 2018) and HIRAX (Newburgh et al., 2016b), as well as LSST.

The plan of this chapter is as follows: In section 7.2 we give an introduction to cosmic magnification statistics and introduce the possibility of using HI intensity maps as foreground lenses. In section 7.3 we calculate the instrumental (thermal) noise of SKA1-MID and HIRAX, as well as the shot noise from the LSST sample, and investigate the signal and noise properties for the cosmic magnification measurement. In section 7.4 we optimize the signal-to-noise ratio for our proposed method and derive the cumulative signal-to-noise ratio for SKA1-MID and HIRAX. We summarize our findings and conclude in section 7.5.

7.2 Cosmic magnification statistics

In this section we describe the power spectrum formalism for measuring the cosmic magnification signal from background galaxies. We start with the standard approach, which assumes a galaxy sample as the foreground sample, and then introduce the possibility of using HI intensity maps instead.

7.2.1 Galaxies as the foreground sample

Galaxies are biased tracers of the underlying dark matter distribution, which is thought to contain most of the mass distributed along the LOS to a light source. Magnification will increase the flux from a galaxy, making it appear brighter than it actually is. Therefore galaxies normally too faint to be detected can still be seen if the magnification caused by the matter along the LOS is strong enough. However, the apparent area of a source is also increased, resulting in a decrease of the observed number density of galaxies. We can write (Zhang & Pen, 2006)

$$\delta_{\rm g}^{\rm L} = \delta_{\rm g} + (5s_{\rm g} - 2)\kappa + \mathcal{O}(\kappa^2)\,, \tag{7.1}$$

with $\delta_{\rm g}^{\rm L}$ and $\delta_{\rm g}$ the lensed and unlensed intrinsic galaxy over-densities, respectively, and κ the lensing convergence. For a survey with limiting magnitude $m^\star$ the number count slope $s_{\rm g}$ is given by (Duncan et al., 2014)

$$s_{\rm g} = \frac{d\log_{10} n_{\rm g}(<m^\star)}{dm^\star}\,, \tag{7.2}$$

with the cumulative number of detected galaxies per redshift interval and unit solid angle, $n_{\rm g}$. The cross-correlation of well separated foreground (at position $\theta_{\rm f}$ and redshift $z_{\rm f}$) and background ($\theta_{\rm b}$ and $z_{\rm b}$) galaxy samples is free from the intrinsic galaxy over-density correlation term $\langle\delta_{\rm g}(\theta_{\rm f}, z_{\rm f})\delta_{\rm g}(\theta_{\rm b}, z_{\rm b})\rangle$, therefore

$$\begin{aligned}\langle\delta_{\rm g}^{\rm L}(\theta_{\rm f}, z_{\rm f})\delta_{\rm g}^{\rm L}(\theta_{\rm b}, z_{\rm b})\rangle &= \langle(5s_{\rm g}^{\rm b} - 2)\kappa_{\rm b}\delta_{\rm g}(\theta_{\rm f}, z_{\rm f})\rangle \\ &+ \langle(5s_{\rm g}^{\rm f} - 2)(5s_{\rm g}^{\rm b} - 2)\kappa_{\rm f}\kappa_{\rm b}\rangle\,,\end{aligned} \tag{7.3}$$

where the superscript L denotes lensed quantities. The right hand side of equation 7.3 contains the magnification-galaxy ($\mu - {\rm g}$) correlation (first term) and the magnification-magnification ($\mu - \mu$) correlation (second term). The latter is subdominant for foregrounds at comparably low redshifts and therefore usually neglected. If both foreground and background galaxies are at high redshifts, however, it can become large (Ziour & Hui, 2008).

7.2.2 HI intensity maps as the foreground sample

In this work, we focus on the magnification effect of HI intensity maps in the foreground, acting on the clustering statistics of background galaxies. Intensity maps themselves are not lensed at linear order due to surface brightness conservation (Hall et al., 2013). This means that $s_{\rm HI} = 2/5$ and

$$\delta T_{21}^{\rm L} = \delta T_{21} = \bar{T}_{21}\delta_{\rm HI} = \bar{T}_{21} b_{\rm HI}\delta\,, \tag{7.4}$$

where $\bar{T}_{21}$ is the mean brightness temperature of neutral hydrogen, $b_{\rm HI}$ is the hydrogen bias and δ the dark matter over-density. Considering galaxies as the background sample, we now have

$$\langle \delta_{\rm HI}^{\rm L}(\theta_{\rm f}, z_{\rm f})\delta_{\rm g}^{\rm L}(\theta_b, z_b)\rangle = \langle (5s_{\rm g}^{\rm b} - 2)\kappa_b b_{\rm HI}\delta(\theta_{\rm f}, z_{\rm f})\rangle\,, \tag{7.5}$$

where the magnification-magnification term is absent since $s_{\rm HI} = 2/5$. The above relation holds at all redshifts, given that the foreground and background samples are well separated. This can be guaranteed via the excellent redshift information provided by the intensity mapping survey.

The observable magnification signal can be expressed using the angular power spectrum (Zhang & Pen, 2006; Ziour & Hui, 2008)

$$\begin{aligned} C_\ell^{{\rm HI}-\mu}(z_{\rm f}, z_{\rm b}) = {} & \frac{3}{2}\frac{H_0^2}{c^2}\Omega_{\rm m,0} \times \\ & \int_0^\infty dz \frac{b_{\rm HI}\bar{T}_{21}(z) W(z, z_{\rm f}) g(z, z_{\rm b})}{r^2(z)}(1+z) \times \\ & P_{\rm m}((\ell + 1/2)/r(z), z)\,, \end{aligned} \tag{7.6}$$

where $r(z)$ is the comoving distance to redshift z and we have applied the Limber approximation, valid for $\ell \geq 10$ (Limber, 1954; Loverde & Afshordi, 2008). The redshift distribution of the foreground HI intensity maps is given by a top hat over the foreground redshift bin $W(z, z_{\rm f})$ and $g(z, z_{\rm b})$ is the lensing kernel:

$$g(z, z_{\rm b}) = \frac{r(z)}{N_{\rm g}(z_{\rm b})}\int_{z_{\rm b}^{\rm min}}^{z_{\rm b}^{\rm max}} dz' \frac{r(z') - r(z)}{r(z')}(5s_{\rm g}(z') - 2) n_{\rm g}(z')\,, \tag{7.7}$$

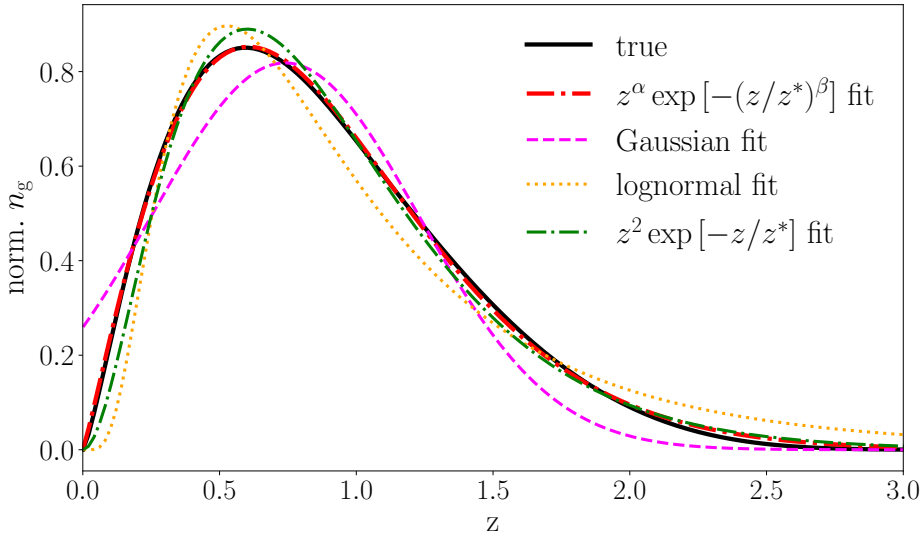

FIGURE 7.1: Different fitting functions for the cumulative galaxy number count were considered. The normalized 'true' function here is taken from Alonso et al. (2015b) (solid black line). The best fitting function (red dotted-dashed line) is given in Equation (7.11).

where the number of galaxies per square degree in the background bin is

$$N_{\rm g}(z_{\rm b}) \equiv \int_{z_{\rm b}^{\rm min}}^{z_{\rm b}^{\rm max}} n_{\rm g}(z) dz \,, \tag{7.8}$$

and $z_{\rm b}^{\rm min}$, $z_{\rm b}^{\rm max}$ denote the minimum and maximum redshift for the background galaxy sample. An interesting feature of the geometrical weight $\frac{r(z')-r(z)}{r(z')}$ is that, in a flat universe, it takes the form of a parabola with a maximum at $r(z') = r/2$. Thus, structures half-way between the source and the observer are the most efficient to generate lensing distortions (Kilbinger, 2015) (and very low redshift foregrounds are less favored).

For increased computational speed, we use a fitting function to approximate the cumulative galaxy count for LSST, $n_{\rm g}$, provided in the publicly available code from Alonso et al. (2015b). This code in turn uses the Schechter function (Schechter, 1976) for the r'-band luminosity from Gabasch et al. (2006), with the faint end slope $\alpha = -1.33$, the characteristic magnitude M^*

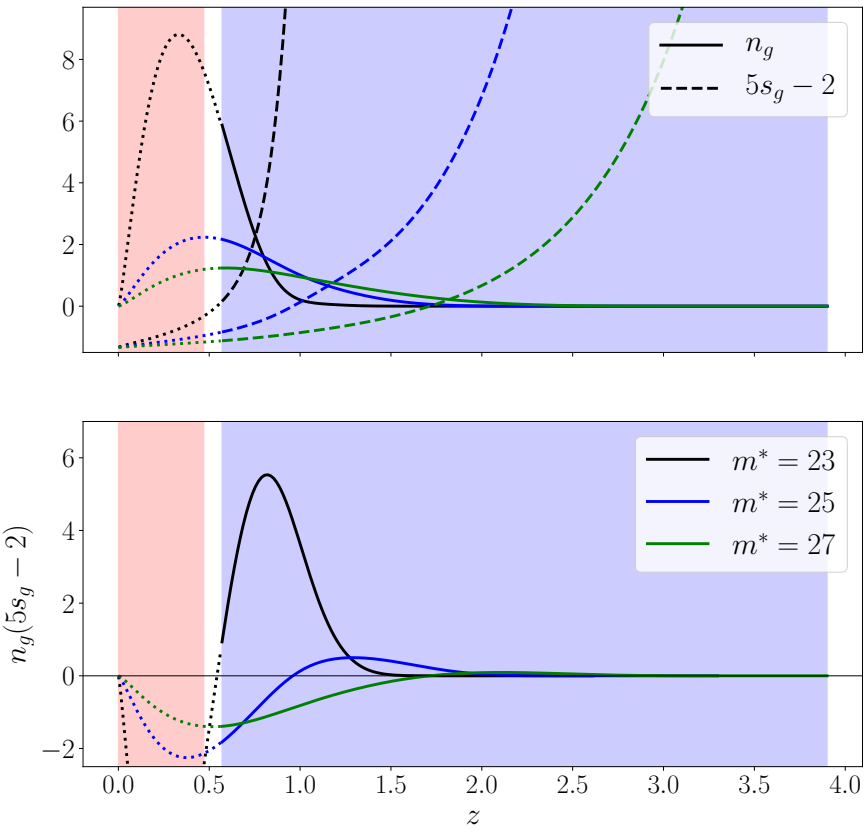

FIGURE 7.2: We illustrate the behavior of the number count slope s_g and galaxy count n_g with respect to the magnitude threshold m^*, here with foreground redshift $0 < z < 0.47$, which corresponds to band 2 of SKA1-MID, described in detail in section 7.3. The red (blue) shaded areas indicate the foreground (background) redshift range. The upper panel displays the galaxy number density n_g (normalized to integrate to one inside the background bin), and the contribution of the number count slope s_g. The bottom panel shows the product $n_g(5s_g - 2)$, which is the only term inside the integral Equation (7.7) to potentially be negative. This demagnification leads to cancellation in the integration and thus to a smaller lensing signal. An appropriate magnitude cutoff enforces $5s_g > 2$ in the background redshift bin and thus boosts the signal. However, this comes at the cost of increasing the galaxy shot noise.

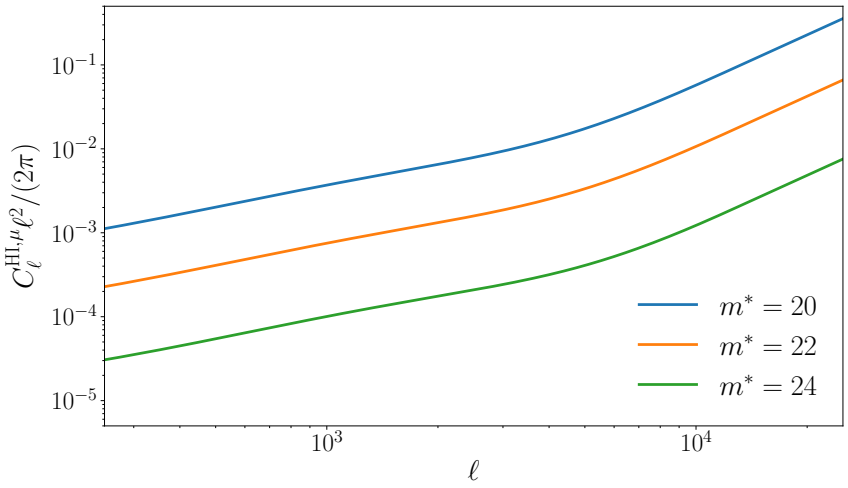

FIGURE 7.3: The HI-magnification cross-correlation power spectrum for a foreground redshift from $z = 0$ to 0.47, corresponding to band 2 of SKA1-MID. Lower magnitude cuts increase the magnification signal.

$$M_*(z) = M_0 + a\ln(1+z) \tag{7.9}$$

and the density ϕ^*

$$\phi_*(z) = (\phi_0 + \phi_1 z + \phi_2 z^2)[10^{-3}\mathrm{Mpc}^{-3}]. \tag{7.10}$$

Here $M_0 = -21.49$, $a = -1.25$, $\phi_0 = 2.59$, $\phi_1 = -0.136$, $\phi_2 = -0.081$. We adapt the fit from LSST Science Collaboration et al. (2009) to approximate n_g as follows,

$$n_\mathrm{g}(z) \propto z^\alpha \exp\left(-\left(\frac{z}{z^*}\right)^\beta\right), \tag{7.11}$$

where we optimize the parameters α, β and z^* to fit n_g from Alonso et al. (2015b) as functions of magnitude cutoff m^* by interpolation. Fig. 7.1 compares this fit with the true n_g and with several other fitting functions. The overall amplitude is irrelevant in Equation (7.7), as n_g is normalized to integrate to one, but it is required to calculate the shot noise – see section 7.3 for details.

The number count slope s_g (Fig. 7.2) rises quicker for a lower magnitude

cutoff, therefore the magnitude threshold can be chosen to avoid a sign change of $5s_{\rm g} - 2$ in the background redshift bin. The amplitude of the magnification signal is proportional to a redshift integral of $5s_g - 2$ (Equations (7.2) and (7.6)). An appropriate magnitude cutoff thus boosts the signal by avoiding cancellations inside the integral for the lensing kernel g. Fig. 7.2 demonstrates this in a situation where a lower magnitude threshold is beneficial to optimize the magnification signal, which is shown in Fig. 7.3. Decreasing m^* comes at the cost of a smaller number of observed galaxies and therefore increased shot noise. We optimize to achieve a maximal signal to noise ratio. We will further discuss this in section 7.3.2, and we also note that a number count slope weighting was suggested in (Menard & Bartelmann, 2002) and used in the SDSS data analysis of Scranton et al. (2005).

We use `CAMB` with `HALOFIT` (Lewis et al., 2000; Smith et al., 2003; Takahashi et al., 2012) to estimate the nonlinear matter power spectrum, $P_{\rm m}(k, z)$, assuming a flat ΛCDM cosmology with $h = 0.678$, $\Omega_c h^2 = 0.119$, $\Omega_b h^2 = 0.022$, $n_{\rm s} = 0.968$.

The error in the measurement of the cross-correlation power spectrum is

$$\Delta C_\ell^{\rm HI-\mu} = \sqrt{\frac{2((C_\ell^{\rm HI-\mu})^2 + (C_\ell^{\rm gg} + C^{\rm shot})(C_\ell^{\rm HI-HI} + N_\ell))}{(2\ell+1)\Delta\ell f_{\rm sky}}}\,, \tag{7.12}$$

where $C^{\rm shot}$ is the galaxy shot noise power spectrum, N_ℓ is the thermal noise of the intensity mapping instrument, $\Delta\ell$ is the binning in multipole space, and $f_{\rm sky}$ is the fraction of sky area overlap of the HI and optical surveys. For the foreground HI IM sample we use a top-hat window function $W(z) = 1/\Delta z$ inside the bin of width Δz and zero elsewhere. We can then write the HI and galaxies auto-correlation power spectra as

$$C_\ell^{\rm HI-HI} = \frac{H_0}{c}\int dz E(z)\left(\frac{b_{\rm HI}\bar{T}_{21}(z)W(z)}{r}\right)^2 P_{\rm m}\left(\frac{\ell+1/2}{r}, z\right), \tag{7.13}$$

and

$$C_\ell^{\rm g-g} = \frac{H_0}{cN_{\rm g}^2}\int dz E(z)\left(\frac{b_{\rm g}(z)n_{\rm g}(z)}{r}\right)^2 P_{\rm m}\left(\frac{\ell+1/2}{r}, z\right), \tag{7.14}$$

where we have written the Hubble rate as $H(z) = H_0 E(z)$, and the HI bias $b_{\rm HI}$ is given by fits to the results from Alonso et al. (2015b):

$$b_{\rm HI}(z) = 0.67 + 0.18z + 0.05z^2 \,. \tag{7.15}$$

The galaxy bias $b_{\rm g}$ naturally depends on redshift as well as magnitude cutoff, as brighter objects are rarer and thus more biased, an effect which is ignored when a simple linear and deterministic fitting function is used, for example

$$\tilde{b}_{\rm g}(z) = 1 + 0.84z. \tag{7.16}$$

To enforce a behavior similar to that of the magnification bias at higher redshifts and more stringent magnitude cuts, we use a piecewise differentiable galaxy bias:

$$b_{\rm g}(z) = \max\left(\tilde{b}_{\rm g}, \frac{1}{2}(5s_{\rm g} - 2)\right). \tag{7.17}$$

This choice makes sure that the ratio $(5s_{\rm g} - 2)/b_{\rm g}$ converges, as described in (Hui et al., 2007), and the resulting ratio is shown in Fig. 7.4 for different magnitude cutoff values. We note that this choice has a comparably weak effect on our results, as the signal remains unaltered and, as it will be shown, errors are mostly shot noise dominated.

The mean observed HI brightness temperature is calculated using the fit provided in Santos et al. (2017), which is based on the results from Santos et al. (2015):

$$\bar{T}_{21} = 0.0559 + 0.2324z - 0.024z^2 \ {\rm mK} \,. \tag{7.18}$$

7.3 Error calculations

7.3.1 HI intensity maps

We consider the experiments HIRAX and SKA1-MID to map the distribution of HI, used as the foreground sample. Together with the shot noise from LSST, their instrumental noise contributes to the total error budget given by Equation (7.12).

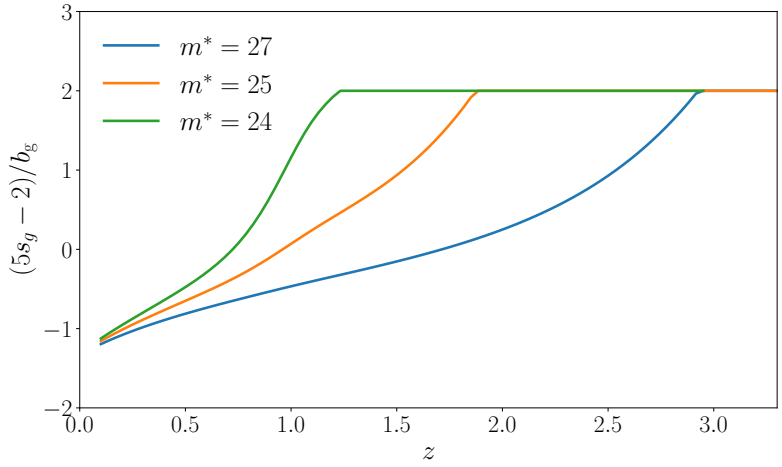

FIGURE 7.4: The ratio of number count slope and galaxy bias $(5s_g - 2)/b_g$ for different magnitude cutoff values. The ratio is set to 2 for higher redshifts via the choice of galaxy bias, see Equation (7.17). The maximum magnitude detectable with LSST is assumed to be 27. Imposing a lower magnitude cutoff increases the shot noise, but also the number count slope, which increases the magnification signal.

HIRAX is a planned radio interferometer of 6 m diameter dishes, sharing the site in the Karoo in South Africa with MeerKAT and SKA1-MID. We assume the full planned array of 1024 and the reduced set of 512 dishes, arranged in a dense square grid with 1 m space between individual antennas. HIRAX aims to perform a large sky intensity mapping survey with $15,000$ deg^2 area, and the integration time is taken to be two full years (corresponding to 4 years observation). We assume a constant system temperature of 50 K on its entire frequency coverage ranging from 400 to 800 MHz (Newburgh et al., 2016b).

At the same time, SKA1 is assumed to have only one year worth of integration time but a larger survey area of 16,900 deg^2. This corresponds to the maximum possible survey overlap with LSST, after taking into account the total survey area of SKA1-MID (Santos et al., 2015) and contamination from galactic synchrotron radiation and dust. SKA1-MID will consist of different dish types: the (already operating) 64 MeerKAT dishes with 13.5 m, and 133 SKA1-MID dishes of 15 m diameter. For simplicity, we assume all

dishes to be identical, taking an average dish diameter $\tilde{D}_{\rm dish} = (64 \times 13.5 + 133 \times 15)/(64 + 133)$ m and using a Gaussian beam pattern. We consider two observational bands: band 1 ranging from 350 to 1050 MHz, and band 2 from 950 to 1750 MHz (Square Kilometre Array Cosmology Science Working Group et al., 2018). The system temperature is assumed to be 30 K for band 1 and 20 K for band 2. This is conservative on low redshifts. For high-redshift foreground bins, the system temperature increases beyond that, but at the same time the galaxy shot noise becomes the dominant source of error and magnification detections quickly become extremely difficult for foreground samples with $z \gtrsim 2$. This justifies our assumption of constant system temperature for both SKA1-MID and HIRAX. For both experiments, we use equally spaced redshift bins of width $\Delta z = 0.5$, with the exception of band 2 with $\Delta z = 0.47$. A more realistic treatment would have to take into account the frequency dependence of the noise temperatures of both experiments, and the different dish and receiver types of SKA1. However, we expect this to have a negligible effect on our results.

Following Battye et al. (2013) and Bull et al. (2015b) for the intensity mapping noise calculations, we calculate the single dish noise for SKA1-MID as

$$N_\ell^{\rm SD} = \sigma_{\rm pix}^2 \Omega_{\rm pix} W_\ell^{-1} \,. \tag{7.19}$$

Here, we use the solid angle per pixel $\Omega_{\rm pix} = 4\pi f_{\rm sky}/N_{\rm pix}$, the number of pixels $N_{\rm pix}$, the beam ($\Theta_{\rm FWHM}$) smoothing function $W_\ell = \exp\left(-\ell^2 \Theta_{\rm FWHM}^2/(8\ln 2)\right)$, the pixel noise $\sigma_{\rm pix} = T_{\rm sys}\sqrt{N_{\rm pix}/(t_{\rm tot}\delta_\nu N_{\rm dish})}$ and the frequency resolution (channel width) δ_ν.

For HIRAX, we calculate the interferometer noise

$$N_\ell^{\rm INT} = \frac{(\lambda^2 T_{\rm sys})^2}{2A_{\rm e}^2 d\nu n(u) t_{\rm p}} \,, \tag{7.20}$$

with the frequency bin width $d\nu$, the time per pointing $t_{\rm p} = t_{\rm tot}/N_{\rm p}$, the effective collecting area of one dish $A_{\rm e} = (D_{\rm dish}/2)^2\pi$, and using the relation $u = \ell/(2\pi)$ for the baseline density $n(u)$.

For all experiments we assume full survey overlap with LSST.

7.3.2 Photometric galaxy counts

We normalize the LSST sample to be a total of $\sim 6.3\times10^9$ galaxies at $m^* = 27$[1]. The galaxy shot noise for LSST is calculated as $C^{\rm shot} = 4\pi/N_{\rm g}^{\rm LSST}(z)$, where we use a fitting function to calculate the number of detected galaxies in the considered redshift bin, $N_{\rm g}^{\rm LSST}$ (Eqs. (7.8) and (7.11)). We consider all possible LSST redshift bins to have their upper edge at the same $z_{\rm max}^{\rm LSST} = 3.9$, and the lower bin edge at a separation from the upper edge of the foreground bin, $z_i^{\rm fg} + 0.1$. The choice of a separation of $\Delta z = 0.1$ is conservative, ruling out any cross-correlations from possible overlaps, caused for example by the uncertainty in the photometric redshift measurements of LSST. We calculate the number count slope for LSST using an adjusted version of the code provided in Alonso et al. (2015b) to extend to more stringent luminosity cutoffs m^*. We then interpolate $(5s_{\rm g} - 2)n_{\rm g}$ on a fine grid (z and m^*) to speed up the numerical calculations.

In order to illustrate the different error contributions and consolidate our findings, Fig. 7.5 shows all summands contributing to the HI-magnification cross correlation error:

$$(\Delta C_\ell^{\rm HI-\mu})^2 = \frac{2}{(2\ell+1)\Delta\ell f_{\rm sky}}\Big((C_\ell^{\rm HI-\mu})^2 + C_\ell^{\rm g-g} C_\ell^{\rm HI-HI} + C^{\rm shot} C_\ell^{\rm HI-HI} + N_\ell C_\ell^{\rm g-g} + C^{\rm shot} N_\ell \Big). \tag{7.21}$$

The amplitude of the different contributions here depends on the choice of experiments and redshift binning.

To ease comparison we used the same single redshift bin for HIRAX and SKA1-MID in Fig. 7.5, from $z = 0.85$ to 1.35. For HIRAX a magnitude cutoff of $m^* = 24.4$ maximizes the signal-to-noise ratio; for SKA1-MID it is 24.3. This optimization will be discussed further in section 7.4. In this case shot noise dominates the error throughout, but it becomes comparable to cosmic variance (mostly $C_\ell^{\rm g-g} C_\ell^{\rm HI-HI}$) on large scales for SKA1-MID. Note that

[1] This is slightly more conservative than the number quoted in LSST Science Collaboration et al. (2009), i.e. almost 10^{10} galaxies for $m^* = 27.5$.

	SKA1 B1	-	-	-
z range	0.34-0.84	0.84-1.34	1.34-1.84	1.84-2.34
m^*	23.6	23.1	26.3	27.0
$\mathrm{SN}_{\mathrm{tot}}$	8.7	6.3	1.1	0.4
	HIRAX	-	-	SKA1 B2
z range	0.78-1.28	1.28-1.78	1.78-2.28	0.0-0.47
m^*	23.0	26.1	27.0	22.1
$\mathrm{SN}_{\mathrm{tot}}$	28.5	9.4	3.8	5.8

TABLE 7.1: Optimized magnitude cutoffs, m^*, as well as cumulative signal to noise values for all experiments and redshift bins. Individual redshift bins of HIRAX are better than SKA1-MID also due to the higher number of ℓ bins that contribute.

small scales are practically inaccessible for SKA1-MID due to its poor angular resolution, restricting it to much larger scales than HIRAX.

The multipole resolution is set by the maximum scale accessible by the SKA, i.e. the survey area S_{area} when in single dish mode. We estimate $\ell_{\mathrm{min}}^{\mathrm{SKA}} = 2\pi/\sqrt{S_{\mathrm{area}}} \sim 3$, but choose a more conservative value of $\ell_{\mathrm{min}}^{\mathrm{SKA}} = 10$ for the Limber approximation to hold (Loverde & Afshordi, 2008). For the HIRAX interferometer it is set by the field of view (fov) which depends on frequency. For the sake of simplicity we ignore this dependence and assume a mean fov $=$ 35.5 deg^2 (Newburgh et al., 2016b), giving $\ell_{\mathrm{min}}^{\mathrm{HIRAX}} = 2\pi/\sqrt{\mathrm{fov}} \sim 60$. From the signal to noise ratio $C_\ell^{\mathrm{HI}-\mu}/\Delta C_\ell^{\mathrm{HI}-\mu}$ we calculate the cumulative (total) signal to noise as

$$\mathrm{SN}_{\mathrm{tot}} = \sqrt{\sum_{\bar{\ell}=\ell_{\mathrm{min}}}^{\ell} (C_{\bar{\ell}}^{\mathrm{HI}-\mu}/\Delta C_{\bar{\ell}}^{\mathrm{HI}-\mu})^2}, \tag{7.22}$$

where the sum runs over the relevant ℓ values, with the minimum ℓ, and the binning $\Delta\ell$, set by ℓ_{min}. We note, however, that the cumulative signal to noise ratio $\mathrm{SN}_{\mathrm{tot}}$ is binning independent.

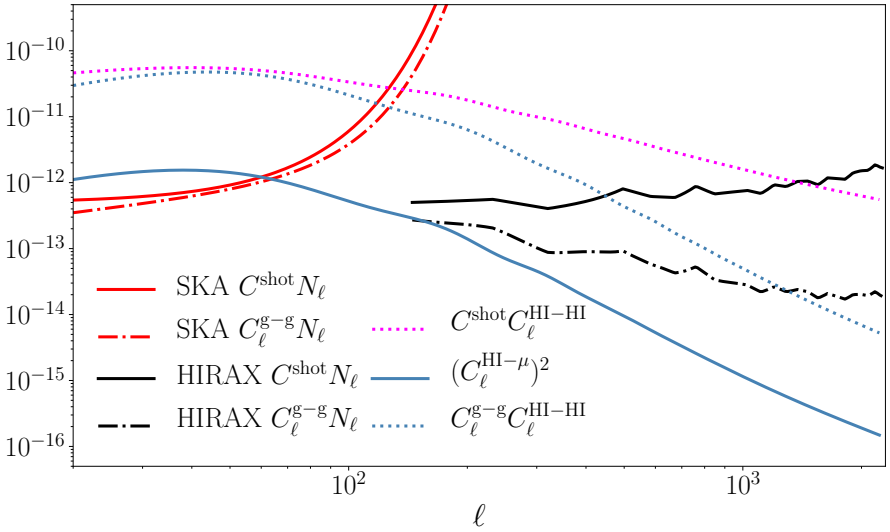

FIGURE 7.5: All contributions to $\Delta C_\ell^{\rm HI-\mu}$ as in Equation (7.21), for a foreground redshift bin from $z = 0.85$ to 1.35 and a background bin $z \geq 1.45$. The common factor of $2/((2\ell+1)\Delta\ell f_{\rm sky}$ was omitted here. Terms proportional to the SKA1-MID (HIRAX) noise are plotted in red (black) and terms proportional to shot noise and cosmic variance are plotted cyan and steel blue respectively. For this choice of binning, the HI intensity mapping noise is subdominant, followed by pure cosmic variance, but both dominated by terms with shot noise, the biggest source of error. Note that the choice of intermediate foreground and background redshift in this plot is only to ease comparison, but not necessarily ideal for magnification measurements.

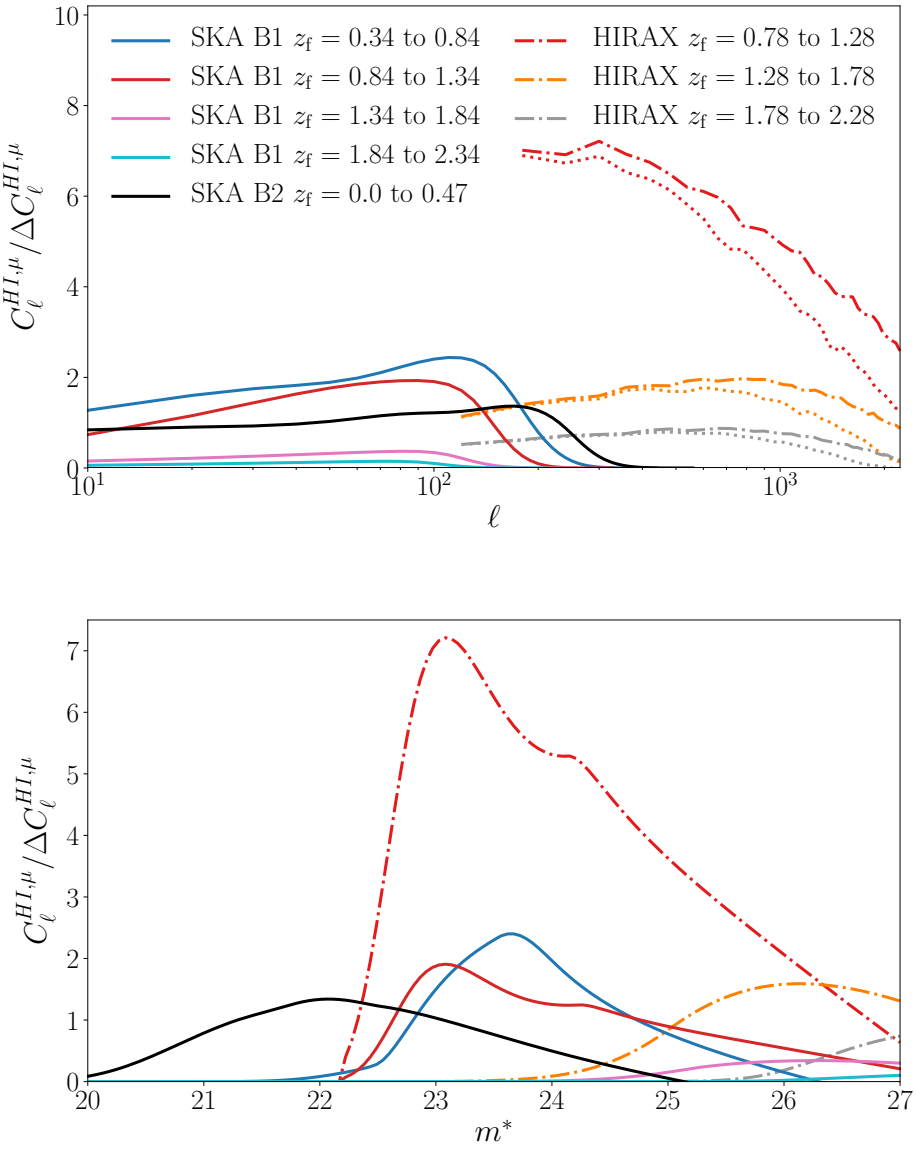

FIGURE 7.6: *Upper panel:* The expected signal to noise ratio of the magnification signal for the combinations HIRAX 1024 (dotted-dashed lines), HIRAX 512 (dotted lines) and SKA1 (solid lines) with LSST. We use different foreground redshift bins, always combined with one single non-overlapping background bin. Shot noise largely dominates, therefore the 512 dish version of HIRAX performs surprisingly well compared to the full array with 1024 dishes. *Lower panel:* The optimization of the signal to noise ratio as a function of magnitude cutoff m^*. This panel is for single ℓ bins only, for SKA1-MID $\ell = 80$ and for HIRAX $\ell = 200$. These values were chosen to lie within the experiment's range of maximum sensitivity.

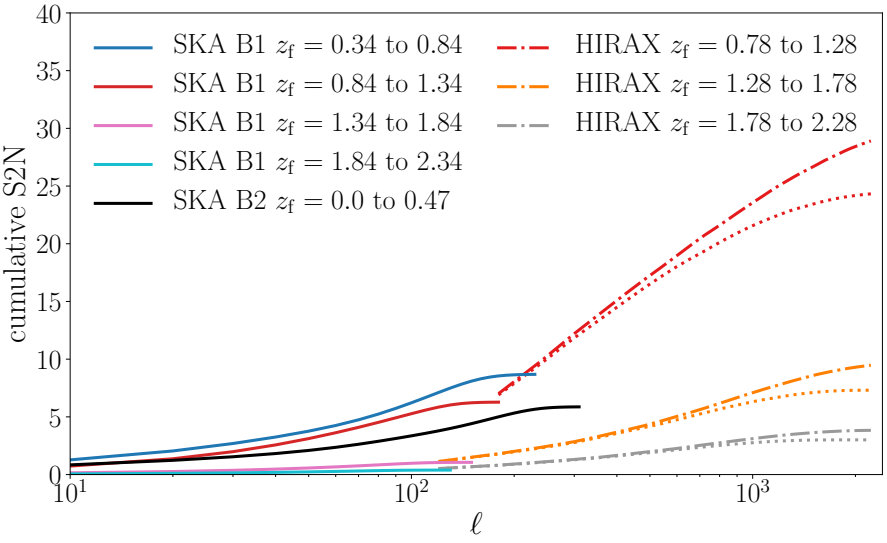

FIGURE 7.7: This plot shows the cumulative signal to noise ratio, Equation (7.22). For HIRAX especially, the error is dominated by the galaxy shot noise. Therefore even the down-scaled design with 512 dishes yields very similar results compared to the full proposal with 1024 dishes.

7.4 Results and Discussion

We maximize the signal to noise ratio with respect to the galaxy magnitude threshold m^* for each HI survey and redshift bin. We consider an optimization range of $m^* \in [19, 27]$ and plot $\mathrm{SN}(m^*)_{\mathrm{tot}}$ for a few examples in Fig. 7.6. The optimal values we found (using the *python* package *scipy optimize*) are shown in Table 7.1. Generally, for low-redshift foreground bins, also a low m^* is preferred, which increases the number count slope at the acceptable cost of increasing the (negligible) shot-noise at these redshifts. For high-redshift foreground bins, however, shot-noise increases and m^* needs to be higher to account for this.

Fig. 7.6 shows the optimized signal to noise as a function of multipole for all considered experiment and redshift combinations. Maps in each foreground redshift bin are correlated with one single redshift bin of LSST, separated from the foreground by $\Delta z = 0.1$ and ranging up to $z = 3.9$. Low redshift foreground bins benefit from a wider background sample containing a larger number of galaxies. Therefore, they often perform better than high redshift bins, especially in the case for HIRAX. The sensitivity of HIRAX is best at comparably small scales, where the power spectrum drops $\sim \ell^2$ (see e.g. Fig. 7.3). The shot noise, however, becomes the dominant error on smaller scales. The 512 dish design for HIRAX performs surprisingly well, as even in this case the interferometer noise remains subdominant.

Figure 7.7 shows the cumulative signal to noise which reaches levels of ~ 30 for individual redshift bins. The performance of SKA1-MID and HIRAX is similar for single ℓ bins, but HIRAX covers a larger multipole range. Both experiments yield best results at intermediate redshifts of $0.6 < z < 1.3$. As they are sensitive to different angular scales, most of their constraining power can be combined.

7.5 Conclusions

In this chapter we proposed the use of HI intensity maps from large sky surveys with forthcoming radio arrays in cross-correlation with background optical

galaxy samples from Stage IV photometric surveys, in order to detect the cosmic magnification signal.

We then derived predictions for the signal-to-noise ratio of the magnification signal from the foreground HI maps acting on background galaxies. We considered the survey combinations HIRAX with LSST and SKA1-MID with LSST. The signal-to-noise was optimized by changing the galaxy magnitude threshold m^* for LSST, since a lower magnitude cutoff boosts the magnification signal. Due to their different resolutions and mode operations, the information provided by the HIRAX interferometer is complimentary to the data gathered by SKA1-MID in autocorrelation (single dish) mode. A detection seems likely with forecasted cumulative signal to noise ratios in the range of $\sim$ 30, but a more detailed analysis with appropriate simulations will be needed to fully assess all relevant sources of errors, e.g. foreground contamination residuals and cleaning effects. Foreground residuals are not expected to be significant in the cross-correlation between HI intensity maps and galaxies. The loss of long-wavelength radial modes in the HI data is also not expected to have a significant deteriorating effect on this observable. However, it would be useful to properly account and quantify both of these effects by extending the cross-correlation simulations studies performed in Witzemann et al. (2019b); Cunnington et al. (2019a,b) – we leave this for future work. We also note that the choice of redshift binning could be reconsidered to make the analysis more realistic for a foreground cleaned HI survey. Furthermore, using realistic simulated LSST catalogs we can implement and test the performance of scale-dependent optimal weighting functions (Yang & Zhang, 2011).

To conclude, our derived forecasts for the signal-to-noise for this detection suggest that it will certainly be possible once the data is available, and that it will be complementary to measurements using optical foreground samples with completely different systematics.

8 Conclusions

The bulk of the work conducted for this thesis was done in the context of three individual research projects, presented in chapters 5 to 7. Using mock data of planned instruments, each project provides forecasts for a specific analysis method. Mapping the intensity of 21cm radiation of neutral hydrogen in the universe is arguably the most promising and groundbreaking new window to cosmology, accessible with next generation radio telescopes. We first introduced to general cosmology, forecasting, and to radio cosmology and its observational probes. To give a more specific introduction to the content of the main body of this thesis, we then continued with a focus on 21cm intensity mapping and the necessary removal of foregrounds.

In chapter 5, we demonstrated that BAO measurements by an instrument like HIRAX constrain the Hubble rate and the angular diameter distance as functions of redshift. Especially when combined with the BAO measurement of the distance to the CMB, this allows to put tight constraints on curvature, even in a scenario with an entirely general non-parametric model of dark energy. To do this, we used Bayesian statistics for a computationally intense MCMC analysis with many parameters. We also present forecasts for two types of perfect telescopes using HIRAX' baseline distribution and dish diameter, and show that even in that case the curvature constraints might be insufficient for ruling out certain theories of inflation. In order to further improve the constraints, it is necessary to assume an informative set of priors or make assumptions on the equation of state of dark energy, motivated by a physical understanding.

Chapter 6 presents an in-depth study of the so called multi-tracer technique in a realistically simulated scenario including foregrounds of the 21cm intensity maps. We simulated 200 HI and 200 galaxy maps, each pair tracing the same underlying dark matter distribution. For each HI map, we then simulated four different sources of foreground radiation, noise, and convolved the maps with

a Gaussian beam pattern. We constructed different estimators of the ratio of the HI and galaxy bias, $b_{\rm HI}/b_{\rm g}$, using the galaxy-galaxy auto-correlation $C_\ell^{\rm gg}$, the HI-HI auto-correlation $C_\ell^{\rm HH}$ and the galaxy-HI cross-correlation $C_\ell^{\rm gH}$. We found that estimators using HI auto-correlations suffer from systematic errors, both due to foreground residuals and the loss of small-scale angular modes from the uncertainty in photometric redshifts. Other estimators are vastly free from systematic errors, but in all cases, the foreground removal introduces the dominant statistical error on the ratio of biases. We confirm that this is caused by the loss of long radial modes associated with foreground cleaning, combined with the lack of small radial modes from the photometric redshift determination. Therefore the combination of photometric galaxy maps with foreground cleaned intensity maps sees a small overlap of radial modes, making cancellation of cosmic variance difficult, albeit possible. Our results improve on the cosmic variance limit by a factor of ~ 2.5. To conclude, we discuss other possible survey combinations which could yield better results, and the potential of future work to derive constraints on the non-Gaussianity parameters from the bias ratio.

In chapter 7, we also combined HI intensity with galaxy maps, but for an entirely different purpose. We assumed a foreground of HI maps acting as a magnifying lens on the clustering of background galaxies. Non-zero cross-correlations between maps well separated in redshift can be used to detect the so-called cosmic magnification signal. We demonstrate that this faint signal can possibly be detected using a combination of HI maps from SKA1 and HIRAX and galaxy maps from LSST.

This work also raises new questions. In chapter 6 we saw that the combination of intensity maps and photometric galaxy surveys is not ideal due to the small overlap of modes in Fourier space. Other combinations, like HI IM - spectroscopic galaxy or intensity mapping of different emission lines, will not suffer from these restrictions. Their comparably small survey volume or foreground residual cross-correlations will degrade their constraining power, but a detailed study could quantify their potential. Chapter 7 presents a rough estimate of the signal to noise ratio of a detection of the magnification signal between HI intensity maps and background galaxies. A

future work could use more realistic modeling and take into account more error sources, foreground contamination in particular. Parameter constraint forecasts from the magnification signal would also be interesting.

We have examined in-depth three examples of novel opportunities using 21cm intensity and galaxy clustering maps, obtained from next generation radio and optical surveys. In all three cases, our results are promising, which is mainly thanks to the incredible performance expected of the next generation instruments. Detections of new effects seem very likely, extensions of standard cosmology can efficiently be tested and even fundamental limits in cosmology can potentially be breached. The first large-volume data-sets will become available soon, revolutionizing precision in cosmology, maybe even calling for a new standard model.

Bibliography

Abate A., et al., 2012

Abbott T., et al., 2016, Mon. Not. Roy. Astron. Soc., 460, 1270

Abbott T. M. C., et al., 2018, Phys. Rev. D, 98, 043526

Abramo L. R., Bertacca D., 2017, Phys. Rev., D96, 123535

Abramo L. R., Leonard K. E., 2013, Mon. Not. Roy. Astron. Soc., 432, 318

Alam S., et al., 2017, MNRAS, 470, 2617

Albrecht A., et al., 2006, ArXiv Astrophysics e-prints,

Albrecht A., et al., 2009, arXiv e-prints,

Alonso D., Ferreira P. G., 2015, Phys. Rev. D, 92, 063525

Alonso D., Ferreira P. G., Santos M. G., 2014, Monthly Notices of the Royal Astronomical Society, 444, 3183

Alonso D., Bull P., Ferreira P. G., Santos M. G., 2015a, Monthly Notices of the Royal Astronomical Society, 447, 400

Alonso D., Bull P., Ferreira P. G., Maartens R., Santos M. G., 2015b, The Astrophysical Journal, 814, 145

Alonso D., Ferreira P. G., Jarvis M. J., Moodley K., 2017, Phys. Rev. D, 96, 043515

Amendola L., et al., 2018, Living Rev. Rel., 21, 2

Anderson C. J., et al., 2018, MNRAS, 476, 3382

Arun K., Gudennavar S. B., Sivaram C., 2017, Advances in Space Research, 60, 166

Aslanyan G., Easther R., 2015, Phys. Rev. D, 91, 123523

Audren B., Lesgourgues J., Benabed K., Prunet S., 2013, Journal of Cosmology and Astro-Particle Physics, 2013, 001

Bacon D. J., Refregier A. R., Ellis R. S., 2000, Mon. Not. Roy. Astron. Soc., 318, 625

Bacon D. J., Andrianomena S., Clarkson C., Bolejko K., Maartens R., 2014, Monthly Notices of the Royal Astronomical Society, 443, 1900

Bandura K., et al., 2014, in Ground-based and Airborne Telescopes V. p. 914522 (`arXiv:1406.2288`), doi:10.1117/12.2054950

Bartelmann M., Schneider P., 2001, Phys. Rep., 340, 291

Battye R. A., Davies R. D., Weller J., 2004, MNRAS, 355, 1339

Battye R. A., Browne I. W. A., Dickinson C., Heron G., Maffei B., Pourtsidou A., 2013, MNRAS, 434, 1239

Bengaly C. A. P., Siewert T. M., Schwarz D. J., Maartens R., 2018, preprint, (`arXiv:1810.04960`)

Bennett C. L., et al., 2003, ApJS, 148, 1

Bernstein G., Jain B., 2004, ApJ, 600, 17

Blake C., Glazebrook K., 2003, ApJ, 594, 665

Blake C., Wall J., 2002, Nature, 416, 150

Blake C., et al., 2013, MNRAS, 436, 3089

Bonvin C., 2008, Phys. Rev. D, 78, 123530

Bonvin C., 2014, Classical and Quantum Gravity, 31, 234002

Bonvin C., Durrer R., 2011, Phys. Rev. D, 84, 063505

Bonvin C., Durrer R., Gasparini M. A., 2006, Phys. Rev. D, 73, 023523

Bonvin C., Andrianomena S., Bacon D., Clarkson C., Maartens R., Moloi T., Bull P., 2017, MNRAS, 472, 3936

Bowman J. D., Morales M. F., Hewitt J. N., 2009, ApJ, 695, 183

Brooks S. P., Gelman A., 1998, Journal of Computational and Graphical Statistics, 7, 434

Bruni M., Crittenden R., Koyama K., Maartens R., Pitrou C., Wands D., 2012, Phys. Rev. D, 85, 041301

Bucher M., Goldhaber A. S., Turok N., 1995, Phys. Rev. D, 52, 3314

Bull P., Camera S., Raccanelli A., Blake C., Ferreira P., Santos M., Schwarz D. J., 2015a, Advancing Astrophysics with the Square Kilometre Array (AASKA14), p. 24

Bull P., Ferreira P. G., Patel P., Santos M. G., 2015b, The Astrophysical Journal, 803, 21

Burles S., Tytler D., 1998, ApJ, 499, 699

Camera S., Santos M. G., Bacon D. J., Jarvis M. J., McAlpine K., Norris R. P., Raccanelli A., Röttgering H., 2012, MNRAS, 427, 2079

Camera S., Santos M. G., Ferreira P. G., Ferramacho L., 2013, Phys. Rev. Lett., 111, 171302

Camera S., Santos M. G., Maartens R., 2015, Mon. Not. Roy. Astron. Soc., 448, 1035

Carucci I. P., Villaescusa-Navarro F., Viel M., Lapi A., 2015, Journal of Cosmology and Astroparticle Physics, 2015, 047

Challinor A., Lewis A., 2011, Phys. Rev. D, 84, 043516

Chang T.-C., Pen U.-L., Peterson J. B., McDonald P., 2008, Phys. Rev. Lett., 100, 091303

Chapman E., et al., 2013, MNRAS, 429, 165

Chevallier M., Polarski D., 2001, International Journal of Modern Physics D, 10, 213

Clarkson C., Cortês M., Bassett B., 2007, JCAP, 8, 011

Coe D., 2009, arXiv e-prints, p. arXiv:0906.4123

Cole S., et al., 2005, MNRAS, 362, 505

Coles P., Jones B., 1991, MNRAS, 248, 1

Colin J., Mohayaee R., Rameez M., Sarkar S., 2017, Monthly Notices of the Royal Astronomical Society, 471, 1045

Conley A., et al., 2006, ApJ, 644, 1

Cooray A., Sheth R., 2002, Phys. Rep., 372, 1

Copi C. J., Schramm D. N., Turner M. S., 1995, Science, 267, 192

Cornish N. J., Spergel D. N., Starkman G. D., 1996, Physical Review Letters, 77, 215

Cowles M. K., Carlin B. P., 1996, Journal of the American Statistical Association, 91, 883

Croft R. A. C., Weinberg D. H., Bolte M., Burles S., Hernquist L., Katz N., Kirkman D., Tytler D., 2002, ApJ, 581, 20

Cunnington S., Harrison I., Pourtsidou A., Bacon D., 2018, MNRAS,

Cunnington S., Wolz L., Pourtsidou A., Bacon D., 2019a

Cunnington S., Harrison I., Pourtsidou A., Bacon D., 2019b, Mon. Not. Roy. Astron. Soc., 482, 3341

Dalal N., Doré O., Huterer D., Shirokov A., 2008, Phys. Rev. D, 77, 123514

Dark Energy Survey Collaboration et al., 2016, MNRAS, 460, 1270

DeBoer D. R., et al., 2017, PASP, 129, 045001

Di Dio E., Montanari F., Lesgourgues J., Durrer R., 2014, Classical and Quantum Gravity, 31, 234002

Di Matteo T., Perna R., Abel T., Rees M. J., 2002, ApJ, 564, 576

Dodelson S., 2003, Modern cosmology. Academic Press, San Diego, CA, https://cds.cern.ch/record/1282338

Duncan C., Joachimi B., Heavens A., Heymans C., Hildebrandt H., 2014, Mon. Not. Roy. Astron. Soc., 437, 2471

Dunkley J., Bucher M., Ferreira P. G., Moodley K., Skordis C., 2005, MNRAS, 356, 925

Eisenstein D. J., Hu W., 1998, ApJ, 496, 605

Eisenstein D. J., Hu W., Tegmark M., 1998, ApJ, 504, L57

Eisenstein D. J., et al., 2005, ApJ, 633, 560

Eisenstein D. J., Seo H.-J., Sirko E., Spergel D. N., 2007, ApJ, 664, 675

Ekers R., 2012, arXiv e-prints, p. arXiv:1212.3497

Fan X., Bahcall N. A., Cen R., 1997, The Astrophysical Journal Letters, 490, L123

Fan X., Carilli C. L., Keating B., 2006, ARA&A, 44, 415

Ferramacho L. D., Santos M. G., Jarvis M. J., Camera S., 2014, MNRAS, 442, 2511

Fonseca J., Camera S., Santos M. G., Maartens R., 2015, ApJ, 812, L22

Fonseca J., Maartens R., Santos M. G., 2017, Mon. Not. Roy. Astron. Soc., 466, 2780

Fonseca J., Maartens R., Santos M. G., 2018, Mon. Not. Roy. Astron. Soc., 479, 3490

Foreman-Mackey D., Hogg D. W., Lang D., Goodman J., 2013, Publications of the Astronomical Society of the Pacific, 125, 306

Frigo M., Johnson S. G., 2005, Proceedings of the IEEE, 93, 216

Furlanetto S. R., Oh S. P., Briggs F. H., 2006, Phys. Rep., 433, 181

G. Labate M., Braun R., Dewdney P., Waterson M., Wagg J., 2017. pp 1–4, doi:10.23919/URSIGASS.2017.8105424

Gabasch A., et al., 2006, A&A, 448, 101

Garcia-Fernandez M., et al., 2018, Mon. Not. Roy. Astron. Soc., 476, 1071

Garrett M. A., Cordes J. M., Deboer D. R., Jonas J. L., Rawlings S., Schilizzi R. T., 2010, arXiv e-prints, p. arXiv:1008.2871

Gelman A., Rubin D. B., 1992, Statist. Sci., 7, 457

Giannantonio T., Porciani C., Carron J., Amara A., Pillepich A., 2012, Mon. Not. Roy. Astron. Soc., 422, 2854

Gleser L., Nusser A., Benson A. J., 2008, MNRAS, 391, 383

Goodman J., Weare J., 2010, Communications in Applied Mathematics and Computational Science, Vol.˜5, No.˜1, p.˜65-80, 2010, 5, 65

Gunn J. E., et al., 2006, AJ, 131, 2332

Guth A. H., Nomura Y., 2012, Phys. Rev. D, 86, 023534

Guth A. H., Kaiser D. I., Nomura Y., 2014, Physics Letters B, 733, 112

Hall A., Bonvin C., Challinor A., 2013, Phys. Rev. D, 87, 064026

Hamaus N., Seljak U., Desjacques V., 2011, Phys. Rev., D84, 083509

Harker G., et al., 2009, MNRAS, 397, 1138

Harker G., et al., 2010, MNRAS, 405, 2492

Harper S. E., Dickinson C., Battye R. A., Roychowdhury S., Browne I. W. A., Ma Y.-Z., Olivari L. C., Chen T., 2018, MNRAS, 478, 2416

Haslam C. G. T., Salter C. J., Stoffel H., Wilson W. E., 1982, A&AS, 47, 1

Hastings W. K., 1970, Biometrika, 57, 97

Haverkorn M., Brown J. C., Gaensler B. M., McClure-Griffiths N. M., 2008, The Astrophysical Journal, 680, 362

Heymans C., et al., 2012, Mon. Not. Roy. Astron. Soc., 427, 146

Hildebrandt H., van Waerbeke L., Erben T., 2009, A&A, 507, 683

Hlozek R., Cortês M., Clarkson C., Bassett B., 2008, General Relativity and Gravitation, 40, 285

Hu W., Dodelson S., 2002, Annual Review of Astronomy and Astrophysics, 40, 171

Hu W., Eisenstein D. J., Tegmark M., White M., 1999, Phys. Rev. D, 59, 023512

Hui L., Gaztañaga E., Loverde M., 2007, Phys. Rev. D, 76, 103502

Huterer D., Peiris H. V., 2007, Phys. Rev., D75, 083503

Huynh M., Lazio J., 2013, arXiv e-prints, p. arXiv:1311.4288

Ivarsen M. F., Bull P., Llinares C., Mota D., 2016, A&A, 595, A40

Jackson J. D., 1999, Classical electrodynamics, 3rd ed. edn. Wiley, New York, NY, `http://cdsweb.cern.ch/record/490457`

Jain B., Taylor A., 2003, Phys. Rev. Lett., 91, 141302

Jeffreys H., 1946, Proceedings of the Royal Society of London. Series A. Mathematical and Physical Sciences, 186, 453

Jelić V., Zaroubi S., Labropoulos P., Bernardi G., de Bruyn A. G., Koopmans L. V. E., 2010, MNRAS, 409, 1647

Jeong D., Schmidt F., Hirata C. M., 2012, Phys. Rev. D, 85, 023504

Jonas J., MeerKAT Team 2016, in Proceedings of MeerKAT Science: On the Pathway to the SKA. 25-27 May, 2016 Stellenbosch, South Africa (MeerKAT2016).

Kaiser N., 1987, MNRAS, 227, 1

Kaiser N., Wilson G., Luppino G. A., 2000

Kass R. E., Carlin B. P., Gelman A., Neal R. M., 1998, The American Statistician, 52, 93

Kazin E. A., et al., 2014, MNRAS, 441, 3524

Kendall M. G., Stuart A., Ord J. K., eds, 1987, Kendall's Advanced Theory of Statistics. Oxford University Press, Inc., New York, NY, USA

Kilbinger M., 2015, Rept. Prog. Phys., 78, 086901

Kleban M., Schillo M., 2012, JCAP, 2012, 029

Knox L., 1995, Phys. Rev. D, 52, 4307

Knox L., 2006, Phys. Rev. D, 73, 023503

Koda J., et al., 2014, MNRAS, 445, 4267

Kovetz E. D., et al., 2017, arXiv e-prints, p. arXiv:1709.09066

Kunz M., Nesseris S., Sawicki I., 2016, Phys. Rev. D, 94, 023510

LSST Science Collaboration et al., 2009, arXiv e-prints, p. arXiv:0912.0201

Laureijs R., et al., 2011, arXiv e-prints, p. arXiv:1110.3193

Leonard C. D., Bull P., Allison R., 2016, Phys. Rev., D94, 023502

Lewis A., Bridle S., 2002, Phys. Rev. D, 66, 103511

Lewis A., Challinor A., 2007, Phys. Rev. D, 76, 083005

Lewis A., Challinor A., Lasenby A., 2000, ApJ, 538, 473

Limber D. N., 1954, ApJ, 119, 655

Linder E. V., 2003, Phys. Rev. Lett., 90, 091301

Liu A., Tegmark M., 2011, Phys. Rev. D, 83, 103006

Liu A., Tegmark M., Zaldarriaga M., 2009a, MNRAS, 394, 1575

Liu A., Tegmark M., Bowman J., Hewitt J., Zaldarriaga M., 2009b, MNRAS, 398, 401

Lonsdale C. J., et al., 2009, IEEE Proceedings, 97, 1497

Loverde M., Afshordi N., 2008, Phys. Rev. D, 78, 123506

Mandelbaum R., 2018, Ann. Rev. Astron. Astrophys., 56, 393

Marín F. A., Beutler F., Blake C., Koda J., Kazin E., Schneider D. P., 2016, MNRAS, 455, 4046

Marsh D. J. E., Bull P., Ferreira P. G., Pontzen A., 2014, Phys. Rev., D90, 105023

Masui K. W., et al., 2013, ApJ, 763, L20

Matarrese S., Verde L., 2008, Astrophys. J., 677, L77

McDonald P., Seljak U., 2009, JCAP, 0910, 007

McQuinn M., Zahn O., Zaldarriaga M., Hernquist L., Furlanetto S. R., 2006, ApJ, 653, 815

Menard B., Bartelmann M., 2002, Astron. Astrophys., 386, 784

Menard B., Scranton R., Fukugita M., Richards G., 2010, Mon. Not. Roy. Astron. Soc., 405, 1025

Metropolis N., Rosenbluth A. W., Rosenbluth M. N., Teller A. H., Teller E., 1953, The Journal of Chemical Physics, 21, 1087

Misner C. W., Thorne K. S., Wheeler J. A., 1973, Gravitation

Moore D. F., Aguirre J. E., Parsons A. R., Jacobs D. C., Pober J. C., 2013, ApJ, 769, 154

Morales M. F., Wyithe J. S. B., 2010, ARA&A, 48, 127

Nesseris S., Sapone D., 2014, Phys. Rev. D, 90, 063006

Newburgh L., et al., 2016a, Proc. SPIE Int. Soc. Opt. Eng., 9906, 99065X

Newburgh L. B., et al., 2016b, in Ground-based and Airborne Telescopes VI. p. 99065X (`arXiv:1607.02059`), doi:10.1117/12.2234286

Oh S. P., 1999, ApJ, 527, 16

Oh S. P., Mack K. J., 2003, MNRAS, 346, 871

Pacholczyk A. G., 1970, Radio astrophysics. Nonthermal processes in galactic and extragalactic sources

Padmanabhan H., 2018, MNRAS, 475, 1477

Padmanabhan N., White M., 2009, Phys. Rev. D, 80, 063508

Padmanabhan H., Choudhury T. R., Refregier A., 2015, MNRAS, 447, 3745

Patel P., Bacon D. J., Beswick R. J., Muxlow T. W. B., Hoyle B., 2010, MNRAS, 401, 2572

Percival W. J., Samushia L., Ross A. J., Shapiro C., Raccanelli A., 2011, Philosophical Transactions of the Royal Society of London Series A, 369, 5058

Perlmutter S., et al., 1999, ApJ, 517, 565

Peter P., Uzan J.-P., 2009, Primordial cosmology. Oxford Graduate Texts, Oxford Univ. Press, Oxford, `https://cds.cern.ch/record/1208401`

Peterson J. B., Pen U., Wu X., 2005, in Kassim N., Perez M., Junor W., Henning P., eds, Astronomical Society of the Pacific Conference Series Vol. 345, From Clark Lake to the Long Wavelength Array: Bill Erickson's Radio Science. p. 441 (arXiv:astro-ph/0502029)

Planck Collaboration XIII 2016, A&A, 594, A13

Planck Collaboration et al., 2016, A&A, 594, A17

Pourtsidou A., Bacon D., Crittenden R., Metcalf R. B., 2016, Monthly Notices of the Royal Astronomical Society, 459, 863

Pourtsidou A., Bacon D., Crittenden R., 2017, Monthly Notices of the Royal Astronomical Society, 470, 4251

Pritchard J. R., Loeb A., 2012, Reports on Progress in Physics, 75, 086901

Pullen A. R., Serra P., Chang T.-C., Doré O., Ho S., 2018, MNRAS, 478, 1911

Raccanelli A., Montanari F., Bertacca D., DorÃ© O., Durrer R., 2016, JCAP, 1605, 009

Raveri M., Bull P., Silvestri A., Pogosian L., 2017, arXiv:1703.05297

Riess A. G., et al., 1998, AJ, 116, 1009

Ross A. J., et al., 2011, MNRAS, 417, 1350

Ross A. J., et al., 2014, MNRAS, 437, 1109

Rubin V. C., Ford Jr. W. K., 1970, ApJ, 159, 379

Rybicki G. B., Lightman A. P., 1979, Radiative processes in astrophysics

Sánchez A. G., et al., 2017, MNRAS, 464, 1493

Santos M. G., Cooray A., Knox L., 2005, ApJ, 625, 575

Santos M., et al., 2015, Advancing Astrophysics with the Square Kilometre Array (AASKA14), p. 19

Santos M., et al., 2016, in Proceedings of MeerKAT Science: On the Pathway to the SKA. 25-27 May. p. 32

Santos M. G., et al., 2017, preprint, (arXiv:1709.06099)

Schechter P., 1976, ApJ, 203, 297

Schinckel A. E., Bunton J. D., Cornwell T. J., Feain I., Hay S. G., 2012, in Ground-based and Airborne Telescopes IV. p. 84442A, doi:10.1117/12.926959

Schmittfull M., Seljak U., 2018, Phys. Rev. D, 97, 123540

Schulz A. E., 2010, ApJ, 724, 1305

Scranton R., et al., 2005, ApJ, 633, 589

Seljak U., 2009, Physical Review Letters, 102, 021302

Seljak U., Zaldarriaga M., 1996, ApJ, 469, 437

Shaw J. R., Sigurdson K., Pen U.-L., Stebbins A., Sitwell M., 2014, ApJ, 781, 57

Shaw J. R., Sigurdson K., Sitwell M., Stebbins A., Pen U.-L., 2015, Phys. Rev. D, 91, 083514

Sheth R. K., Tormen G., 1999, MNRAS, 308, 119

Smith M. S., Kawano L. H., Malaney R. A., 1993, ApJS, 85, 219

Smith R. E., et al., 2003, Mon. Not. Roy. Astron. Soc., 341, 1311

Sokal A., 1997, Monte Carlo Methods in Statistical Mechanics: Foundations and New Algorithms. Springer US, Boston, MA, pp 131–192

Spergel D. N., et al., 2007, The Astrophysical Journal Supplement Series, 170, 377

Square Kilometre Array Cosmology Science Working Group et al., 2018, preprint, (arXiv:1811.02743)

Switzer E. R., 2017, ApJ, 838, 82

Switzer E. R., et al., 2013, MNRAS, 434, L46

Takada M., Dore O., 2015, Phys. Rev., D92, 123518

Takahashi R., Sato M., Nishimichi T., Taruya A., Oguri M., 2012, Astrophys. J., 761, 152

Taylor A. N., Kitching T. D., Bacon D. J., Heavens A. F., 2007, MNRAS, 374, 1377

Tegmark M., Eisenstein D. J., Hu W., de Oliveira-Costa A., 2000, The Astrophysical Journal, 530, 133

Testori J. C., Reich P., Reich W., 2008, A&A, 484, 733

Thyagarajan N., et al., 2015, ApJ, 804, 14

Tully R. B., Fisher J. R., 1977, A&A, 54, 661

Tyson J. A., Valdes F., Wenk R. A., 1990, ApJ, 349, L1

Van Waerbeke L., Hildebrandt H., Ford J., Milkeraitis M., 2010, Astrophys. J., 723, L13

Vardanyan M., Trotta R., Silk J., 2009, Mon. Not. Roy. Astron. Soc., 397, 431

Viel M., Markovič K., Baldi M., Weller J., 2012, Monthly Notices of the Royal Astronomical Society, 421, 50

Villaescusa-Navarro F., Bull P., Viel M., 2015, ApJ, 814, 146

Villaescusa-Navarro F., Alonso D., Viel M., 2017, MNRAS, 466, 2736

Villaescusa-Navarro F., et al., 2018, ApJ, 866, 135

Waelkens A., Jaffe T., Reinecke M., Kitaura F. S., Enßlin T. A., 2009, A&A, 495, 697

Wagner C., Müller V., Steinmetz M., 2008, A&A, 487, 63

Walker T. P., Steigman G., Schramm D. N., Olive K. A., Kang H.-S., 1991, ApJ, 376, 51

Walters A., Weltman A., Gaensler B. M., Ma Y.-Z., Witzemann A., 2018, ApJ, 856, 65

Wang X., Tegmark M., Santos M. G., Knox L., 2006, ApJ, 650, 529

Weinberg D. H., Davé R., Katz N., Hernquist L., 2004, The Astrophysical Journal, 601, 1

Widrow L. M., Pym B., Dubinski J., 2008, ApJ, 679, 1239

Wilman R. J., et al., 2008, MNRAS, 388, 1335

Wilson T. L., Rohlfs K., Hüttemeister S., 2013, Tools of Radio Astronomy, doi:10.1007/978-3-642-39950-3.

Wittman D. M., Tyson J. A., Kirkman D., Dell'Antonio I., Bernstein G., 2000, Nature, 405, 143

Witzemann A., Bull P., Clarkson C., Santos M. G., Spinelli M., Weltman A., 2018, MNRAS, 477, L122

Witzemann A., Pourtsidou A., Santos M. G., 2019a, preprint (`arXiv:1907.00755`)

Witzemann A., Alonso D., Fonseca J., Santos M. G., 2019b, MNRAS, 485, 5519

Wolleben M., Landecker T. L., Reich W., Wielebinski R., 2006, A&A, 448, 411

Wolz L., Abdalla F. B., Blake C., Shaw J. R., Chapman E., Rawlings S., 2014, MNRAS, 441, 3271

Wolz L., Blake C., Wyithe J. S. B., 2017, Monthly Notices of the Royal Astronomical Society, 470, 3220

Yahya S., Bull P., Santos M. G., Silva M., Maartens R., Okouma P., Bassett B., 2015, MNRAS, 450, 2251

Yamauchi D., Takahashi K., Oguri M., 2014, Phys. Rev., D90, 083520

Yang X., Zhang P., 2011, Mon. Not. Roy. Astron. Soc., 415, L45

Yoo J., 2010, Phys. Rev. D, 82, 083508

Yoo J., Desjacques V., 2013, Phys. Rev. D, 88, 023502

Yoo J., Seljak U., 2015, Monthly Notices of the Royal Astronomical Society, 447, 1789

Yoo J., Hamaus N., Seljak U. c. v., Zaldarriaga M., 2012, Phys. Rev. D, 86, 063514

Zhang P., Pen U.-L., 2006, MNRAS, 367, 169

Ziour R., Hui L., 2008, Phys. Rev. D, 78, 123517

Zuo S., Chen X., Ansari R., Lu Y., 2018, preprint, (`arXiv:1801.04082`)

Zwicky F., 1937, ApJ, 86, 217

de Oliveira-Costa A., Tegmark M., Gaensler B. M., Jonas J., Landecker T. L., Reich P., 2008, MNRAS, 388, 247

de Putter R., Gleyzes J., Dor O., 2017, Phys. Rev., D95, 123507

van Uitert E., et al., 2018, Mon. Not. Roy. Astron. Soc., 476, 4662

van Waerbeke L., et al., 2000, Astron. Astrophys., 358, 30